QUANTIFYING EFFECTS OF HYDROMETEOR DROPLET CHARACTERISTICS ON WIND TURBINE BLADE LEADING EDGE EROSION

A Thesis

Presented to the Faculty of the Graduate School

of Cornell University

In Partial Fulfillment of the Requirements for the Degree of

Master of Science

by

Shuolin Li

May of 2019

ABSTRACT

Blading leading edge erosion, a significant source of reduction in energy production and increased maintenance costs can occur on any wind turbine in any wind farm. However, the current understanding of how hydrometeor droplet impacts the erosion process is far from conclusive. In this work, a CFD framework based on ANSYS Fluent has been built to analyze the influence of rain droplet characteristics on the blade leading edge erosion. I present aerodynamical simulations of a modeled three-blade wind turbine and use those as the basis for the rain droplet injection analysis. This work shows that the particle trajectories are closely related to the inflow wind conditions and blade rotation. The inlet wind velocity is observed as an important factor in determining how many particles impact the blade (indicated as trapping to the blade wall). Moreover, limited evaluation of rain droplet sizes indicates that their trajectories vary by diameter.

BIOGRAPHICAL SKETCH

Shuolin Li is a graduate student (2018-2019) in the Sibley School of Mechanical and Aerospace Engineering at Cornell University. He works for the degree of Master of Science in Mechanical Engineering (minor in Earth and Atmospheric Sciences) under the supervision of Professor Rebecca Barthelme. His master research is on using computational fluid dynamics approaches to investigate the influence of rain droplets on the wind turbine blade performance. The committee members of his master research include Professor Sara C. Pryor, a professor in Earth and Atmospheric Sciences and Professor Gregory Bewley who is a professor in Mechanical Engineering.

ACKNOWLEDGMENTS

I express my sincere thanks to Croll Faculty Fellow Professor Rebecca Barthelmie, without whom this thesis would not have been possible. Prof. Barthelmie is an expert in wind energy research due to whom I begin interested in the wind-related meteorological and mechanical questions. She is also a very helpful advisor to work with, always there offering suggestions when I am confused about my research. It has always been enjoyable to discuss with her.

On the same time, I thank Professor Sara C. Pryor, an expert in the field of atmospheric science. Through the discussions and the emails with her, I was impressed by her incisive understanding of the problem and the useful suggestions in research. Moreover, it is my honor to have Professor Gregory Bewley as my committee member. This research benefits a lot from his suggestions. Finally, I must thank Dr. Rajesh Bhaskaran who helped me a lot in the ANSYS training and Dr. Fred Letson for answering many meteorological questions.

I would like to thank my mother, father, and sister who are always supportive of my studies and life decisions financially and spiritually. It is my true blessing.

I thank all those who have helped make my Master life colorful here at Cornell. Without these people and experiences, I cannot make it here

At last but not the least, I acknowledge the financial support from Cornell Graduate School Fellowship and the funding from U.S. Department of Energy (DE-SC0016438), Cornell University's Atkinson Center for a Sustainable Future (ACSF-SP2279-2018) and Engaged Cornell (ECG16.007/17.007).

TABLE OF CONTENTS

CHAPTER 1

INTRODUCTION TO BLADE LEADING EDGE EROSION

Wind energy is playing a more and more important role in contributing to electricity generation. Over the past two decades, wind energy has been developing significantly. In 2018, about 519GW of onshore wind energy capacity was installed worldwide along with 23GW of offshore wind energy capacity [GWEC, 2018]. It is expected that over 50GW further capacity will be installed each year until 2023, and at least 6GW each year offshore [EWEA, 2011; Goch et al., 2012; Morata and Sandoval, 2012; Slot et al., 2015].

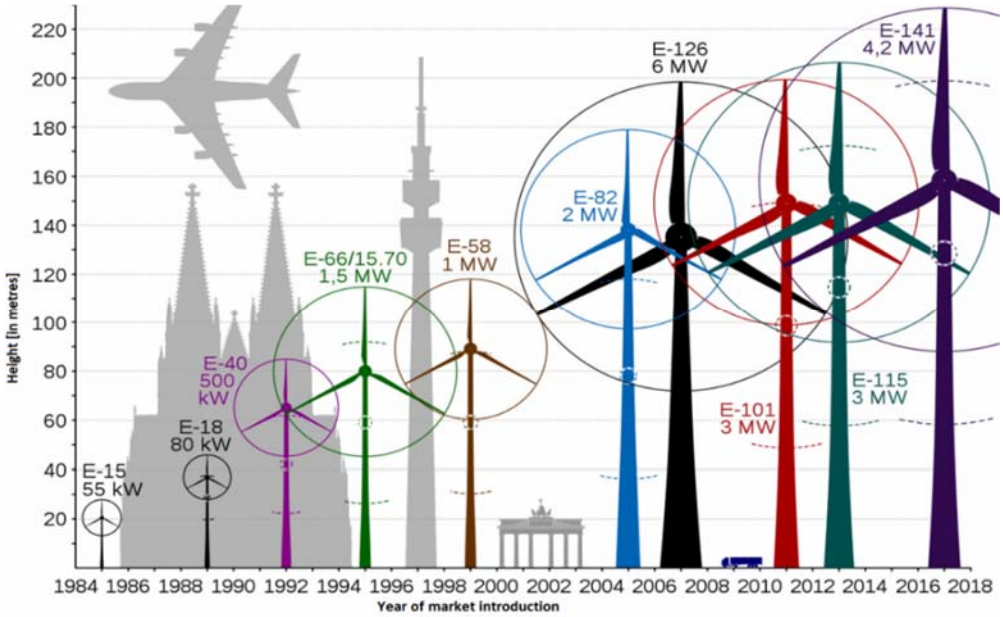

Figure 1.1: The increment of energy and turbine dimensions over time[1].

[1] Source: https://www.cleanenergywire.org/factsheets/german-onshore-wind-power-output-business-and-perspective

As installed wind energy capacity increases, individual wind turbine capacity is increasing, partly through increased hub-height and partly through increases in the swept area (Figure 1.1). Wind turbine blade length has increased from around 20m in 1990 to over 40m in 2018. The average rotor diameter of a wind turbine installed in the US in 2016 was 103 m [WISER, 2016]. For a given blade angular velocity w_a, the tip velocity increases dramatically if the blade length increases substantially, given that $U_t = Lw_a$, where U_t is the tip speed and L is the length of the blade. According to Keegan, [2014], it is commonplace for large wind turbines to have a tip velocity of $80ms^{-1}$ in operation. For offshore wind turbines, the size is typically larger [Barthelmie, Hansen, and Pryor, 2013]. The only currently installed offshore wind turbines in the US have a capacity of 6 MW and a rotor diameter of 150 m.

Blade Leading Edge Erosion

The cross-section of turbine blades is comprised of different airfoil shapes, which are specifically designed to create lift towards the rotation orientation of the blade (Figure 1.2). The blade is thicker at the hub and decreases in chord towards the tip. This reduces the weight of the blade but allows structural integrity to be maintained near the hub. Blades are typically hollow and made of fiberglass. The blade is usually strengthened by some supporting shell core comprised of foam and wood [Slot et al., 2015]. The leading edge can be strengthened with an additional coating which may extend the lifetime of the blade [Goward, 1986]. Even though such coatings are used to protect the blade from erosion, environmental conditions where

the turbines are installed may still be detrimental enough to eventually negatively reduce the blade performance due to the continued presence of precipitation and abrasive particle-laden wind [Pryor, Spaulding and Barthelmie, 2010].

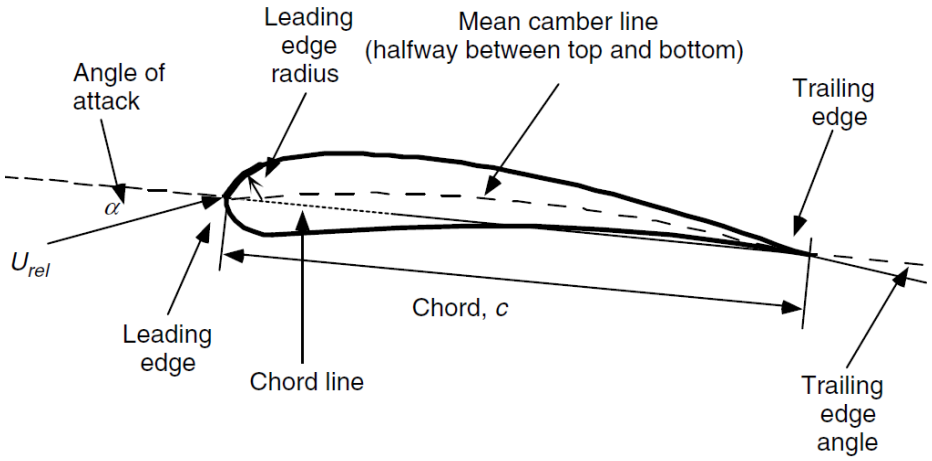

Figure 1.2: Cross-section of a wind turbine blade reproduced from Manwell, McGowan, and Rogers, [2010].

Blade leading edge erosion (LEE) describes damage at the blade leading edge, especially near the tip and the outer third of the blade (Figure 1.2). LEE can be a severe issue in wind turbine operation because the loss of aerodynamic performance through roughening of the blade edge causes a reduction in aerodynamic lift reducing the energy generation efficiency of wind turbines and causes additional maintenance costs. For example, Sareen et al., [2014] reported a total of 5% to 25% annual energy can be lost due to the leading edge erosion. The performance loss is due to the severe surface roughness generated by the erosion of the material on the blade leading edge which compromises the aerodynamic lifts. LEE can be generated by a variety of airborne particles, which can be erosive and influence the aerodynamical condition.

Research to date suggests most of the LEE occurs due to precipitation [Wagner, H. J. 2013]. The erosion is accelerated in the rotor tip region where the rotation speed is very high. Thus the net closing velocity between the falling hydrometeor and the rising wind turbine leading edge is becoming higher. The high-speed rotor tip region is the most important part of the blade in optimum blade performance and energy capture, accounting for more than 1/3 of the total energy capture [Wagner, H. J. 2013].

Figure 1.3: A photograph of the leading-edge erosion. In this example, the turbine blade is suffered to severe leading edge erosion. Photos are extracted from Slot et al., [2015].

Leading edge erosion is caused by the sweeping motion of the wind turbine blade at high velocity impacting with rain droplets, dust, and hail and so on. Other studies [Uematsu and Yamada, 1995; Matteoni and Georgakis, 2012, 2015] have shown that the increasing surface roughness due to leading edge erosion can significantly influence the aerodynamic force coefficients and thereby influence the aerodynamic performance [Almohammadi, Ingham, Ma and Pourkashanian, 2015; Schuerich and Brown, 2012].

Although the detrimental effects of the leading edge erosion are well known, a quantitative and mechanical understanding of the effects of the leading edge erosion on wind turbine performance is still lacking. Some previous studies [Jasinski et al., 1997; Giguère and Selig, 1997; Van Rooij and Timmer, 2003; Fuglsang and Bak, 2004; Somers, 2004; Khalfallah and Koliub, 2004] have investigated the accretion of the roughness on the leading edge due to dust and insect debris. These experimental and computational results, however, can also account for the increased turbine performance loss due to more severe surface roughness generated due to the erosion of the blade leading edge. Recently, some researchers [Ehrmann et al., 2013 & 2017; Ehrmann and White, 2014; Rumsey, 2013; Wilcox and White, 2016] conducted some further experiments to measure the roughness of the wind blades due to severe soiling and erosion and developed models to capture the effects of the surface roughness and erosion on energy capture. The experiments and models were focused on the tip region, where the NACA 633-418, airfoil were used. The results suggest that the occurrence of the roughness greatly reduces the energy capture compared with that harvested by the intact airfoil [Ehrmann et al., 2013 & 2017; Ehrmann and White, 2014].

The formation of the leading edge erosion as an illustration in sketched in Figure 1.4. Figures 1.4 (a)-(c) shows the process of the erosion from pits to gouges and from gouges to delamination.

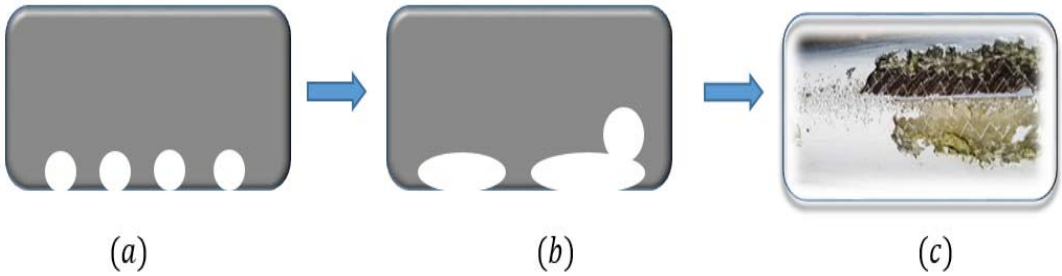

Figure 1.4: A sketch of the formation of the leading edge erosion. In (a), some small pits are formed due to the abrasive particles in the atmosphere, which gradually grows into gouges (b). Subjecting to the natural forces for an extended time, these gouges finally get combined and form the delamination (c).

Rain erosion of the blade usually begins with some small pits in blade's surface by increasing the roughness of the blade wall [Sareen, Sapre, and Selig, 2014]. It is shown that the blade erosion begins with some small pits formed near the blade leading edge, which then form gouges due to the density increase over time. If the gouges are left subject to these natural forces, then they would continue to increase in density, connect to other gouges and finally contribute to the delamination near the leading edge surface [Stinebring et al., 1980; Sareen et al., 2014].

Dalili et al., [2009] studied surface engineering damage to the wind turbine blade due to the icing influence in Nordic climates. It clearly shows that the particle droplet-laden winds can damage the leading edge to a large extent and will seriously reduce the aerodynamic efficiency of the blade. They also discussed several methods to improve blade erosion resistance, such as applying elastomeric materials to the

leading-edge surface and replacing that frequently if the turbine were to run expected years. There are also some discussions on protecting the leading-edge surface elastomers with some nano-sized reinforcement. For instance, Karmouch & Ross, [2010] included silica nanoparticles in an epoxy paint to generate a hydrophobic cover on the blade surface to leverage erosion impact. But even though a plethora of methods have been developed for this, a detailed evaluation of how such approaches perform is still not available in the literature.

In addition, Sayer et al., [2013] investigated the material properties of an 11.6m-long DEBRA-25 turbine blade which had been in operation for over twenty years and stated that the leading edge of the turbine blade had been significantly impacted by the rain droplet erosion. Leading-edge erosion has also been recorded only after two years by the operators, which is early given that the turbines are expected to run over a time span of at least 20 years [Keegan et al., 2013a, 2013b]. Therefore, operators, manufacturers, and repair companies are emphasizing the need for effective inspection and maintenance to enable the satisfactory performance of the turbines. An on-site inspection is routinely undertaken and results in on-site repair if needed. The minor repair can be done while blades are still attached, while more extensive repair may require the additional expense of a crane to remove the blade and return it to the manufacturing center. Very serious damage may require blade replacement.

Precipitation Map of the USA

Wind turbine blades are exposed to environments where a number of detrimental factors contribute to blade erosions. Among these adverse factors, the action of rain droplets occurs in almost all environments and at all times of the year [Sayer et al., 2013]. A precipitation map of the USA based on data from 1981 to 2010 reported by NOAA Climate Data Center is shown in Figure 1.5. Rainfall climates are highly variable. Considering the USA, almost every wind farm site will be expecting some level of precipitation which also varies by season in terms of precipitation type. As shown in Figure 1.5, precipitation is highest in the southeast of the USA which has very few wind turbines installed and along the northwest coast. Much of the northeast has relatively high rainfall (more than 40 inches per year) while the areas with highest turbine installation (Central and Great Plains areas) typically receive 20-40 inches. Louisiana receives precipitation over 60 inches per year, while some inland states even have a lower level of fewer than 10 inches per year. But in general, precipitation is expected at some level in the entire USA, which means that the issue of rain droplet erosion should be considered. However, little published information is available describing quantitatively the impact damage of rain droplets on wind turbine blades.

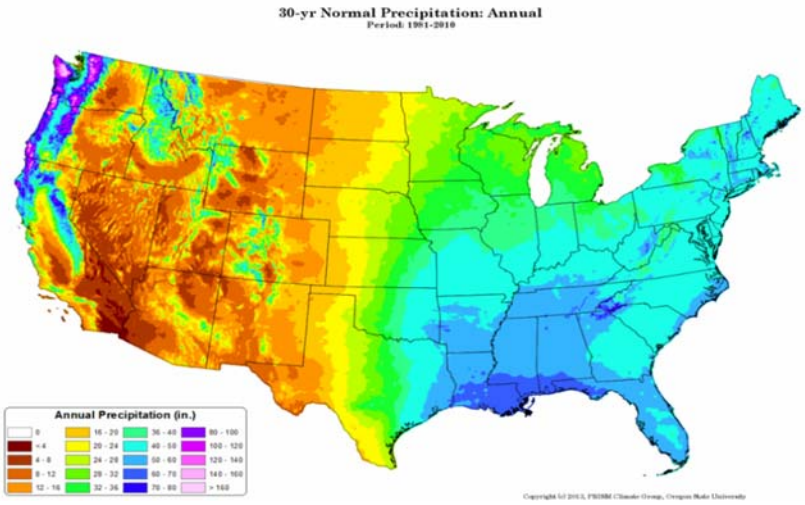

Figure 1.6: Averaged annual precipitation based on data from 1981-2010[2].

However, key aspects of the precipitation climate in terms of potential for leading edge erosion are not only precipitation amount, but also the phase of the precipitation and the size of the hydrometeors. The material response to impacts from solid hydrometeors such as hail is different to that from liquid droplets. The size of the hydrometeors is important since that determines the mass, terminal velocity and the probability that a falling hydrometeor will impact the blade due to material forces or avoid contact with the blade by following the streamline.

Objectives of Thesis

Although some advances have been made towards quantifying the energy captured by the blade from falling hydrometeors, understanding the effects of the

[2] Source: https://climatedataguide.ucar.edu/climate-data/prism-high-resolution-spatial-climate-data-united-states-maxmin-temp-dewpoint

hydrometers on roughness formation and the leading edge erosion remains incomplete. Without knowing the mechanisms that govern the process of the severe roughness formation due to hydrometers or other abrasive aerodynamic particles, it is hard to quantify and predict how much energy loss can be generated for an operational wind turbine. Therefore, the objectives of this thesis are to advance understanding of hydrometeor droplet (rain droplet) impact on wind turbine blade leading edge erosion by quantifying the role of the characteristics of hydrometeors on the roughness formation and energy transition to the turbine blade. As a first step, this thesis contributes to this goal by conducting computational simulations which can be heuristic to guide further laboratory experiments. Therefore, the specific goals of this thesis are:

(1) Build a set of 3D horizontal turbine blade system numerically and analyze the aerodynamic performance of the turbine blade.
(2) Quantify the inflow wind aerodynamics on the turbine performance and compare that under different wind conditions.
(3) Build a set of particle tracking systems in the turbine blade domain.
(4) Examine the rainfall intensity and size on the particle collections by the blade.
(5) Quantify the inflow wind effects on the particle trajectories in the turbine domain.

CHAPTER 2

LITERATURE REVIEW

In this chapter, a two-part review of (i) the rain droplets size distributions under the typical meteorological conditions and (ii) some numerical models in simulating the horizontal turbine blades are presented. With this background, the numerical investigations of the rain droplet on the leading edge erosion in later chapters are conducted.

Rain Texture Models

In meteorology, a rain event is characterized by its intensity and duration [Holton, 1993]. The rain intensity (RR) is expressed as the height of the water accumulated in a specific period of time, which is usually presented in units of millimeter per hour. The rain intensity itself is not enough to quantify the rain droplet on the leading edge erosion, since each rain droplet is of important in shaping the erosion. Therefore, it is necessary to discuss the size and distribution of the droplets in space [Fu et al., 2015].

Rain droplet distribution

In natural conditions, rainfall droplets, referred to herein as particles, are characterized by a distribution of droplet sizes and the number of each radius per unit volume of air. Over the years, numerous rainfall distributions have been proposed and improved [Torres et al., 1994; Stull, 2000; Cugerone and Michele, 2015; Bako et al., 2019]. Among these models, the Marshall-Palmer function [Stull, 2010] is the most commonly used, where the rain droplets conform to

$$\mathrm{N} = \frac{N_0}{I}\exp\left(-IR\right) \tag{2.1}$$

where N is the number of the particles per unit volume, the particles are specified as the particles whose radius is greater than R, $N_0 = 1.67 \times 10^7 m^{-4}$, and $I(m^{-1}) = 8200RR^{-0.21}$ is a function of the rain intensity RR (mmh^{-1}). For the rain intensity from $10mmh^{-1}$ to $160mmh^{-1}$, the droplet size is distributed in Figure 2.1.

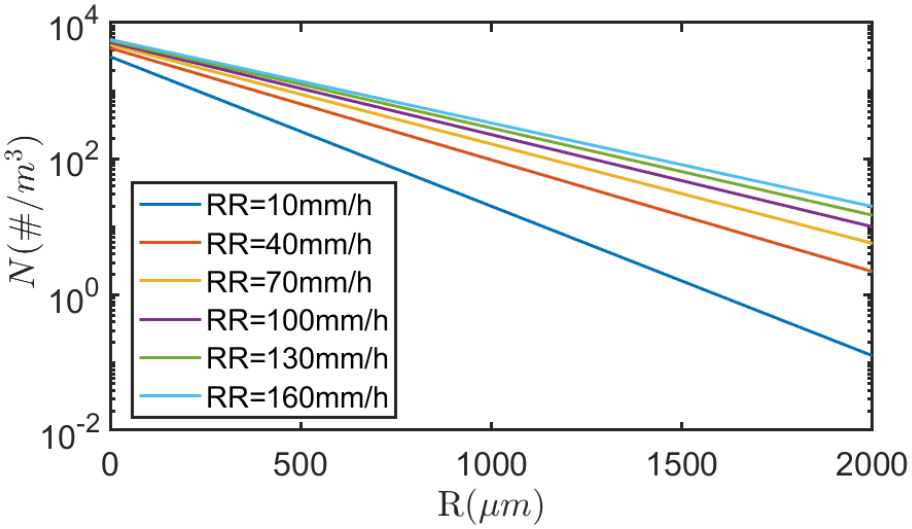

Figure 2.1: The Marshall-Palmer law of the particle size distribution, where the rain intensities are shown in different colors.

It is shown in Figure 2.1 that as rainfall intensity increases, the number of both larger and smaller rain droplets increases, though the change is most marked for the larger radii. Other than the Marshall-Palmer function, there are also some other models [Best, 1950; Marshall & Palmer, 2002; Montero-Martínez et al., 2009] which may provide a better description for some specific rain conditions. For example, the Gamma law from Ulbrich, [1983] proposed for a stratiform rain describes the number of the particles per unit volume as,

$$\mathrm{N} = 6.4 \times 10^{10} D^{4.65} \exp\left(-\frac{8.32}{0.114 RR^{0.11}} D\right) \tag{2.2}$$

where D=2R is the diameter of the rain droplet in millimeter. Equation 2.2 works better than the Marshall-Palmer function for the stratiform rain. However, for general rain and not specific conditions, the Marshall-Palmer function provides better matches between experimental data and predicted curves. Therefore, it is used to describe particle distributions in this thesis. Based on the Marshall-Palmer data, Best [1950] gave a probability density function for the fraction of rain droplet with a diameter smaller than D as,

$$\mathrm{F} = 1 - \exp\left[-\left(\frac{D}{1.31 RR^{0.232}}\right)^{2.25}\right] \tag{2.3}$$

where F is the fraction of water liquid in stagnant air. The probability density function of Equation 2.3 is plotted in Figure 2.2 for a range of different rain intensities.

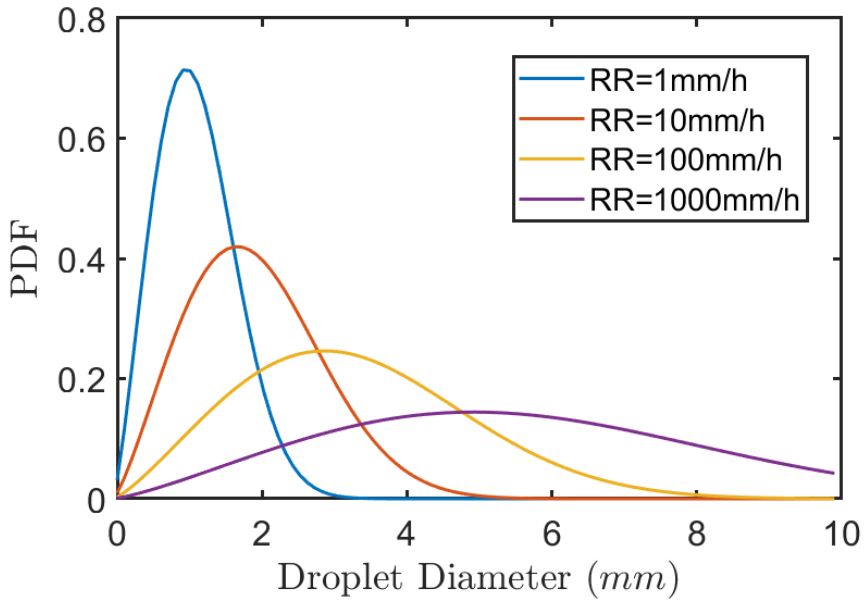

Figure 2.2: The probability density function of the rain size distributions for different rain intensity versus different droplet diameter from Equation 2.3

It is shown in Figure 2.2 that as the rain intensity becomes larger, the median droplet diameter (D_{50}) increases, which conforms to our intuition. Other than the fraction distribution function, the D_{50} diameter can also be predicted described by two empirical power- and exponential laws respectively [Mahadi and Zulkifli, 2017]:

$$D_{50} = 1.483RR^{0.176} \quad (2.4a)$$

$$D_{50} = 3.270 - 1.631\exp(-0.04RR) \quad (2.4b)$$

The comparison between the prediction and the experimental data [Varikoden et al., 2010; Mahadi and Zulkifli, 2017a, 2017b] is shown in Figure 2.3. It is shown in Figure 2.3 that the D_{50} value increases as the rain intensity increases, which is consistent with Equation 2.3 and Figure 2.2.

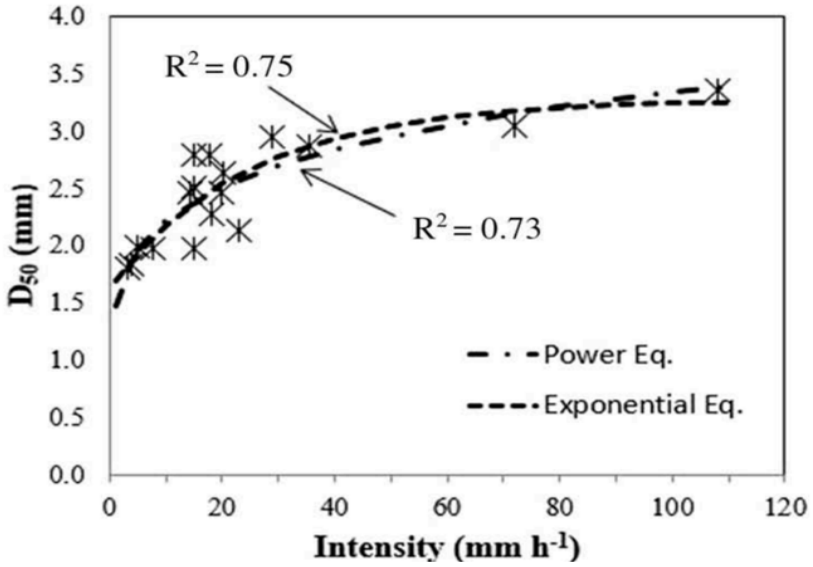

Figure 2.3: The distribution of the fraction of rain droplet with a diameter smaller than D for different rain intensity versus different droplet diameter. Reproduced from Mahadi and Zulkifli, [2017a, 2017b]. The power- and exponential equations in this figure corresponds to the equations in Equation 2.4 respectively.

Rain droplet terminal velocity

Other than the size distribution function, the terminal velocity of the rain droplets is also important in generating the leading edge erosion, since the kinetic energy of each particle impact is influential in the energy transfer. The terminal velocity of a falling rain droplet is influenced by many factors such as climatic conditions, meteorological responses and the local hydrological factors, which is therefore hard to quantify. Gunn and Kinzer, [2002] conducted a substantial number of experiments in 1949 and measured the terminal velocities of the water droplet through the stagnant air. Their

results are shown in Figure 2.4. It indicates that the terminate velocity increases as the particle diameter increases.

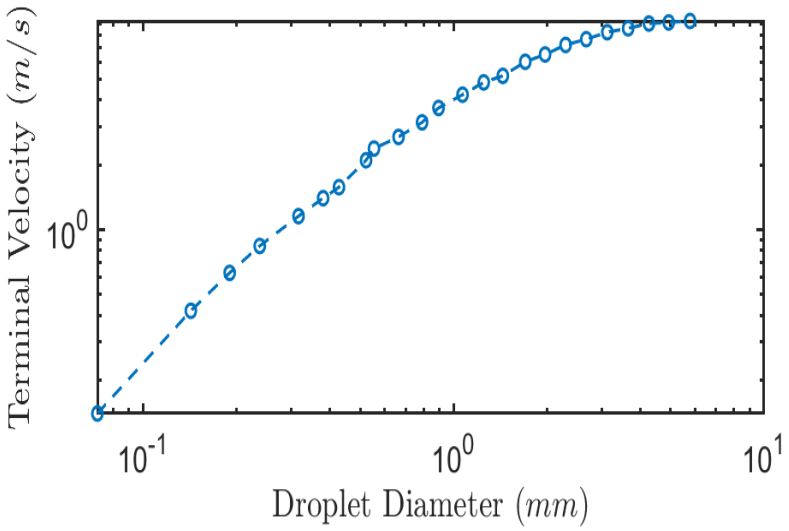

Figure 2.4: Terminal velocity of very small droplets from measurements in Gunn and Kinzer, [2002]. The droplets size varies from 0.1mm to 10mm .is shown in Figure 2.4.

In practice, the particle terminal velocity (V) for a limited range of particle sizes can be determined using an empirical equation from [Stull, 2000]:

$$\mathrm{V} = -\mathrm{c}\left[V_0 - \exp\left(\frac{R_0 - R}{R_1}\right)\right] \tag{2.5}$$

where the three parameters are given as $V_0 = 12m/s$, $R_0 = 2.5mm$ and $R_1 = 1mm$. The parameter c is a density correction factor, which can be estimated using $\mathrm{c} = \sqrt{70/P}$, where P is the ambient pressure.

In summary, Equations 2.1 to 2.5 provide fundamental equations to describe rainfall events. For a given rainfall intensity, the size distribution of rain droplets can be determined and the terminal fall velocity can be estimated. In the following section, numerical simulations of the horizontal turbine blade or 2D airfoil are reviewed, which provides the background of the 3D wind turbine simulations under the rain droplet conditions discussed in the following chapters.

Turbine Blade Simulations

2D airfoil simulations

With the recent advance in numerical techniques, it has become possible to study complex aerodynamic phenomena through computational fluid dynamics (CFD). As a first step into this question, it is necessary to review some advancements in the airfoil field, since studies on wind turbine blade erosion are rather limited. However, in other fields such as aircraft engineering, there are many researchers who have investigated the erosion issue in terms of the flight airfoil through some 2D experiments and simulations. For example, Cai, Abbasi, and Arastoopour, [2013] analyzed the airplane airfoil aerodynamic performance in heavy rain using several 2D CFD simulations. In their simulations, the discrete phase model (DPM) was used, where the rain droplets were simulated by a few small balls characterized by a specific diameter and a total mass flow rate in the unit of kilogram per second. Based on the 2D simulation, Cai, Abbasi, and Arastoopour, [2013] show that the flight performance is greatly influenced by the rainfall, where there are significant aerodynamic penalties

under heavy rain conditions. The momentum of airflow from the wings to the flight body is significantly impacted by the adhered water which increases the effective mass of the wings and body, thus changing the wing's inertial moment. Moreover, droplets can also increase the surface roughness of the flight surface, thus increasing the aerodynamic drag and reducing lift.

However, the aforementioned simulations are not representative of the real airfoil, since the simulating domain is only a cross-section. As indicated in Chapter 1, the airfoil may have different cross-sections in different locations, which indicates the 2D simulation might be flawed in such cases. Also, the airfoil is assumed to be stationary or at least moving in straight line, which is not always the case, as the flights are continually adjusting the elevation and orientation of the airfoil when the impact of the rain droplet may be most significant [Langtry et al., 2006; Wu, Lv and Cao, 2019].

Furthermore, Wang et al., [2019] investigate the effects of the leading-edge deformation with an S809 airfoil and shows that the aerodynamic coefficients and flow fields are very sensitive to the leading-edge defect both in steady and unsteady conditions. The sketch of the airfoil is shown in Figure 2.5. The simulation was conducted using the SST $k\sim\omega$ model, where the residual errors of the iteration are controlled below 10^{-6}. They show that when the leading edge defect has a relatively smaller influence on the aerodynamic characteristics if the defect thickness t is less than $0.06t_c$. They also conclude that that the flow field and pressure contour do not

change substantially even when the defect thickness varies from $0.06t_c$ to $0.25t_c$. Finally, they indicate that the flow in the vicinity of the defective airfoils is featured by the intense trailing edge vortex and separation bubble.

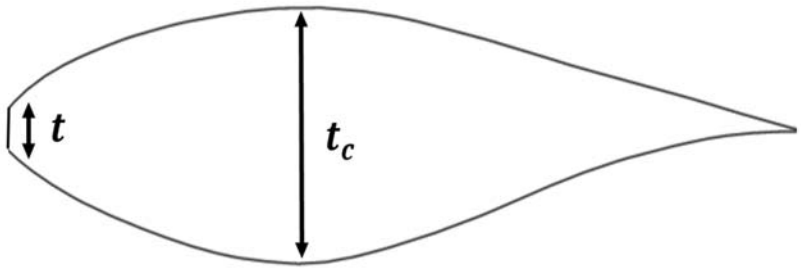

Figure 2.5: The sketch of the airfoil used by Wang et al., [2019]. The deformation thickness is represented with t and t_c is the thickness of the airfoil.

In addition to the shape of the airfoil and the damage extent, the angle of attack is another important factor in leading edge erosion. Since the suspended particles in a fluid flow can usually be described by a Stokes number, Li et al., [2018] investigated the effects of the particle Stokes number ($Stk = \tau u/l$, where τ is a particle characteristic time scale, u is the local velocity and l is a characteristic length scale) on wind turbine airfoil erosion using 2D simulations. If $Stk > 1$, then it is generally assumed that the particle trajectory is influenced by the obstacle. The particles are injected from a specific predetermined line ahead of the airfoil. The simulation is sketched in Figure 2.6. It is indicated that the angle of attack (AOA) plays an important role in particle trapping over the blade surface, which is consistent to the finding by Casari et al, [2018]. The results show that when the AOA becomes larger than 6.1 degrees, no erosion is occurring once the particle Stokes number is lower than

0.0135. Therefore, this Stokes number is deemed as the critical number for the erosion to initiate. Furthermore, it also shows that the erosion threshold is closely related to the particle diameters, particle density and the inflow wind speed. It also indicates that under certain range the critical particle Stokes number increases when the AOA increases. If the Stokes number becomes larger, the extent of erosion also increases. Finally, it is concluded that airfoil erosion is heavily impacted by the high surface pressure in a 2D simulation of an airfoil in a modeled wind tunnel.

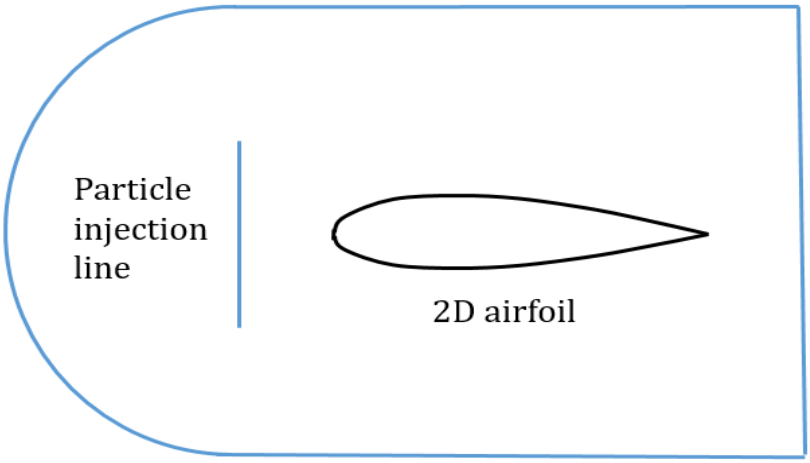

Figure 2.6: The sketch of the airfoil and particle injection experiment used by Li et al., [2018]. The particles are injected as a linear group ahead of the airfoil.

However, it is not clear how many particles can be collected or trapped to the airfoil in this simulation. Since erosion can be significant in the environment when the humidity and precipitation are high, it is necessary to quantify to what extent the rain droplets can contribute to the erosion process. Therefore, further work is needed to investigate these factors.

3D horizontal turbine simulations

It is obvious that 2D simulations are not representative enough to describe the particle movement in the vicinity of the blade. In the 2D simulations, the airfoil is stationary [Cai, Abbasi, and Arastoopour, 2013; Li et al., 2018; Casari et al, 2018], which is different from the practical rotating blade cases. However, most CFD studies are focused on the 2D blade profile, which cannot consider the effects of the airflow and the particle movement in the radial direction. For 3D simulations, Shu et al., [2018] used CFD models and investigated the aerodynamic performance of the turbine blade after icing. In their simulations, a three-blade horizontal turbine is used, which is shown in Figure 2.7.

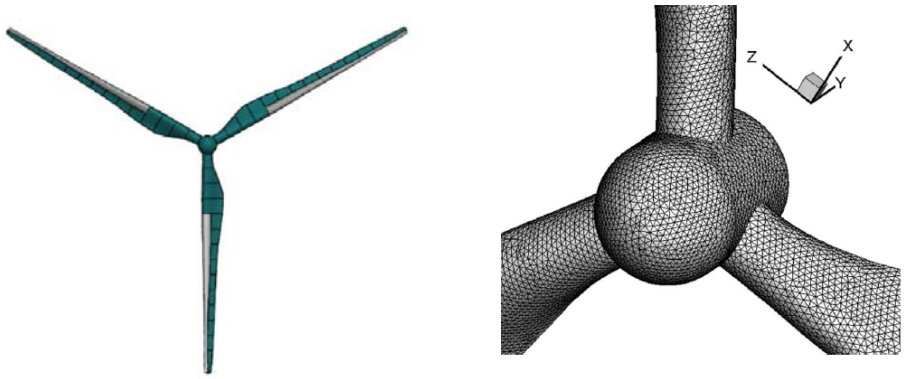

Figure 2.7: The sketch of the three-blade horizontal turbine. The right figure shows the meshes on the blade. Note that these figures are extracted from Shu et al., [2018].

It is shown in Figure 2.7 that the turbine is represented with a three-blade wall. The ice condition is simulated by different roughness on the surface. The results show that the ice shape can also influence the pressure distribution of the leading edge of the

airfoil, which is not surprising since the ice can act as a form of roughness on the blade. The ice which is covered on the blade can significantly reduce the energy output. This simulation also shows that the increasing wind speed can decrease the normal force and tangential force up to 89% in the radial direction. This finding, however, cannot be deduced from the 2D simulations, since the radial forces cannot be considered in 2D airfoils [Duque et al., 2003; Sezeruzol and Long, 2006; Li et al., 2012; Sørensen et al., 2013; Shu et al., 2018].

In this thesis, the 3D domain is used to simulate the particle impact on leading edge erosion of the turbine blade. Since the rain droplets have been shown to significantly influential in the formulating the leading edge erosion, this thesis proposes to investigate the influence of the rain droplets. We aim at building a 3D turbine blade simulation system and using that to quantify the influence of the particles on the developments of the leading edge erosion of the turbine blade. Therefore, in the following chapter, the numerical simulation theory and techniques are discussed in detail.

CHAPTER 3

TURBULENT AND PARTICLE TRACKING MODELS

In this chapter, the governing equations for the turbulent simulations are discussed. The governing equation for the wind flow is based on the Navier-Stokes equation in a multiple-reference coordinate system. The turbulent model used to simulate the wind flow in the blade domain is based on the $k\sim\omega$ model. The basis of Navier-Stokes equations and the $k\sim\omega$ model are discussed in this section. All of the equations used in this chapter are given and explained from the ANSYS Theory Guide, [15.2]. Some important equations for the turbulent model that are used in the current simulations are extracted and listed in the following sections.

Governing Equations

The governing equations used in ANSYS 19.2 are derived based on the commonly-used Navier-Stokes equation group [ANSYS Theory Guide, 15.6]. The difference here lies in that the equations are formulated with rotating reference coordination. For a fixed stationary control volume, the conservation of mass gives,

$$\frac{\partial \rho}{\partial t} + \nabla \cdot \rho \vec{u} = 0 \tag{3.1}$$

where t is the time, ρ is the air density, $\vec{v}$ is the velocity vector, and p is the static pressure and $\nabla = \frac{\partial}{\partial x} + \frac{\partial}{\partial y} + \frac{\partial}{\partial z}$ is the gradient calculation sign.

The conservation of the momentum provides,

$$\frac{\partial(\rho\vec{u})}{\partial t} + \nabla \cdot \rho(\vec{u}\vec{u}) = -\nabla p + \nabla \cdot \bar{\bar{\tau}} \tag{3.2}$$

where t is the time, ρ is the air density, $\vec{v}$ is the velocity vector, and p is the static pressure and $\bar{\bar{\tau}}$ is the shear stress vector given as,

$$\bar{\bar{\tau}} = \nu\left[(\nabla\vec{u} + \nabla\vec{u}^T) - \frac{2}{3}\nabla \cdot \vec{u}I\right] \tag{3.3}$$

where ν is kinetic viscosity and I is the unit tensor.

Applying Equations 3.1 and 3.2 to a rotating domain, the mass conservation equation becomes,

$$\frac{\partial\rho}{\partial t} + \nabla \cdot \rho\overrightarrow{u_r} = 0 \tag{3.4}$$

and the equation of the conservation of momentum yields,

$$\frac{\partial(\rho\overrightarrow{u_r})}{\partial t} + \nabla \cdot \rho(\overrightarrow{u_r}\,\overrightarrow{u_r}) + \rho(2\overrightarrow{\omega_r} \times \overrightarrow{u_r} + \overrightarrow{\omega_r} \times \overrightarrow{\omega_r} \times \vec{r}) = -\nabla p + \nabla \cdot \bar{\bar{\tau_r}} \tag{3.5}$$

where r is the variable in the radius direction, $\overrightarrow{u_r} = \vec{u} - \overrightarrow{\omega_r} \times \vec{r}$ is the relative velocity (the velocity viewed from the moving frame) and $\overrightarrow{\omega_r}$ is the angular velocity, $(2\overrightarrow{\omega_r} \times \vec{r})$ is the Coriolis force and $(\overrightarrow{\omega_r} \times \overrightarrow{\omega_r} \times \vec{r})$ is the centripetal acceleration. The shear stress is calculated using the SST *k~ω* model.

SST k~ω Model

The stationary shear-stress transport (SST) *k~ω* model [Li et al., 2012] is used for the wind turbulence simulation due to its advantage in addressing the low-Reynolds

number effects and shear flow spreading. The k~ω model is an empirical turbulent model based on the turbulent kinetic energy (k) and the dissipation rate (ω). The transport equations for the k and ω are given as

$$\frac{\partial(\rho k)}{\partial t} + \frac{\partial(\rho k u_i)}{\partial x_i} = \frac{\partial}{\partial x_j}\left(\Gamma_k \frac{\partial k}{\partial x_j}\right) + \widetilde{G_k} - Y_k + S_k \tag{3.6}$$

$$\frac{\partial(\rho \omega)}{\partial t} + \frac{\partial(\rho \omega u_j)}{\partial x_j} = \frac{\partial}{\partial x_j}\left(\Gamma_\omega \frac{\partial \omega}{\partial x_j}\right) + G_\omega - Y_\omega + G_\omega + S_\omega \tag{3.7}$$

where $\widetilde{G_k}$ denotes the generation of the turbulent kinetic energy due to mean velocity gradients, Y_k and Y_ω denote the dissipation terms due to turbulence [*ANSYS Theory Guide*m 15.6], G_ω denotes the dissipation of the turbulent kinetic energy due to mean velocity gradients , D_ω represents the cross-diffusion term, Y_k and Y_ω denote the dissipation due to turbulence, S_k and S_ω represent two source terms respectively. These terms are given as,

$$\Gamma_k = \mu + \frac{\mu_t}{\sigma_k} \tag{3.8}$$

$$\Gamma_\omega = \mu + \frac{\mu_t}{\sigma_\omega}$$

where σ_k and σ_ω are the turbulent Prandtl numbers given as,

$${\sigma_k}^{-1} = \frac{F_1}{\sigma_{k,1}} + \frac{1 - F_1}{\sigma_{k,2}} \tag{3.9}$$

$${\sigma_\omega}^{-1} = \frac{F_1}{\sigma_{\omega,1}} + \frac{1 - F_1}{\sigma_{\omega,2}} \tag{3.10}$$

and μ_t is a turbulent viscosity term computed using

$$\mu_t = \frac{\rho k}{\omega} \frac{1}{\max\left[\frac{1}{\alpha^*}, \frac{SF_2}{\alpha_1 \omega}\right]} \tag{3.11}$$

and α^* is a coefficient depending on the turbulent viscosity and Reynolds number,

$$\alpha^* = \alpha_\infty^* \left(\frac{Re_t + \alpha_0^* Re_k}{Re_t + Re_k} \right) \tag{3.12}$$

The Reynolds number terms are defined as follows from the *ANSYS Theory Guide* [15.6],

$$Re_t = \frac{\rho k}{\mu \omega};\ Re_k = 6 \tag{3.13}$$

The other relevant parameters are given in the *ANSYS Theory Guide*. Therefore it is not repeated here. In summary, Equations 3.6 to 3.13 provides the basis for the turbulent models, which are embedded in the finite volume method for the aerodynamics simulations. The turbulent production terms are given in the following section.

For the modeling of the turbulent production terms, the details can be found on the ANSYS Theory Guide, [15.6]. Only some key information is listed in this section. The turbulent kinetic energy production term $\widetilde{G_k}$ is modeled as,

$$\widetilde{G_k} = \min(G_k, 10\rho\beta^* k\omega) \tag{3.14}$$

where G_k is calculated with,

$$G_k = -\rho \overline{u_i' u_j'} \frac{\partial u_j}{\partial x_i} \tag{3.15}$$

Or using the Boussinesq hypothesis, the production term G_k can be derived as,

$$G_k = \mu_t S^2 \tag{3.16}$$

The production G_ω is given by,

$$G_\omega = \frac{\alpha}{\nu_t} \widetilde{G_k} \tag{3.17}$$

Since the other parameters are stationary variables which can be found from any Turbulence book, therefore they are repeated here. The details of the models for ANSYS simulations can be found in the ANSYS Theory Guide, [15.6]. The dissipation term of *k* is defined as,

$$Y_k = \rho\beta^* k\omega \tag{3.18}$$

where the parameter β is given by

$$\beta_i = F_1\beta_{i,1} + (1 - F_1)\beta_{i,2} \tag{3.19}$$

The cross-diffusion term comes from the stationary *k~ω* model, which is modified and defined as,

$$D_\omega = 2(1 - F_1)\rho\frac{1}{\omega\sigma_{\omega,2}}\frac{\partial k}{\partial x_j}\frac{\partial \omega}{\partial x_j} \tag{3.20}$$

The other constants used in the ANSYS simulations are specified as follows, which are used to validate the simulation model, as suggested by the ANSYS Theory Guide, [15.6].

$$\begin{gathered}\sigma_{k,1} = 1.176;\ \ \sigma_{k,2} = 1.0;\ \sigma_{\omega,1} = 2.0;\ \sigma_{\omega,2} = 1.168 \\ a_1 = 0.31;\ \beta_{i,1} = 0.075;\ \beta_{i,1} = 0.0828\end{gathered} \tag{3.21}$$

Equations 3.14 to 3.21 provide the production and dissipations terms for the turbulent models. The wind turbine aero dynamical simulations are based on Equation 3.1 to 3.20. In this following section, the governing equations for the particle tracking model are discussed. The particle tracking model is based on the discrete phase model, which has been tested and applied to many engineering applications [Mezhericher, Brosh, and Levy, 2011; Safaei et al., 2014].

Discrete Phase Model

In this work, the rain droplet particles are simulated by the discrete phase model (DPM), where the rain droplets are dispersedly traced in a Lagrangian reference frame. It is to be noted that the DPM is only valid for the domain where the volume fraction is lower than 10% so that the particle-particle interactions and the impact of the particle volume fraction on the fluid transport can be neglected. The particle in DPM is simply represented with a sphere. The sphere is considered as a mass point with a known radius value R.

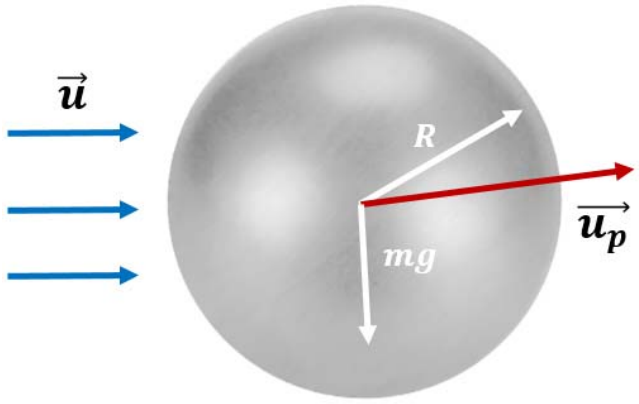

Figure 3.1: A sketch of the modeled rain droplet sphere. The particle has a radius of R and a mass of m. Here g is the gravitational acceleration, $\overrightarrow{u_p}$ is the particle velocity and $\vec{u}$ is the free flow velocity.

The trajectories of a discrete phase rain droplet particle are predicted based on the total force exerted on the particle. Using Newton's second law, the forces acting on the particles can be linked as,

$$\frac{du_p}{dt} = F_D\left(\vec{u} - \overrightarrow{u_p}\right) + \frac{\vec{g}(\rho_p - \rho)}{\rho_p} + \vec{F} \tag{3.22}$$

where $\vec{u}$ is the flow velocity, $\overrightarrow{u_p}$ is the particle velocity, ρ_p is the density of the particle, ρ is the density of the fluid, $\vec{g}$ is the gravitational acceleration, $\vec{F}$ is the additional acceleration term and F_D is the drag force which is computed as,

$$F_D = \frac{9\mu}{2\rho_p R_p^2}\frac{C_D Re}{24} \tag{3.23}$$

where μ is the fluid viscosity, C_D is the drag coefficient, R_p is the radius of the particle and Re is the Reynolds number defined as,

$$Re = \frac{2\rho R_p}{\mu}\left|\vec{u} - \overrightarrow{u_p}\right| \tag{3.24}$$

The additional acceleration term is generated due to the "virtual mass" force, which is required to accelerate the flow near the surrounding particles:

$$F = \frac{1}{2}\frac{\rho}{\rho_p}\frac{d}{dt}\left(\vec{u} - \overrightarrow{u_p}\right) \tag{3.25}$$

The particles are injected over the inlet and the inlet top surfaces, with a specific predetermined velocity. The self-rotation of the particles is not considered in this work. It is also assumed the interaction between particles and the effects of the particles [Bewley, Saw, and Bodenschatz, 2013; Bewley, Sreenivasan, and Lathrop, 2008; Saw et al., 2014] to the precipitation and other turbulence-related phenomena can be neglected in this work.

Boundary conditions

Inlet and outlet condition

As we are simulating scenarios in which a uniform wind is flowing from the inlet boundary to the outlet boundary, blowing through swept area of the wind turbine blade, the inflow free surface wind is represented with a constant velocity U_0. The outlet condition is the free pressure condition (the local pressure equals the free atmosphere pressure), where the outflow velocity is to be determined.

Wall condition

The blade surface is assumed as a rough wall, so that the no-slip boundary condition is applied, which is,

$$\overrightarrow{u_r} = 0 \tag{3.26}$$

$$\nabla \cdot \overrightarrow{u_r} = 0 \tag{3.27}$$

Since we are only simulating 1/3 of the entire domain, periodic conditions will be applied to the interfaces. It will be presented in the numerical setup section.

Particle condition

The particles in the wind flow are given an initial velocity, which will then be coupled in the flow field. The particle initial velocity is decomposed into two

components, one in the vertical direction and the other in the horizontal direction. The horizontal component is the uniform inflow wind speed as stated. The vertical rain droplet falling velocity is given by Stull [2000]:

$$\mathrm{V} = -\mathrm{c}\left[V_0 - \exp\left(\frac{R_0 - R}{R_1}\right)\right] \tag{3.29}$$

where the three parameters are given as $V_0 = 12m/s$, $R_0 = 2.5mm$ and $R_1 = 1mm$, according to Stull [2000]. The parameter c is a density correction factor, which can be estimated using $\mathrm{c} = \sqrt{70/p}$, where p as before is the static pressure.

Equation 3.29 is derived based on the balance between the particle gravity and the frictional drag when the gravitational pull on the droplet is transmitted to the ambient air through frictional drag. For the ambient air pressure of $70kpa$, Equation 3.27 is plotted in Figure 3.2.

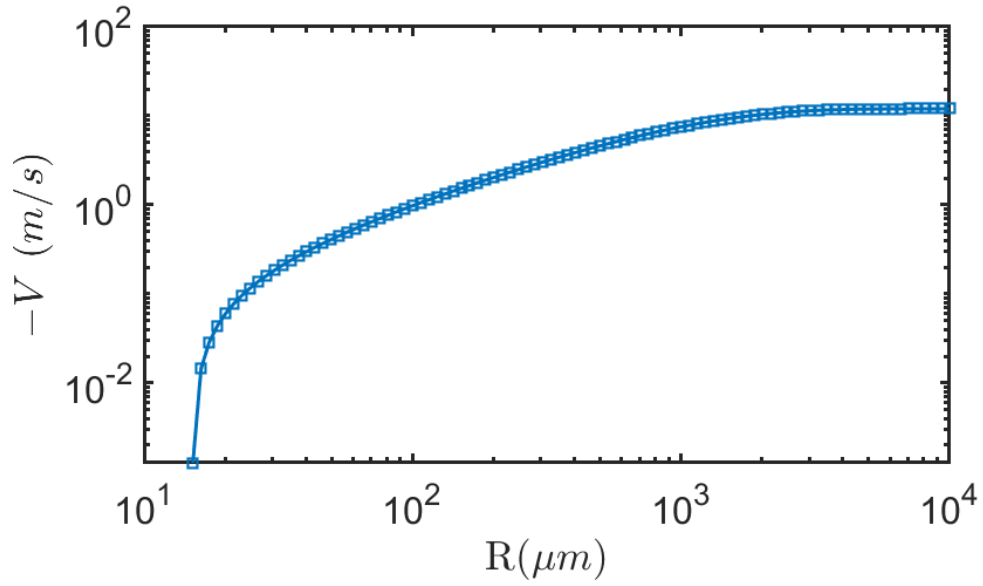

Figure 3.2: Particle terminal velocity for a particle with a radius of R. The velocity is computed according to Equation 3.29.

Figure 3.2 shows that larger particles have larger terminal velocities. However, when the particle radius is larger than 1 mm, the terminal velocity of larger particles increases slowly. The equations presented in this chapter provides the governing equations that can be used to simulate the rain droplets and the airflow over the wind turbine domain. The interactions between particles and the blade are assumed of three scenarios, as shown in Figure 3.3.

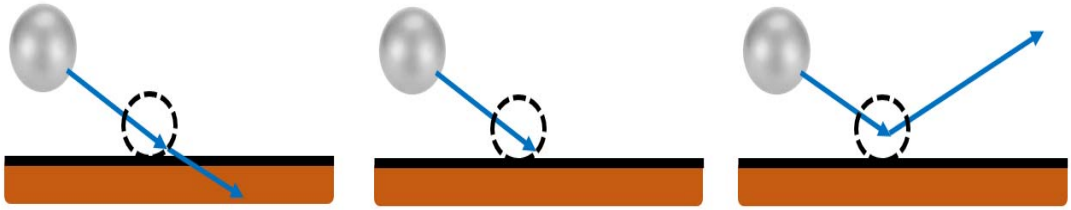

Figure 3.3: The interaction between particles and the blade surface. Three scenarios are assumed: (a) the escape case, (b) the trap case and (c) the reflect case.

The interactions between the particles and the blade can have three different scenarios. The escape case, when the rain droplet leaves the flow domain without hitting the blade. The trap case, where the rain droplet is collected on the blade. And the reflect case when the rain droplet bounds off the blade surface and moves in a different direction. Since many particle and blade material properties are not known, the reflect case is currently not considered. In the next chapter, the numerical set up is conducted and the application of the equations in this chapter is also discussed.

CHAPTER 4

GEOMETRY AND MESHES OF TURBINE DOMAIN

To simulate the flow around the blade, the governing equations discussed in the previous chapter are used. The open-source software ANSYS 19.2 is used as the platform for conducting the simulations. Before solving the equations, ANSYS requires users to build the geometry and mesh for the simulation. The geometry for the 3D wind turbine is assumed as a truncated cone [Simcafe, 2019], where two inlet and outlet conditions are applied to define the boundary of the domain. The original geometry and mesh files are downloaded from the Simcafe, [2019] website. The details of the simulation conditions are specified in this chapter.

Numerical setup

Computational domain

As shown in Figure 4.1, the computational domain is set as a circular truncated cone, where the blade is attached along the x direction in the origin. The conical shape is used to reduce the domain size while maintain a good accuracy of the calculation [Cao, 2011]. The wind comes along the $(-z)$ direction with a uniform velocity of U.

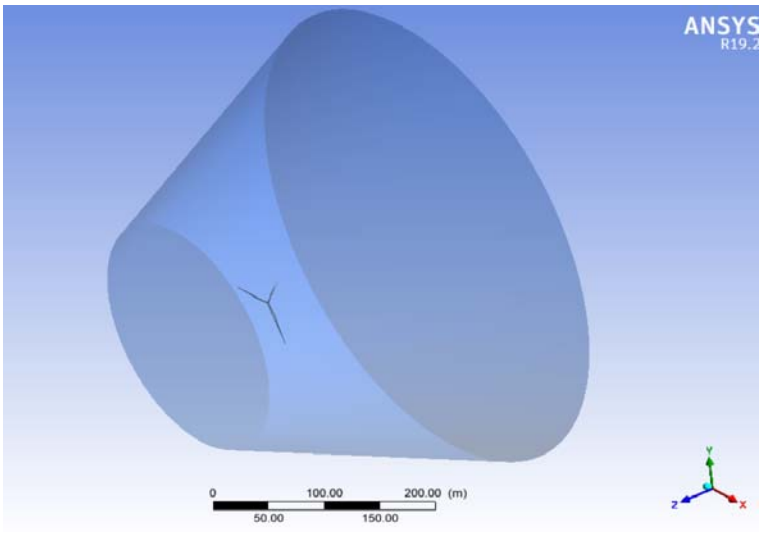

Figure 4.1: A 3D representation of the computational domain of the turbine blades.

To be clear, two 2D side views of the domain and blade are also plotted and thereby shown in Figure 4.2.

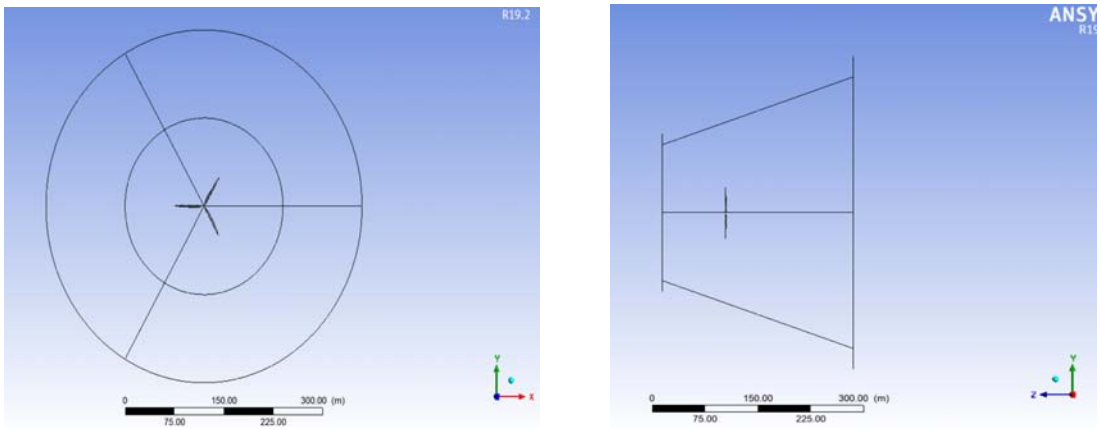

Figure 4.2: The two side views of the computational domain and the turbine blades. Left: This figure is plotted from the (− z) direction. Right: This sketch is made from the lateral (-y) direction.

As it is shown in Figure 4.1 and 4.2 that, a three-blade horizontal wind turbine is used in the simulation. It is observed that each one of the three blades occupy the same space and are spinning in the same rotating velocity, which is $\overrightarrow{\omega_r}$, therefore, only 1/3 of the entire domain is used in the numerical simulations. So that the computational burdens are greatly reduced. Now the new computational domain is shown in the following Figure 4.3.

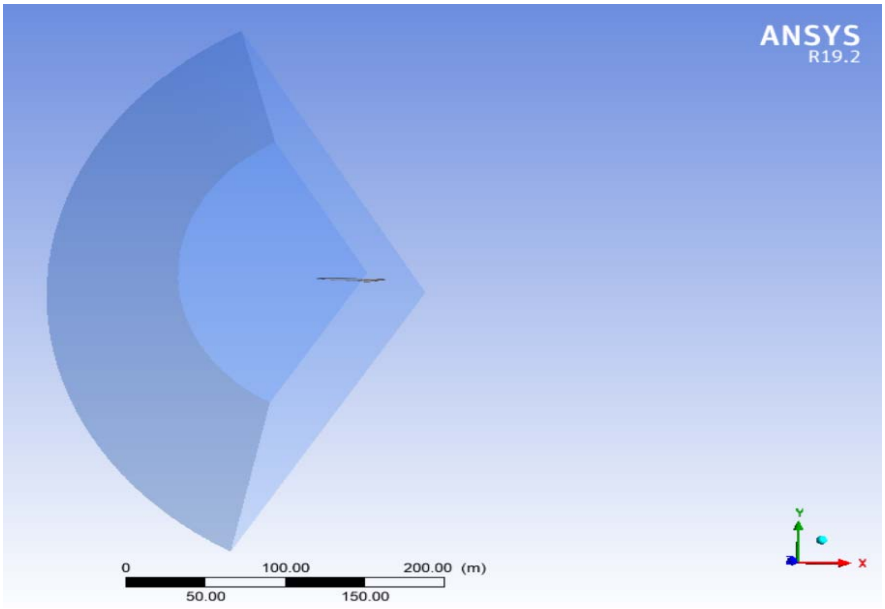

Figure 4.3: A simplified 3D representation of the computational domain and the turbine blade used in this work. The domain as we can compare it with that in Figure 4.1, is 1/3 of the entire circle domain.

Moreover, the names of each surface in the computational domain are shown in Figure 4.4.

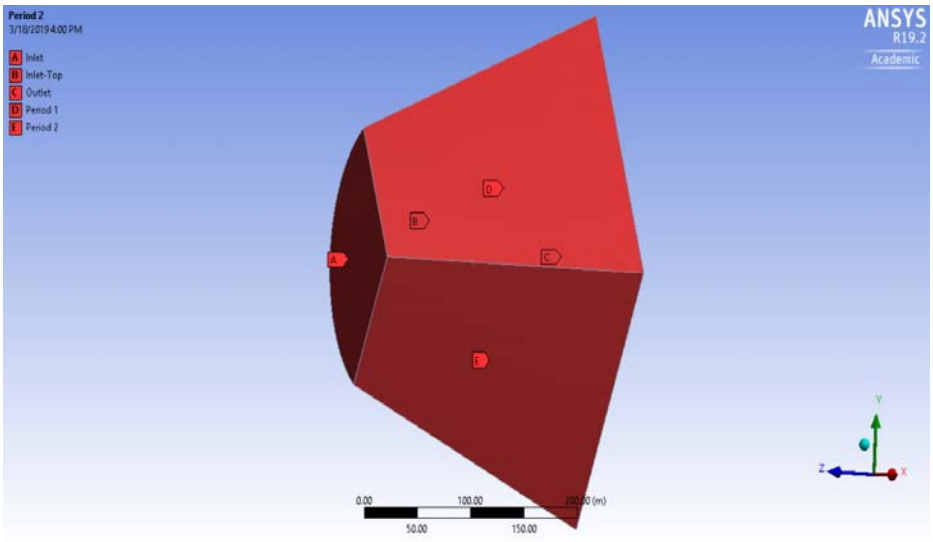

Figure 4.4: The names of each surface of the computational domain. The surfaces are termed inlet (A), inlet-top (the lateral of the cone) (B), outlet (C) and periodic wall 1 (D) and 2 (E) in this domain.

Periodic boundary condition

Since we are only simulating 1/3 of the truncated circular cone, it is, therefore, necessary to use periodic conditions for the periodic walls 1 and 2. A sketch of the front view of the circle domain is shown in Figure 4.5.

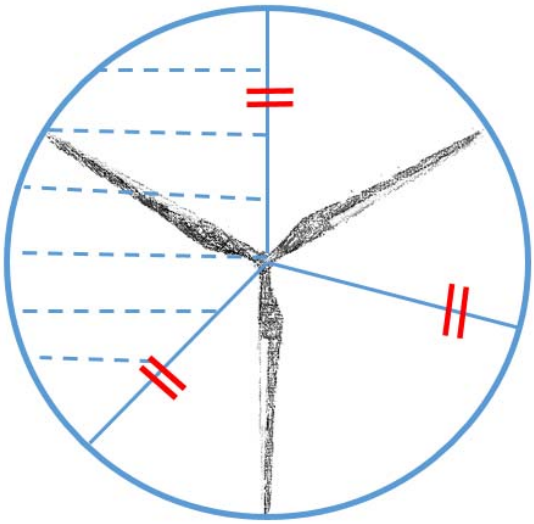

Figure 4.5: The front-view sketch of the computational domain. It is to be noted that only the shaded part is used in the numerical simulation. The periodic condition is performed on the two sides of the shaded area which are denoted with the "=" sign.

As we only simulate 1/3 of the circular domain, therefore the periodic boundary condition is exerted on the 1/3 domain. The periodic condition is expressed with the following equation:

$$\overrightarrow{u_r}(r_1, \theta) = \overrightarrow{u_r}(r_1, \theta - 120°n) = 0 \qquad (4.5)$$

with $n = 1,2,3$ ... where θ is the rotating angle.

Equation 3.5 means that the velocity profiles at the angle of $\theta = 0$, $\theta = 120°$, $\theta = 240°$ and $\theta = 360°$ are the same. If we use θ_1 and θ_2 to represent the two periodic boundaries of the 1/3 domain, then we have the expression that $\overrightarrow{u_r}(r_i, \theta_1) = \overrightarrow{u_r}(r_i, \theta_2)$.

Numerical Assumptions

Before conducting the numerical simulations, a few key assumptions are stated in the following:

First, steady-state conditions are assumed for the wind turbine turbulence, since we are interested in the steady state when the wind flow has been fully developed. Thermal effects are not considered in current simulations; therefore, the air density is set as a constant. This is used to ensure the incompressible flow condition so that the control finite volume method can be applied for the fluid simulations.

Second, the turbine is assumed to have three blades, which are the same. The homogenous flow condition is also presumed so that we can only consider 1/3 of the domains with one blade inside it. The blade is fixed in the middle of the domain and can only rotate around the z-axis, therefore, the angle of attack is constantly changing since the chord line rotates and the inflow wind velocities are of different values.

Third, the wake is non-rotating, and each point on the blade is considered to have the same angular velocity, which is used to make sure that the moving frame technique in ANSYS Fluent can be applied for the simulation. As discussed earlier the rotational speed increases with the radial point along the blade such that it is maximum at the blade tip. However, here the simplifying assumption has been made to permit calculations to be undertaken in the rotating framework.

Finally, the uniform thrust is assumed over the disc and the rotor area, so that the Navier-Stokes equations can be used to simulate the velocity and pressure fields of the fluid through the wind turbine. The static pressure of the inlet and outlet are assumed to equal the undisturbed atmospheric pressure, which is 1atm (=1.01×10^5Pa).

Mesh Generation

The mesh is automatically generated in the ANSYS environment based on the optimized computational efficiency method. The ANSYS mesh is generated considering the available cores and the parallel processing in the computer so that it can significantly reduce the time to create a mesh. To make the result more accurate near the blade, a refined mesh is used in a spherical region around the blade. The detail of the techniques used has been discussed elsewhere [Simcafe, 2019]. It is, therefore, not repeated here, and the mesh in the domain is shown in Figure 4.6.

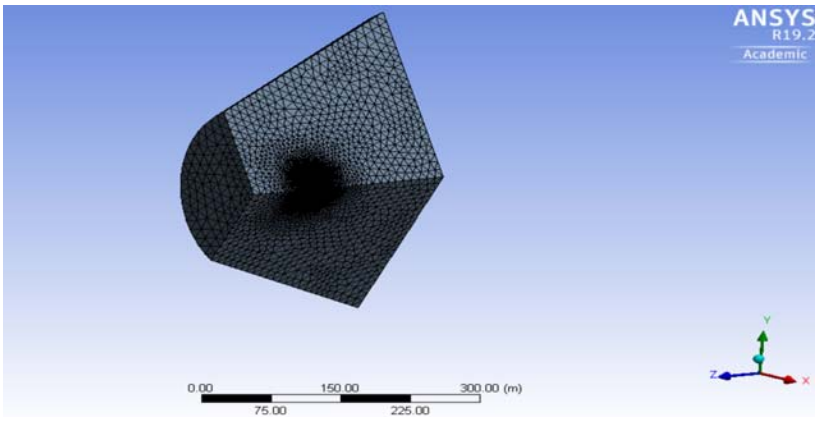

Figure 4.6: The mesh generated in the 1/3 wind turbine domain. The mesh is refined near the blade.

The zoom-in configuration of the blade is shown in Figure 4.7 illustrates the degree of refinement near the center of the blade. Given the focus here is on the trajectories of particles near the blade edge, allowing less detail near the inflow and outflow reduces the computational burden.

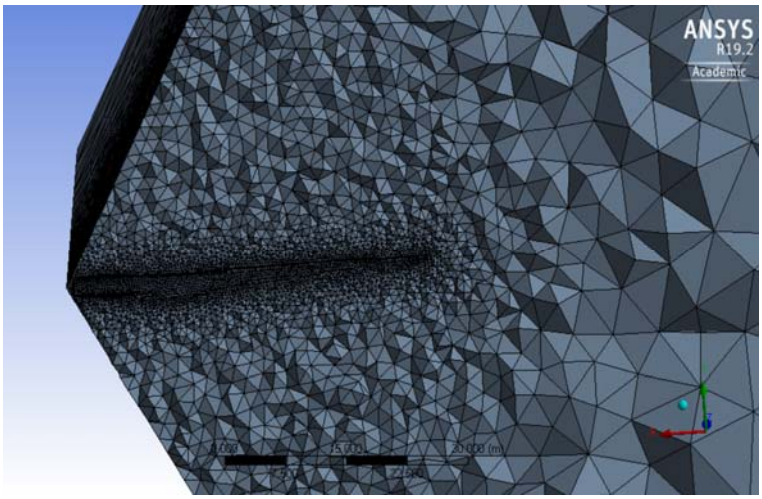

Figure 4.7: The zoom-in configuration of the mesh of the region near the blade.

Geometries of the Domain

Blade configuration

To make sure that a normal velocity of $80m/s$ (which is typical tip velocity for the wind turbine as discussed in Chapter 1) can be achieved near the blade tip, the blade is set as 43.2m in length [Simcafe, 2019]. The root region of the blade is set as a cylindrical shape and it transitions to airfoils S818, S825 and S826 for the root, the body and the tip regions, respectively. The blade has a pitch angle of 4 degrees at the tip and is twisted as a function of radius. The configuration of the blade is shown in Figure 4.8:

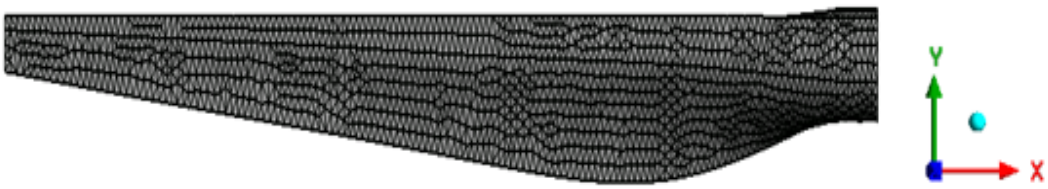

Figure 4.8: The configuration of the blade. As shown in the figure, the blade is circular in the root region, then turns into S818, S825, and S826 airfoil shapes for the root, the body, and the tip regions respectively [Simcafe, 2019].

The cross sections of the three airfoils, S818, S825, and S826 are shown in Figure 4.9 respectively.

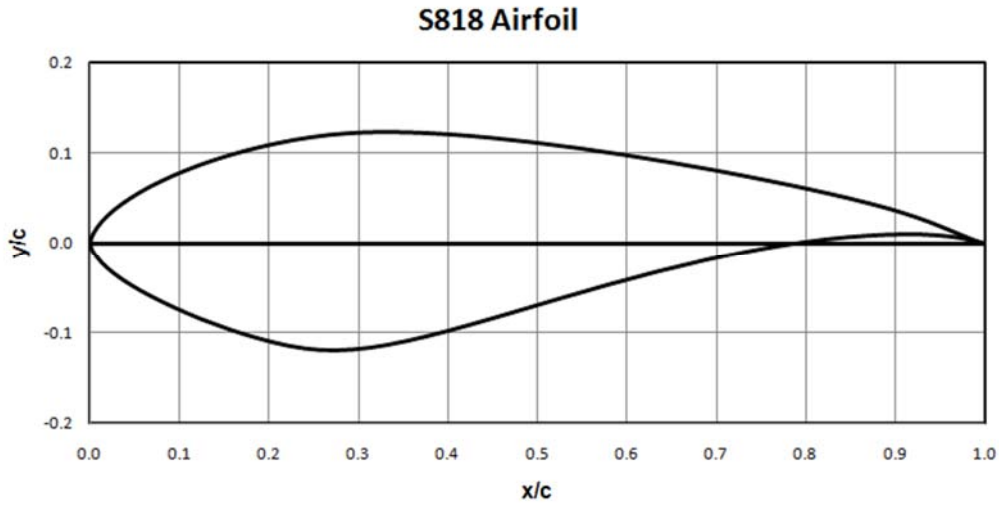

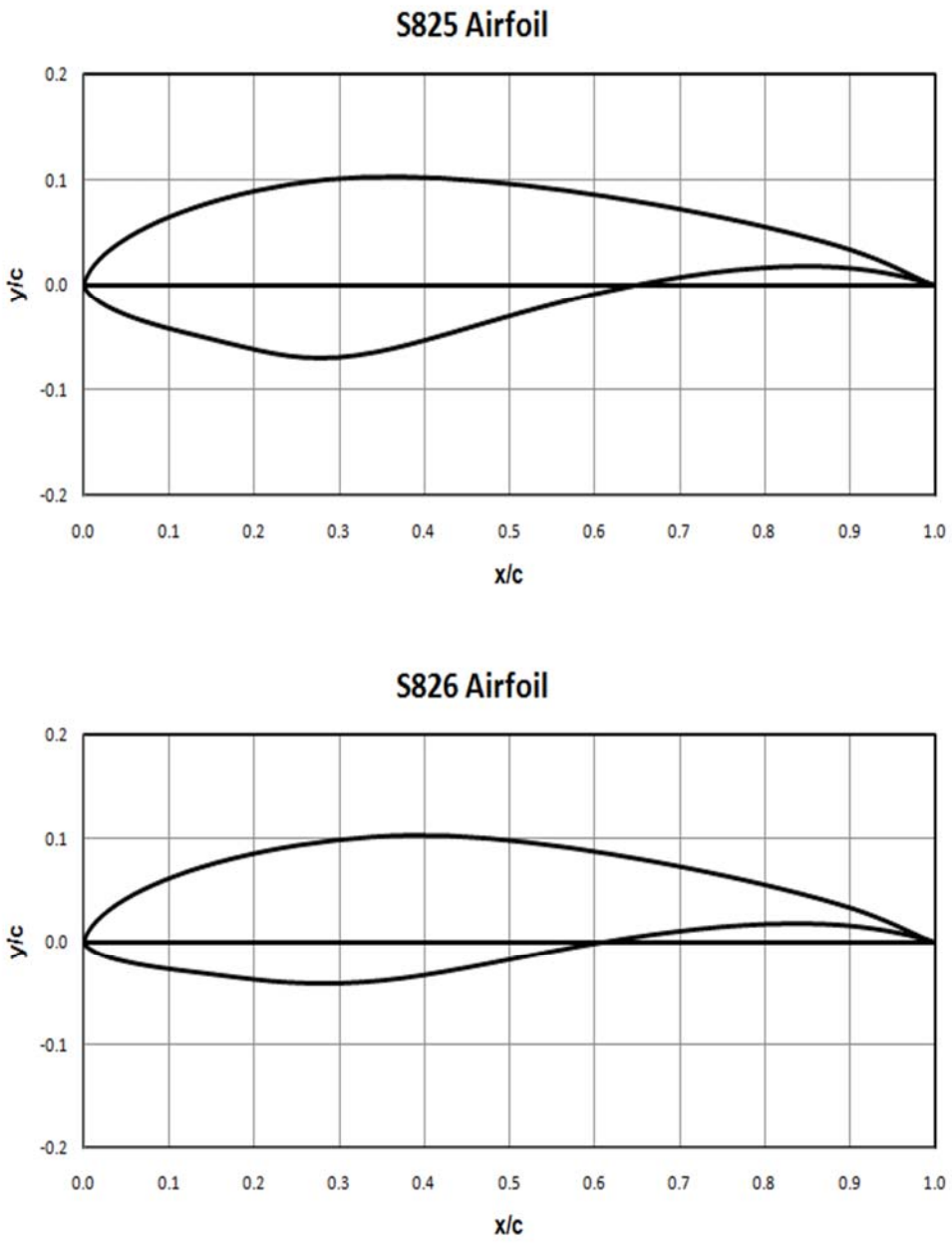

Figure 4.9: The sketches of the S818, S825, and S826 airfoil shapes[3].

[3] The figures are from the wind designing website: https://wind.nrel.gov/airfoils/Shapes

The domain configuration

The domain configuration of the fluid domain is shown in Figure 4.10.

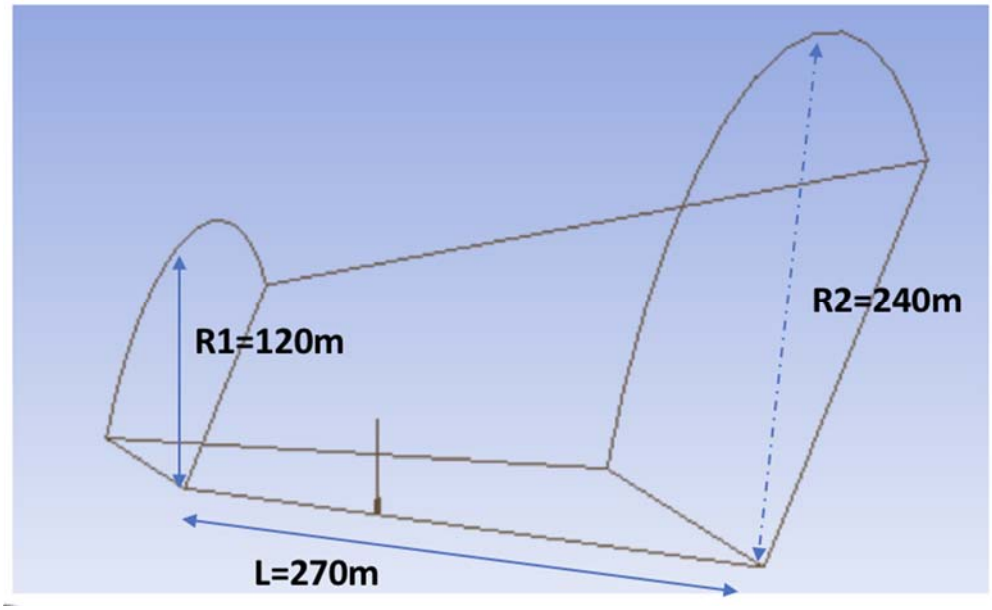

Figure 4.10: The configuration of the computational fluid domain.

The configuration of the computational domain is shown in Figure 4.10, as stated previously. The domain is designed as a truncated circular cone. The inlet circular is set with a radius of 120m, while the outlet 240m. These two surfaces are 270m away from each other horizontally, where the blade is put in the middle and set as the origin of this domain. The blade is set along the x-direction and the wind is coming in from the left circular surface in $(-\mathrm{z})$ direction.

CHAPTER 5

3D AERODYNAMICAL SIMULATION OF WIND TURBINE

Using the theories, geometries, and meshes illustrated in previous chapters, three different wind cases are considered and simulated in this chapter, characterized by the inflow wind speed of $5ms^{-1}$, $12ms^{-1}$, and $22ms^{-1}$ respectively. In this chapter, the aerodynamic properties of the horizontal wind turbine blade are discussed. To ensure the main features of the wind turbine systems are captured, we compare the wind blade performances under different boundary conditions. In the following, the results are presented in the rotating framework i.e. the flow in the domain rotates while the turbine remains stationary. For clarity, for some figures marked "Stn" in the caption, the results are shown in the stationary framework (correspond to the ground).

Case 1: When Inflow Wind Velocity Is $\mathbf{5ms^{-1}}$

In this case, the inflow wind velocity is set as $5ms^{-1}$ which is a required minimal value for withe nd turbine to operate. This velocity is close to the cut-in wind speed for most wind turbines. Using the numerical schemes discussed in the previous chapters, the results are shown in the following sections.

Residual plots

The residual errors of convergence are shown in Figure 5.1 after 1600 iterations have been conducted. The residual error comes from the discretization when the partial differential equations are approximated with a group of algebraic equations and every algebraic equation must be solved for an individual control volume. The residuals of the continuity, momentum equations and are generally considered as convergence criteria [ANSYS GUIDE, 15.6]. The residual errors are controlled to be below 1×10^{-4}.

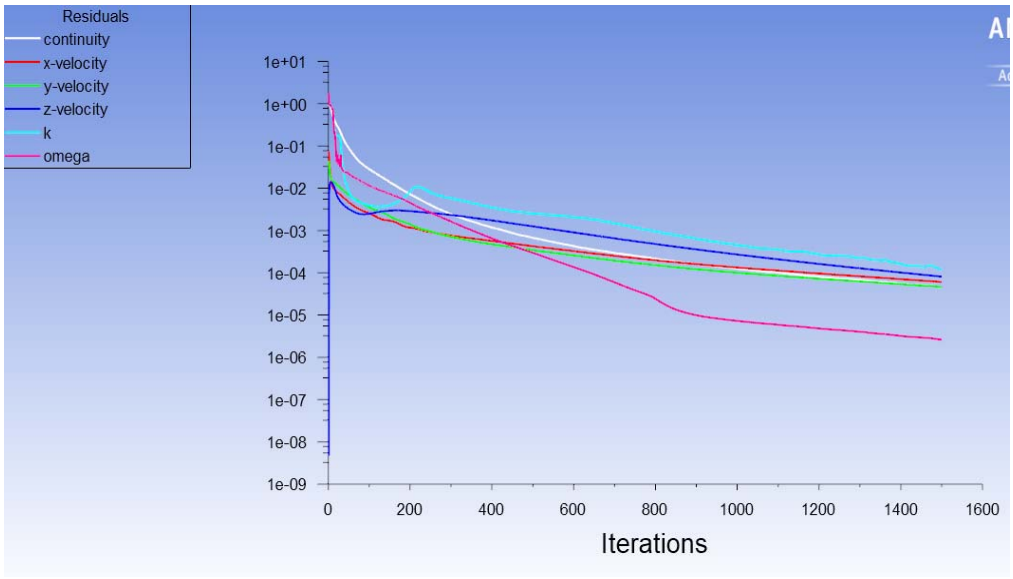

Figure 5.1: The variations of residual errors of the relevant parameters versus increasing interactions.

It is shown in Figure 5.1 that after running the simulation for 1500 steps, all of the residual errors become lower than 1×10^{-4}. The integral pressure of the entire

turbine blade (upper and lower) is used as a second monitor and the variation of it is shown in Figure 5.2.

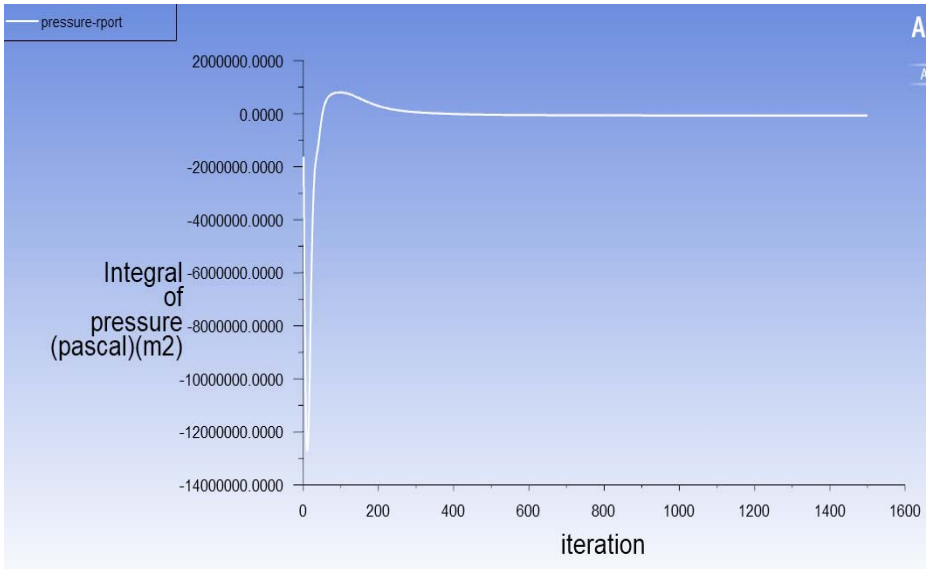

Figure 5.2: The variations of integral pressure of the blade per unit surface versus increasing iteration.

Figure 5.1 shows that as the number of iterations increases, the residual errors decrease. For fluid calculations, the mass flow rate within the domain is computed. The detail of these mass flow rates are given as inlet: 92175.4 kgs^{-1}, inlet top 277078.5kgs^{-1} and outlet $-369256.1kgs^{-1}$. It is approximated that a net $-2.1kgs^{-1}$ (=total outlet- total inlet) is lost between the inflow and the outflow. Therefore, the conservation of mass is satisfied.

Figure 5.2 indicates the variation of the integral blade pressure over the number of iterations. As the iteration increases, the calculation is converging thus the

integral blade pressure become stable at around the value of the free atmosphere pressure. It shows that after sufficient iterations the solution converges.

Turbine blade profiles

The rotational speed of the turbine is shown in Figure 5.3, where a series of colored arrows are used to represent the magnitude of the rotational speed.

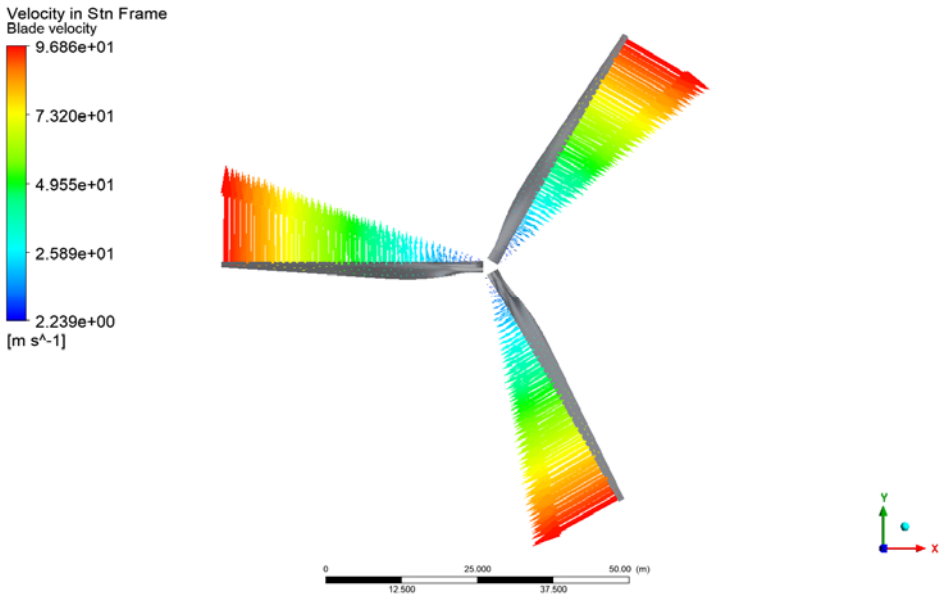

Figure 5.3: Blade velocity of the turbine blade in a stationary frame (refer to the non-rotational ground).

It is shown in Figure 5.3 that the velocity is not uniformly distributed in the blade surface: the rotational velocity is relatively larger near the tip region, while the velocity is smaller near the root. This is explained by our operating condition: the blade is set with a specific angular velocity, which is 2.22 $\mathrm{rad}s^{-1}$, the blade velocity

is larger as the reference point moves away from the root. The conditions are set to represent those of a typical 80 m wind turbine with a rotational speed of ~21 rpm and a tip speed velocity of over 80 m/s.

Velocity streamlines

The velocity of the fluid in a stationary frame is shown in Figure 5.4. The wind is coming from the inlet and the inlet top surfaces in all simulations, as shown in the left figure in Figure 5.4. To make the result more clear, the wind is long inserted from the inlet for surface only for illustration purpose in the right figure. It is clear from the right subfigure that the wind velocity decreases once it passes the turbine blades. The velocity is almost uniformly distributed in the horizontal direction, however, the velocity is decreasing in the vicinity of the turbine blade. This is because the energy transition is intense for the region near the blade. The kinetic energy is harvested by the wind turbine to generate electricity. Also when the wind approaches the blade surface, lift and drag forces are both generated here, therefore, kinetic energy is used to maintain the turbine rotation while only a small fraction of the kinetic energy from wind is lost through friction as heat.

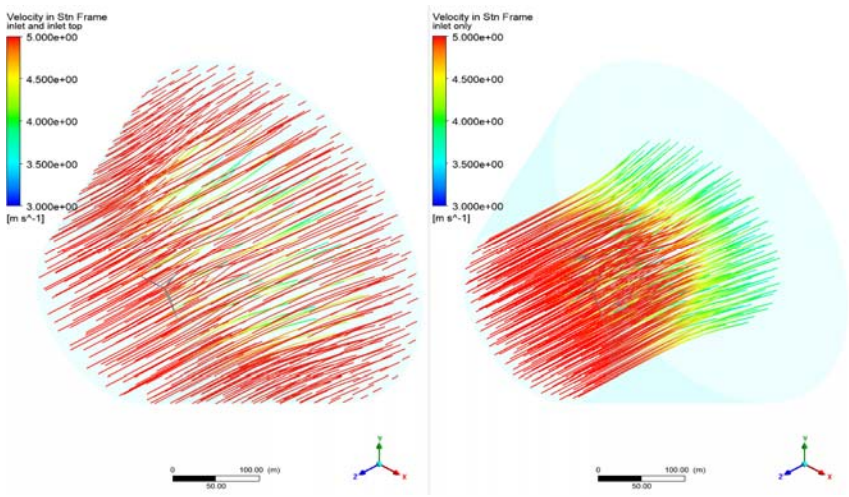

Figure 5.4: Velocity streamlines in the fluid domain. The velocity is plotted in a stationary domain (refer to the non-rotational ground).

Pressure contours

The pressure contour of the turbine blade front is shown in Figure 5.5. Note the inflow wind speed is set at $5 \mathrm{m} s^{-1}$.

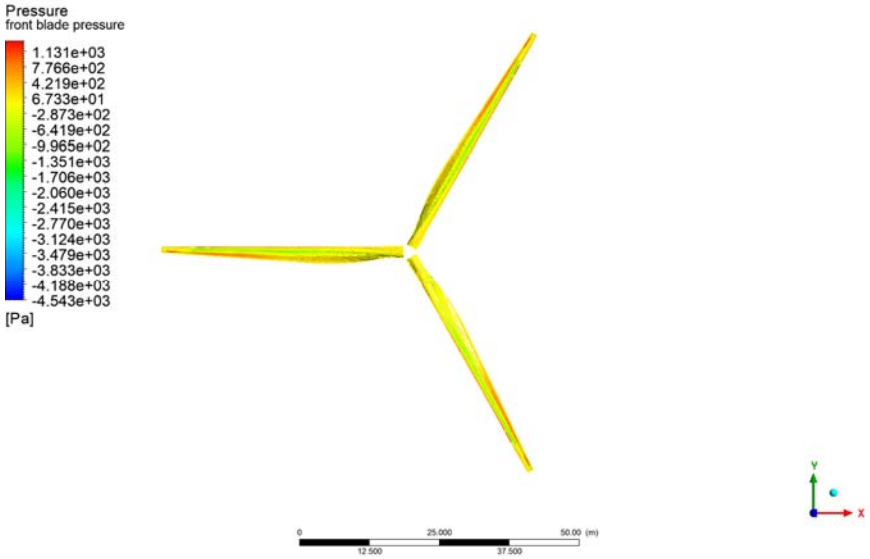

Figure 5.5: Pressure contour on the wind turbine blade front.

It is shown that the pressure is relatively high near the tip compared with the near-root region. It also shows that the pressure is larger near the edges, however, the pressure is smaller along the trailing edge near the rotor.

The pressure contour on the back of the wind turbine blade is shown in Figure 5.6. It shows that the pressure is relatively higher in front of the rotor plane but lower immediately after.

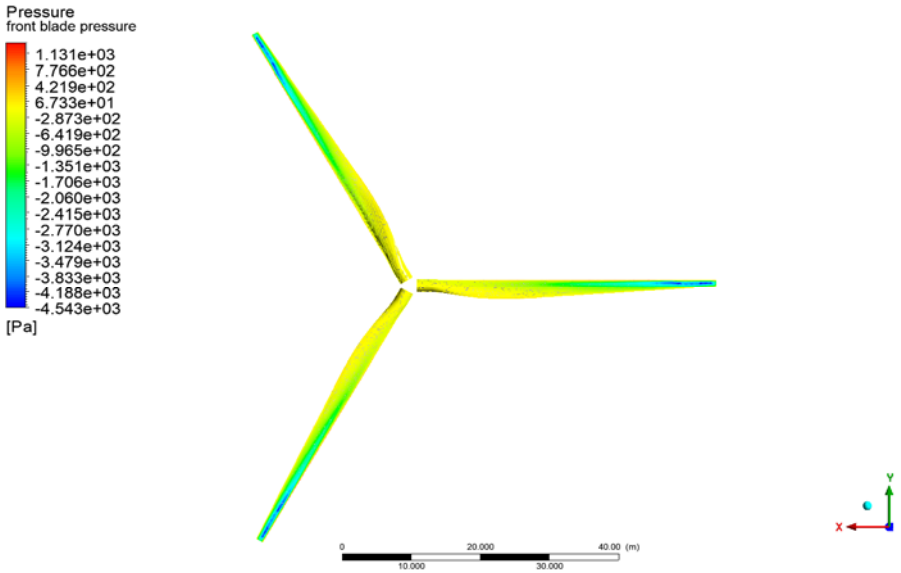

Figure 5.6: Pressure contour on the wind turbine blade back.

It is shown in Figure 5.5 and 5.6 that the pressure contours are closely related to the wind conditions. The pressure on the turbine tip is relatively larger than that near the rotor. This can be explained by the fact that the velocity due to rotation near the tip is larger than that in the root region, given that the entire turbine blade is spinning in a fixed angular velocity. Since the tip velocity is larger, the dynamic pressure due to motions is larger, the pressure near the tip is thus larger. Second, we

found that the pressure on the back of the blade is smaller than that in the front. This is consistent with our understanding since the wind velocity is larger in the front. Due to the extraction of energy by the turbine blade, the wind velocity is strongly influenced by the turbine blade, thus a large amount of kinetic energy is removed by the wind turbine and some is lost as heat.

Pressure contour for different cross section

Cross-sections on three representative locations, the near root region (at x=-10m), the near-tip region (at x=-43m), and the region between the tip and the root (blade mid-point, at x=-35m) are shown in Figures 5.7-5.9.

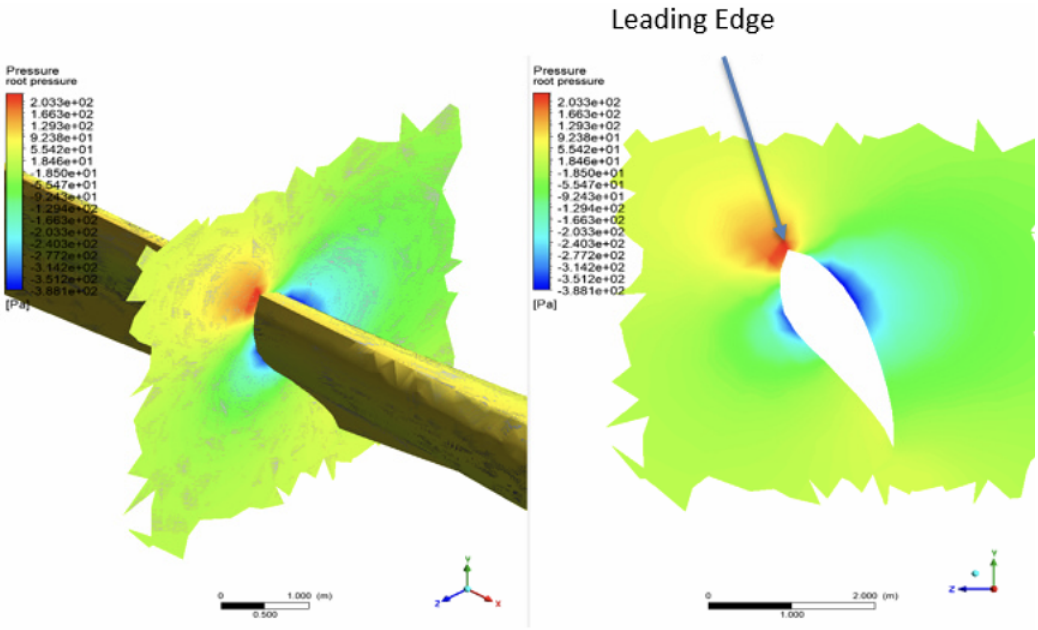

Figure 5.7: Pressure contour for the wind fluid near the root region. The left is a 3D sketch of the YZ plane and the pressure on the blade and the ambient fluid. The right subfigure shows a 2D pressure contour on the selected YZ plane (x=-10m). It is noted

that the blade section has an S818 airfoil shape. The leading edge is at the top of the frame and the trailing edge at the bottom.

For the near root region, it is shown in Figure 5.7 that the pressure is higher in the leading edge side compared with the trailing edge. The pressure contour can be explained by the fact that the leading edge is the active side which interacts with the wind. The low-pressure region creates lift. It is shown that the leading edge has a positive pressure gradient.

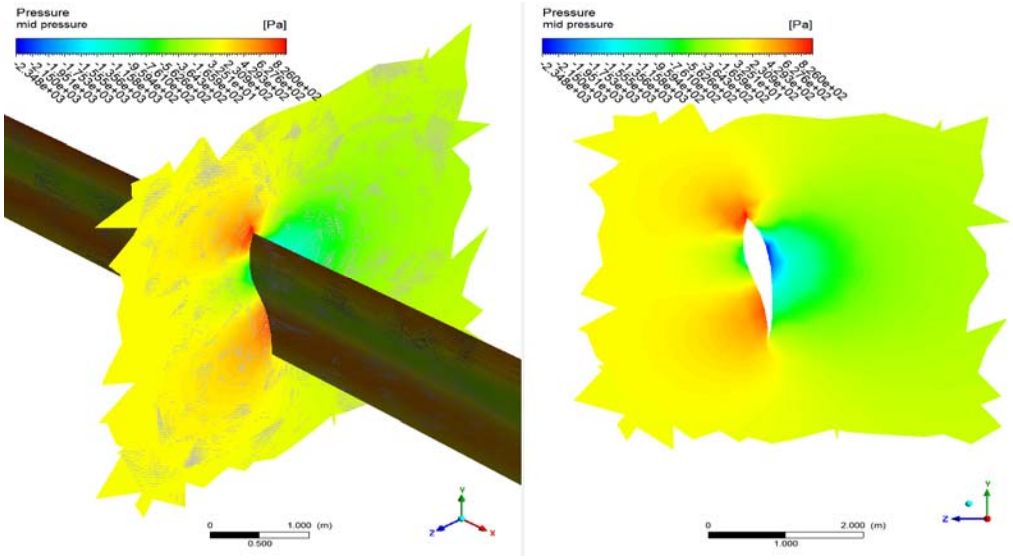

Figure 5.8: Pressure contour for the wind fluid near the mid region. The left is a 3D sketch of the YZ plane and the pressure on the blade and the ambient fluid. The right subfigure shows a 2D pressure contour on the selected YZ plane (x=-30m). It is noted that the blade section has an S825 airfoil shape.

For the mid-blade region, it is shown in Figure 5.8 that the pressure in the mid-region of the blade is larger than that compared with the root region. This is not

surprising as the rotating speed is larger in the mid-region compared with that in the root zone. It is also noted that the pressure is high at the trailing and leading edge, while the low-pressure region generates lift.

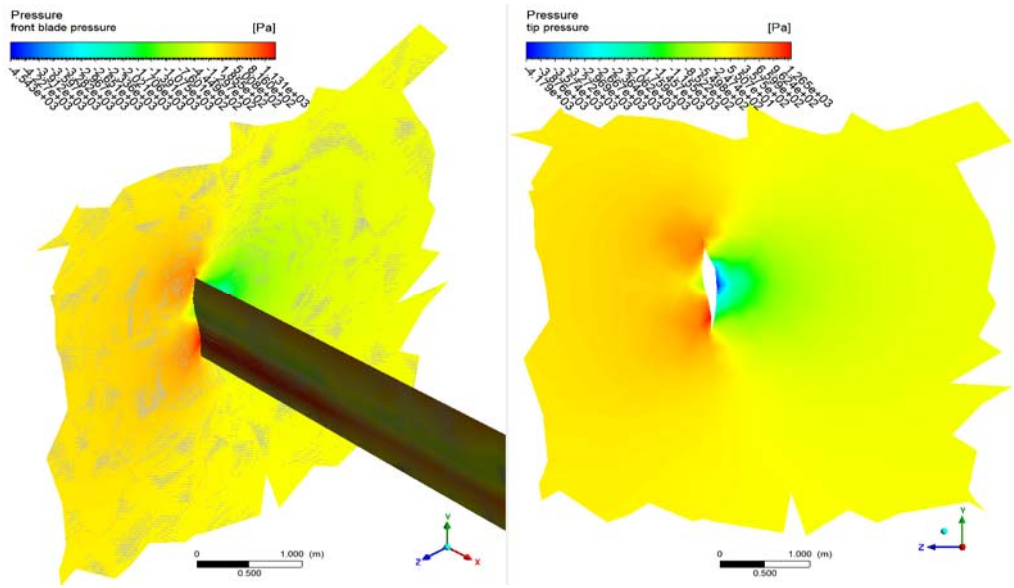

Figure 5.9: Pressure contour for the wind fluid near the tip region. The left is a 3D sketch of the YZ plane and the pressure on the blade and the ambient fluid. The right subfigure shows a 2D pressure contour on the selected YZ plane (x=-43m). It is noted that the blade section has an S826 airfoil shape.

For the near-tip region, it is shown in Figure 5.9 that the pressure increases in both the leading edge and the trailing edge. The pressure contour can be explained by the fact that the relative velocities are larger than at other places on the blade. Figures 5.7 to 5.9 show that there is a positive pressure gradient at the leading edge region. The velocity streamlines are also shown in the following figures.

Velocity streamlines for different cross sections

The streamlines of the wind in the vicinity of the blade are presented for the same locations in Figures 5.10-5.12.

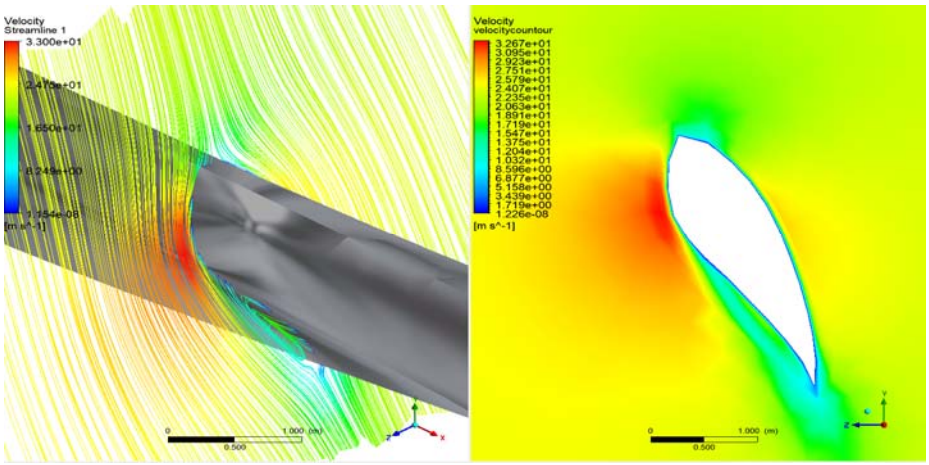

Figure 5.10: Fluid streamlines for the wind fluid near the root region. The left is a 3D sketch of the YZ plane and the fluid streamlines for ambient fluid around the blade. The right figure shows a 2D pressure contour on the selected YZ plane (x=-10m). It is noted that the blade section has an S818 airfoil shape.

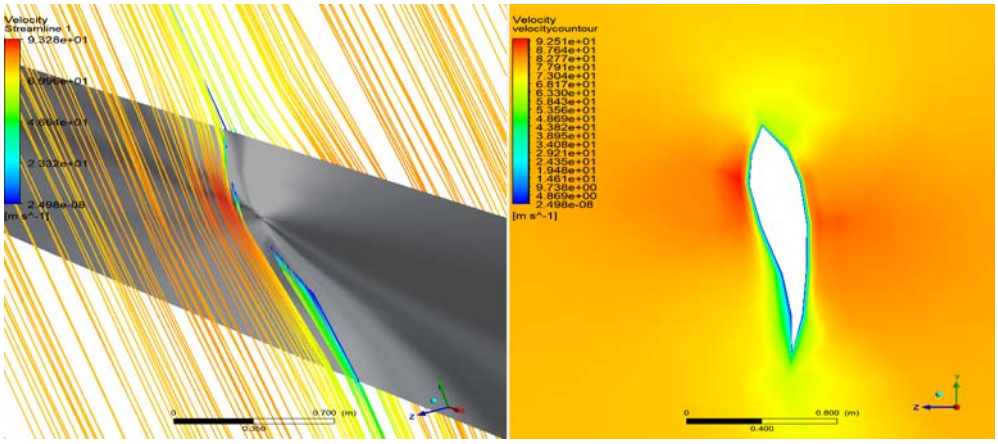

Figure 5.11: Fluid streamlines for the wind fluid near the mid blade region. The left is a 3D sketch of the YZ plane and the fluid streamlines for ambient fluid around the blade.

The right subfigure shows a 2D pressure contour on the selected YZ plane (x=-35m). It is noted that the blade section has an S825 airfoil shape.

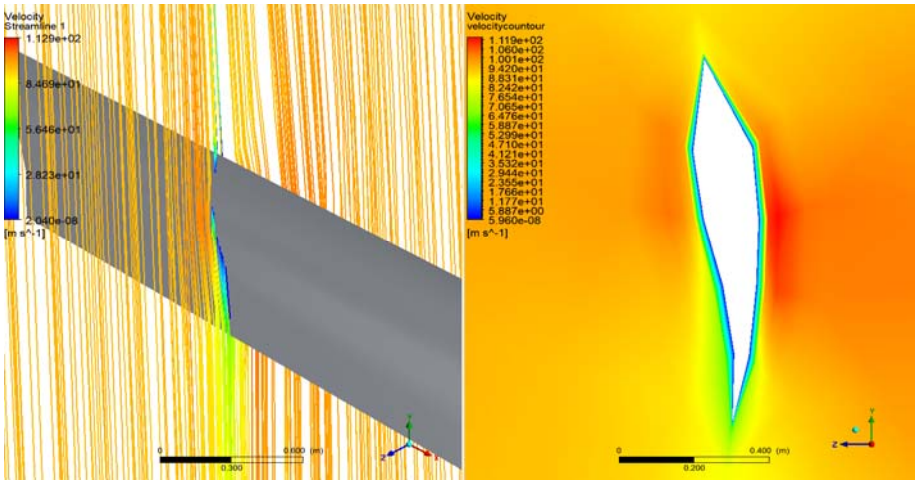

Figure 5.12: Fluid streamlines for the wind fluid near the root region. The left is a 3D sketch of the YZ plane and the fluid streamlines for ambient fluid around the blade. The right subfigure shows a 2D pressure contour on the selected YZ plane (x=-43m). It is noted that the blade section has an S826 airfoil shape.

Consistent with the pressure fields, Figures 5.11 and 5.12 show that the velocity in the mid-region of the blade is larger than those in the root region.

Figures 5.10 to 5.12 show that the velocities are relatively larger in the leading edge region compared with that in the trailing edge. The velocity is highest in the tip region, among the root, mid and the tip regions. This may help explain why the leading edge erosion is most intensive near the tip zone or the outer ⅓ of the blade.

Case 2: When Inflow Wind Velocity Is $12ms^{-1}$

In this section, the wind velocity used for simulation is $12ms^{-1}$, which is a normal wind turbine operating velocity. At this wind speed, the turbine is typically operating at its rated wind speed. The simulation follows the same operating conditions as Case One, except for the different boundary conditions. The residual errors, the pressure monitor, the pressure contour and velocity streamlines are shown in the following subsections.

Residual plots

Figure 5.13 shows the residual error of the simulation errors versus increasing iteration steps. After running the simulation for 1500 steps, the residual errors become lower than 1×10^{-4}.

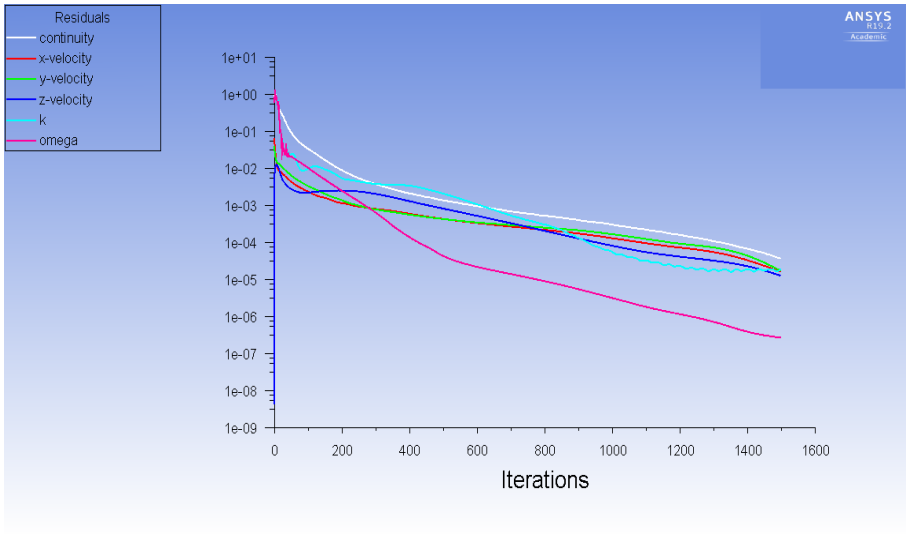

Figure 5.13: The variations of residual errors versus the number of iterations.

It is shown in Figure 5.13 that the residual error decreases over the number of iteration. After 1500 iterations, the residual error becomes reasonably low. The solution converges, therefore the simulation ends. For the fluid calculation, the mass flow rate is also computed and a net $-0.4kgs^{-1}$ (about 5.0×10^{-7} of the total mass flow rate) is lost. Therefore, the conservation of mass is satisfied. The detail of these mass flow rate is given as: inlet $221221.14kgs^{-1}$, inlet top $664988.48kgs^{-1}$ and outlet $-886210.06kgs^{-1}$.

The integral pressure on the turbine blade is shown in Figure 5.14.

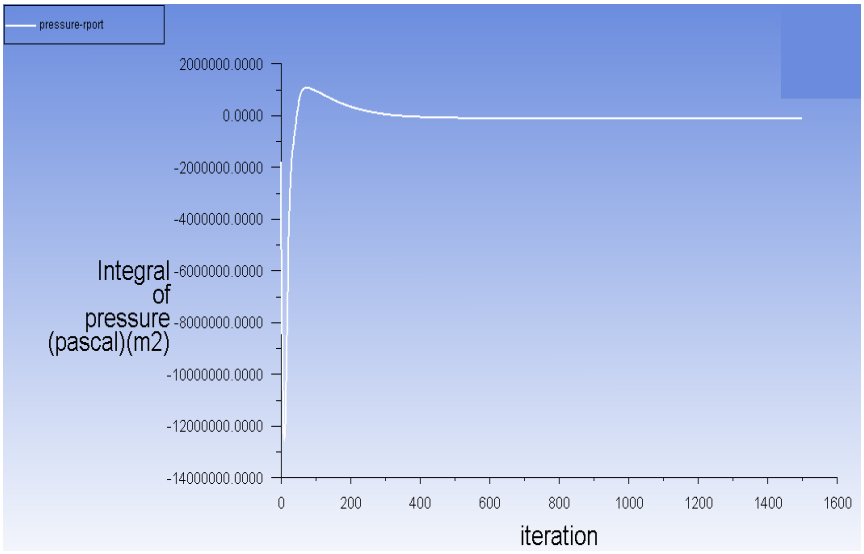

Figure 5.14: The variations of integral pressure on blade versus increasing interactions

Figure 5.15 shows the variation of the integral blade pressure versus different iterations. The rotating speed of the turbine is shown in Figure 5.15.

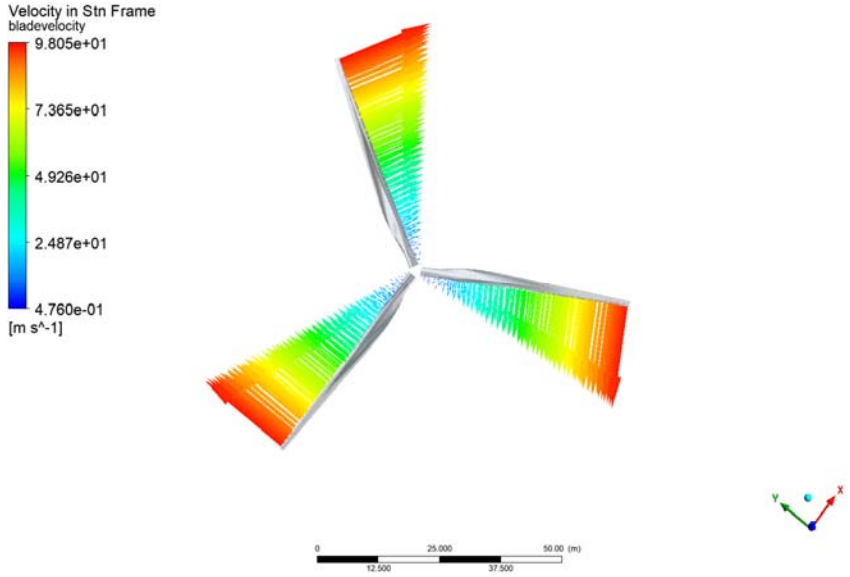

Figure 5.15: Blade velocity of the turbine blade in a stationary frame.

It is shown in Figure 5.15 that the velocity is not uniformly distributed in the blade surface: the velocity is relatively larger in the tip region, while the velocity is smaller near the rotor. This is similar to the finding in the case when the wind velocity is $5ms^{-1}$.

Velocity streamlines

Similarly, the velocity streamlines of the fluid in a stationary frame are shown in the following Figure 5.16.

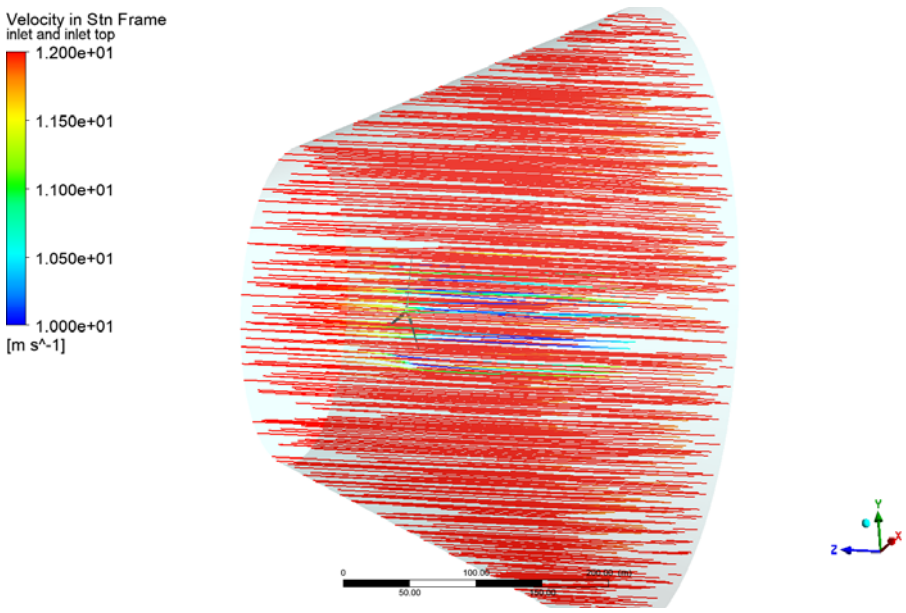

Figure 5.16: Wind velocity in the fluid domain. The velocity is plotted in a stationary reference.

Again, it is shown in Figure 5.16 that the velocity is almost uniformly distributed in the horizontal direction, however, the velocity is decreasing near the turbine blade. However compared with the streamlines in case one, the velocity becomes higher, since the inflow wind velocity is larger.

Pressure contour

The pressure contour of the turbine blade front is shown in Figure 5.17.

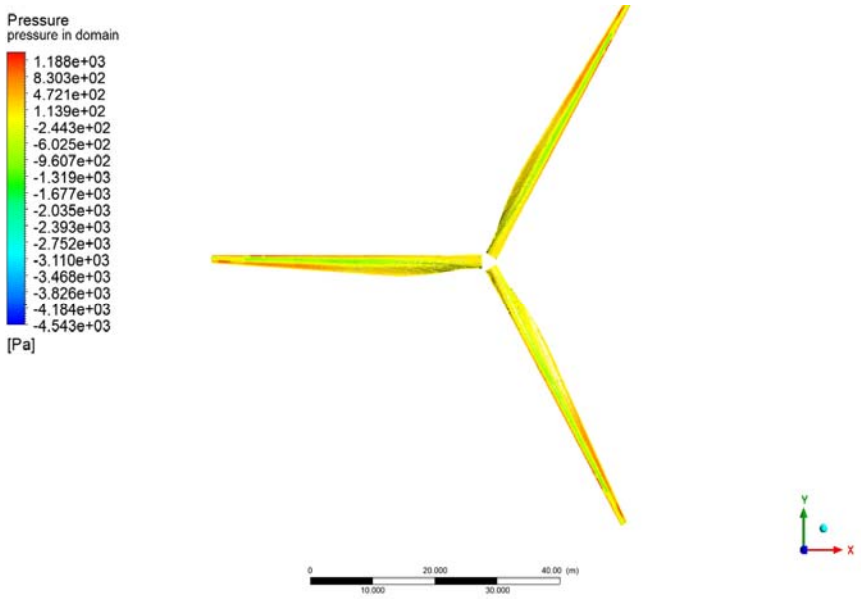

Figure 5.17: Pressure contour on the wind turbine blade front. It is shown in this figure that the pressure is relatively higher near the tip compared with the rotor region.

The pressure contour on the back of the blade is shown in Figure 5.18.

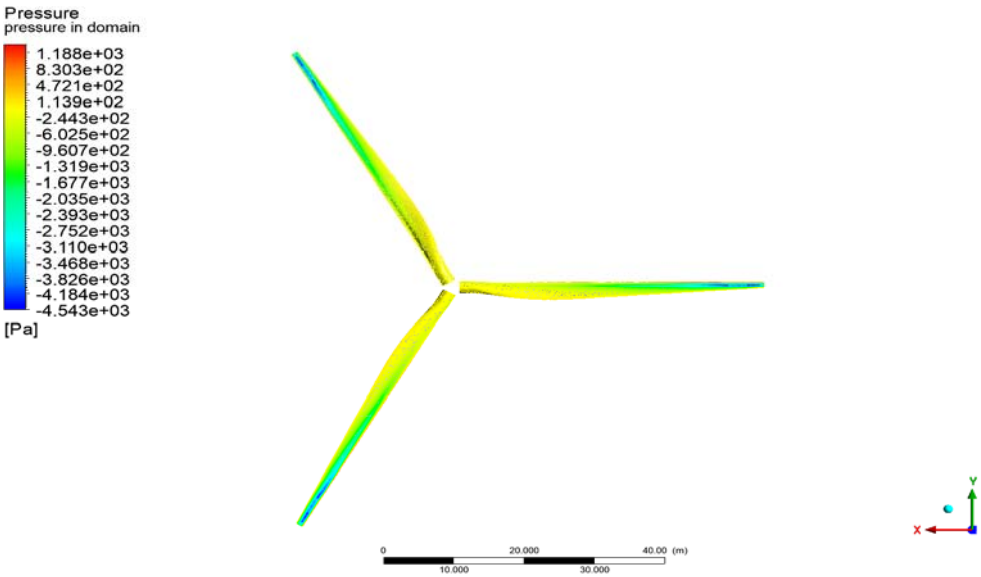

Figure 5.18: Pressure contour on the wind turbine blade back. It is shown in that the pressure is relatively higher in the front but lower in the back.

It is shown in Figures 5.17 and 5.18 that the pressure contours are closely related to the wind conditions. The pressure on the turbine tip is relatively larger than that near the root. This agrees with the observations in case one, however, the pressure becomes higher in case two. The increased pressure can be explained by the higher wind velocity, which indicates a larger dynamic pressure.

Pressure contour for different cross sections

The pressure contours on the three representative cross sections are also plotted for comparison in this subsection. First, the pressure contour for the cross section near the root region (at x=-10m) is shown in the following Figure 5.19.

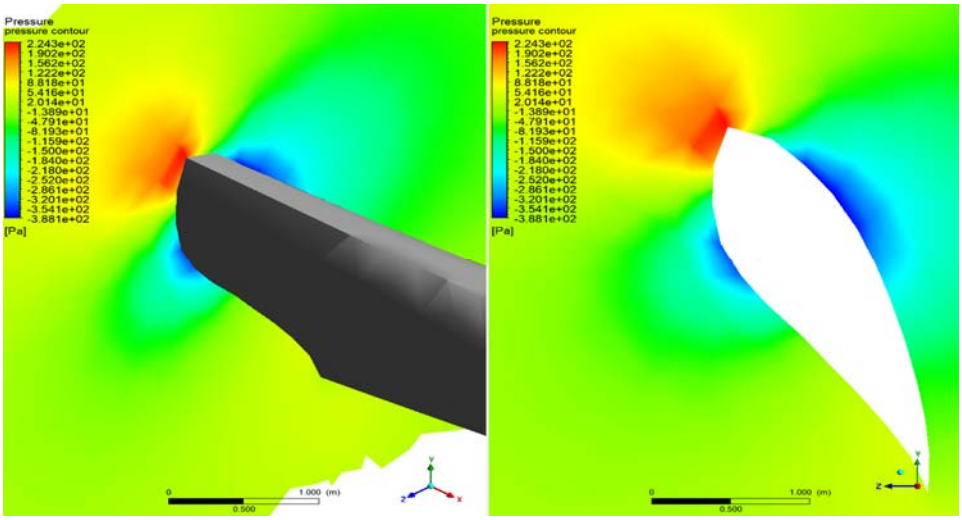

Figure 5.19: Pressure contour for the wind fluid near the root region. The left is a 3D sketch of the YZ plane and the pressure on the blade and the ambient fluid. The right subfigure shows a 2D pressure contour on the selected YZ plane (x=-10m). It is noted that the blade section has an S818 airfoil shape.

It is shown in Figure 5.19 that the pressure is higher in the leading edge side compared with the trailing edge. Compared with case 1, the pressure increases largely. This indicates the free wind velocity has a strong impact on the blade.

Second, the pressure contour for the cross section near in the mid (at x=-35m) is shown in Figure 5.20.

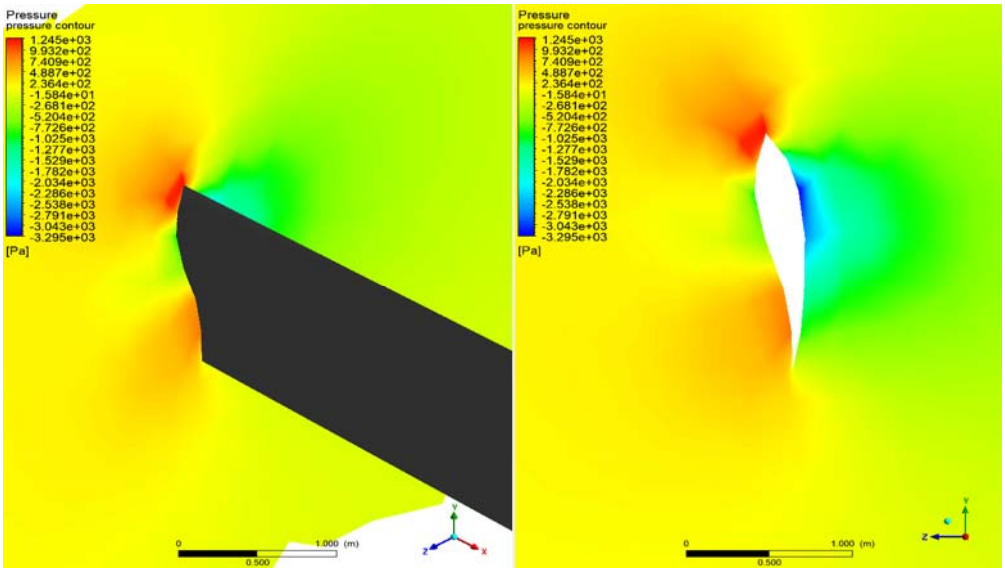

Figure 5.20: Pressure contour for the wind fluid near the mid region. The left is a 3D sketch of the YZ plane and the pressure on the blade and the ambient fluid. The right subfigure shows a 2D pressure contour on the selected YZ plane (x=-30m). It is noted that the blade section has an S825 airfoil shape.

It is shown in Figure 5.20 that the pressure in the mid-region of the blade is larger than that compared with the root region. The pressure also increases compared with the mid-region in Case one.

Finally, the pressure contour for the cross section near the tip (at x=-43m) is shown in Figure 5.21.

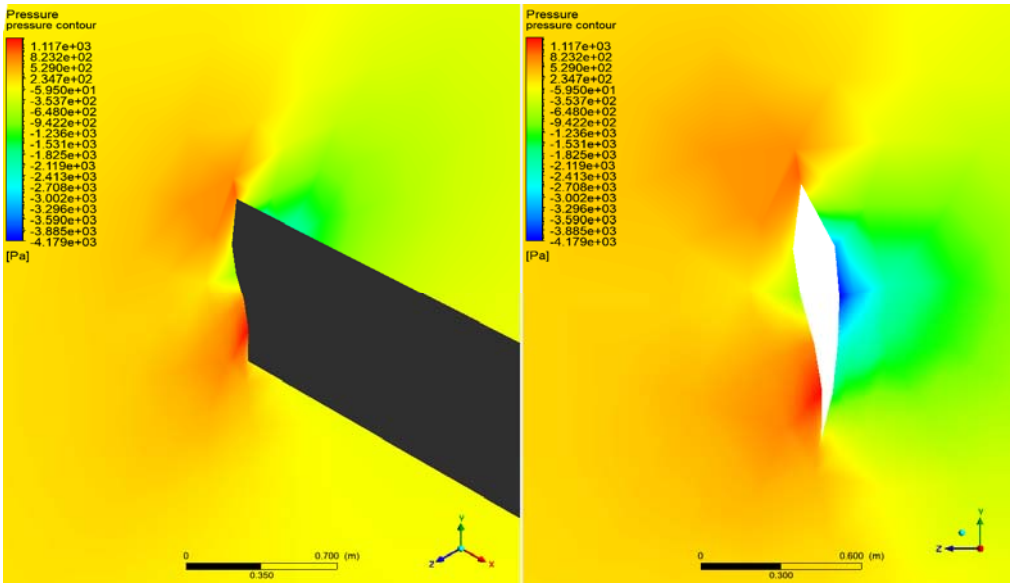

Figure 5.21: Pressure contour for the wind fluid near the tip region. The left is a 3D sketch of the YZ plane and the pressure on the blade and the ambient fluid. The right subfigure shows a 2D pressure contour on the selected YZ plane (x=-43m). It is noted that the blade section has an S826 airfoil shape.

It is shown in Figure 5.21 that the pressures are very high near both the leading-edge and the trailing edge, as expected. The pressure contours are similar to Case one when the surface wind velocity is $5ms^{-1}$. However, it is noted that the velocity is much larger in Case two. Figures 5.18 to 5.21 show that the pressure are relatively larger in the leading edge region compared with that in the trailing edge. The pressure is higher in the front of the blade in contrasted with the back of the blade. The pressure reaches the higher in the tip region, among the root, mid and the tip regions.

Velocity streamlines for different cross sections

First, the fluid streamlines for the cross section near the root region (at x=-10m) is shown in the following Figure 5.22.

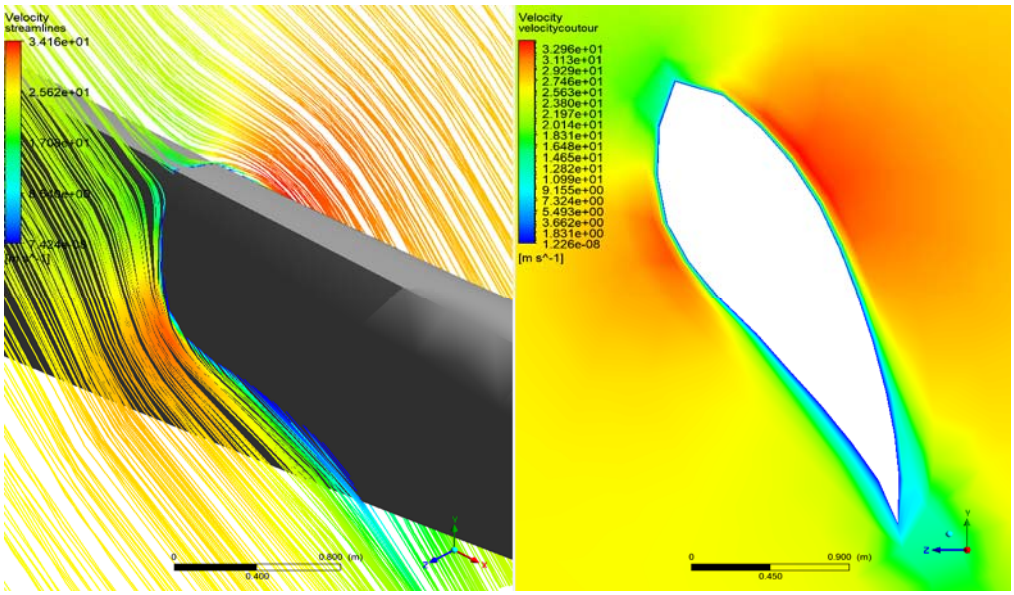

Figure 5.22: Fluid streamlines for the wind fluid near the root region. The left is a 3D sketch of the YZ plane and the fluid streamlines for ambient fluid around the blade. The right subfigure shows a 2D pressure contour on the selected YZ plane (x=-10m). It is noted that the blade section has an S818 airfoil shape.

It is shown in Figure 5.22 that the velocity is larger in the leading edge side compared with the trailing edge. The velocity near the blade is higher than that in Case one, which is expected since the surface wind speed increases from $5ms^{-1}$ to $12ms^{-1}$.

The fluid streamlines for the cross section near in the mid (at x=-35m) is shown the following Figure 5.23.

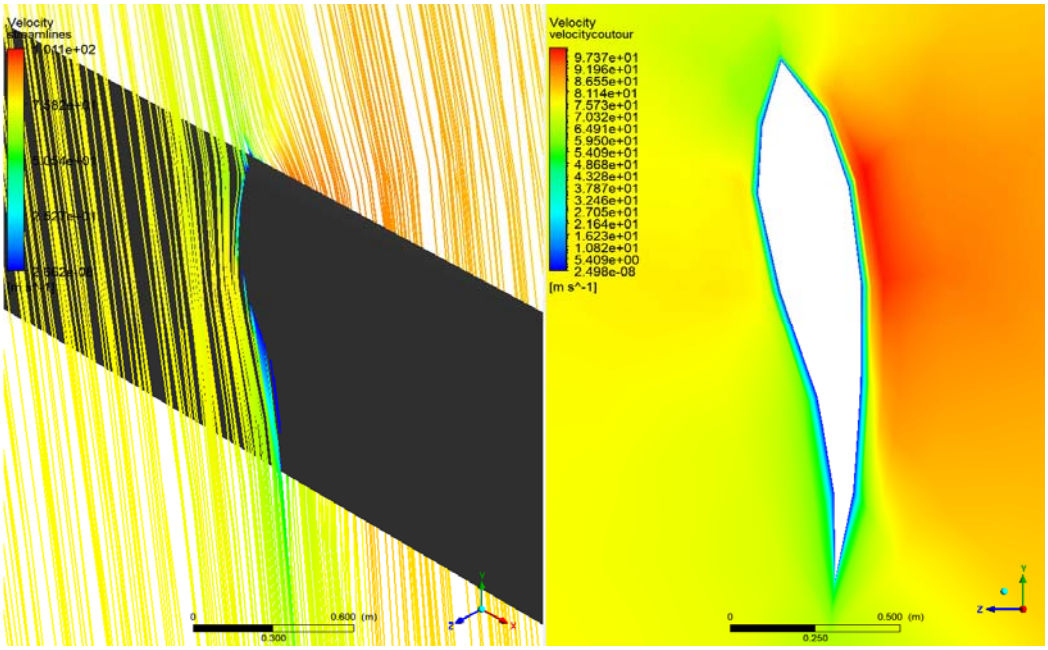

Figure 5.23: Fluid streamlines for the wind fluid near the mid blade region. The left is a 3D sketch of the YZ plane and the fluid streamlines for ambient fluid around the blade. The right subfigure shows a 2D pressure contour on the selected YZ plane (x=-35m). It is noted that the blade section has an S825 airfoil shape.

In addition, fluid streamlines for the cross section near in the mid (at x=-43m) is shown the following Figure 5.24.

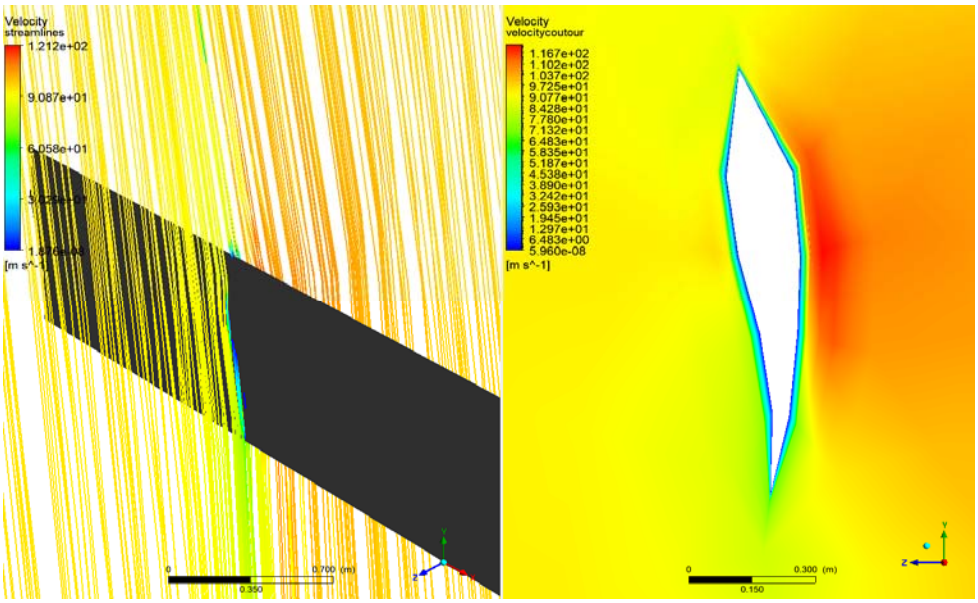

Figure 5.24: Fluid streamlines for the wind fluid near the root region. The left is a 3D sketch of the YZ plane and the fluid streamlines for ambient fluid around the blade. The right subfigure shows a 2D pressure contour on the selected YZ plane (x=-43m). It is noted that the blade section has an S826 airfoil shape.

Figures 5.22 to 5.24 show that the velocities are relatively larger in the leading edge region compared with that in the trailing edge. The velocity reaches the higher in the tip region, among the root, mid and the tip regions. When the surface wind speed increase, the ambient wind velocity near the blade also increases, however, the increment is less than the surface wind incensement, which is $7ms^{-1}$ ($12ms^{-1}$-$5ms^{-1}$). This implies that the blade velocity has more influences on the wind velocity near the blade.

Case 3: When Inflow Wind Velocity Is $22ms^{-1}$

Finally, we also investigate a high-velocity case when the surface wind velocity becomes far larger than the normal operation velocity. In this case, I set it $12ms^{-1}$ for the inflow wind velocity, which is used to contrast with Cases one and two. The simulation methods are the same as the simulations for the aforementioned Cases one and two, however, a different surface wind condition is employed in this case.

Residual plots

The residual plot is shown in Figure 5.25. The total iteration step is also set to 1500. The integral pressure monitor is also used in this case.

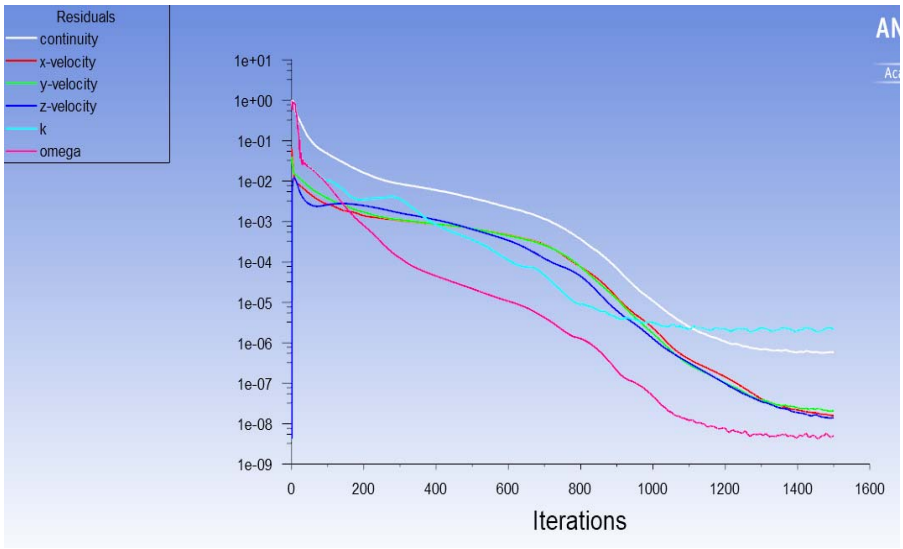

Figure 5.25: The variations of residual errors versus increasing interactions.

The integral pressure on the turbine blade is shown in Figure 5.26.

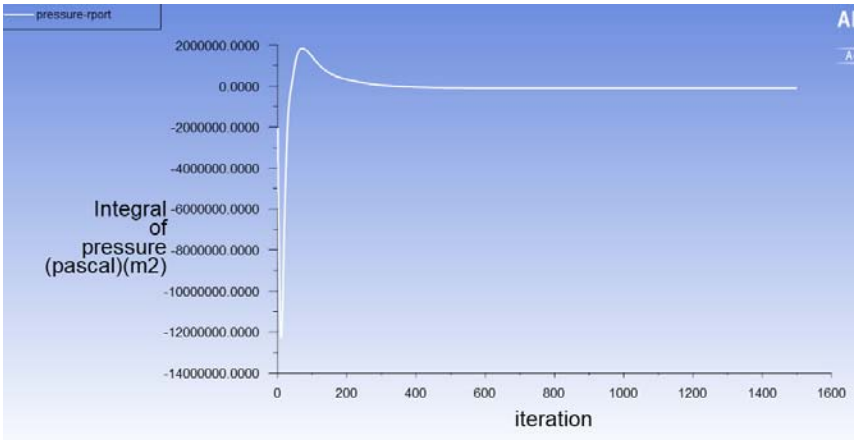

Figure 5.26: The variations of integral pressure on blade versus increasing interactions

Figure 5.26 shows that the residual errors become lower than 1×10^{-5} after 1500 iterations. The integral pressure monitor is shown in Figure 5.26. It is shown that when about 800 iterations are conducted, the ambient pressure is achieved.

Furthermore, the rotating speed of the turbine is shown in Figure 5.27.

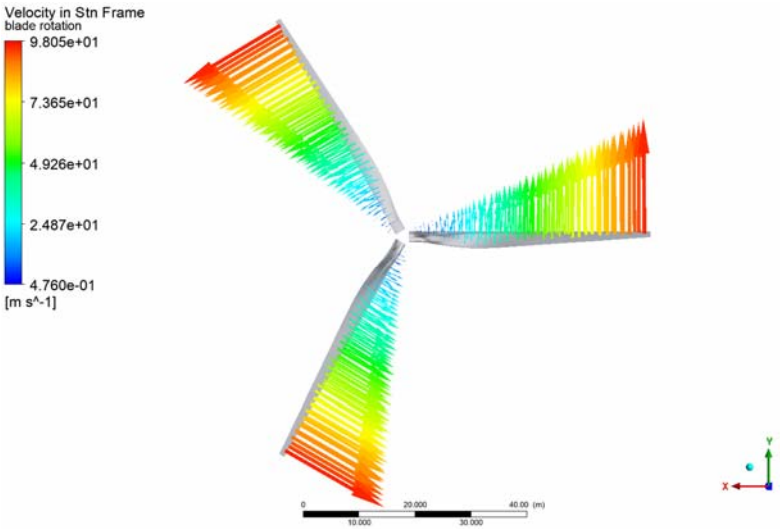

Figure 5.27: Rotating velocity of the turbine blade in a stationary frame.

It is shown in Figure 5.27 that the velocity is not uniformly distributed in the blade surface: the velocity is relatively larger in the tip region, while the velocity is smaller near the rotor. The wind velocity is the same as Cases One and Two since the angular velocity is set at the same 2.22rad/s.

Velocity Streamlines

The velocity of the fluid in a stationary frame is shown in the following Figure 5.28. It is noted that the streamlines are shown in the colorful lines.

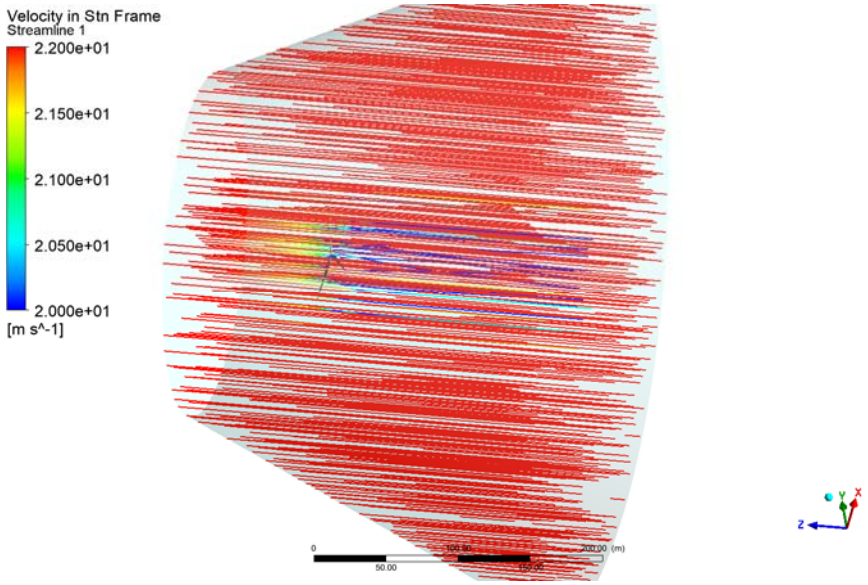

Figure 5.28: Wind velocity in the fluid domain. The velocity is plotted in a stationary domain.

It is shown in Figure 5.28 that the velocity is almost uniformly distributed in the horizontal direction, however, the velocity is decreasing near the turbine blade.

This is identical to Cases One and Two, however, the wind speed in Case Three reaches the largest, therefore, the velocity also increases in the domain.

Pressure contour

The pressure contours of the turbine blade front and back are shown in the following Figures 5.29 and 5.30.

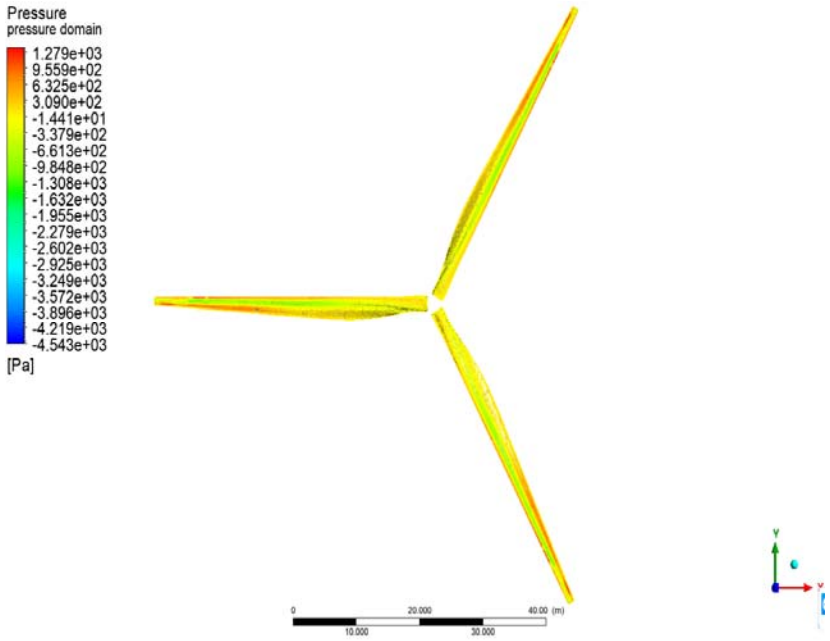

Figure 5.29: Pressure contour on the wind turbine blade front. It is shown that the pressure is relatively higher near the tip compared with the root region.

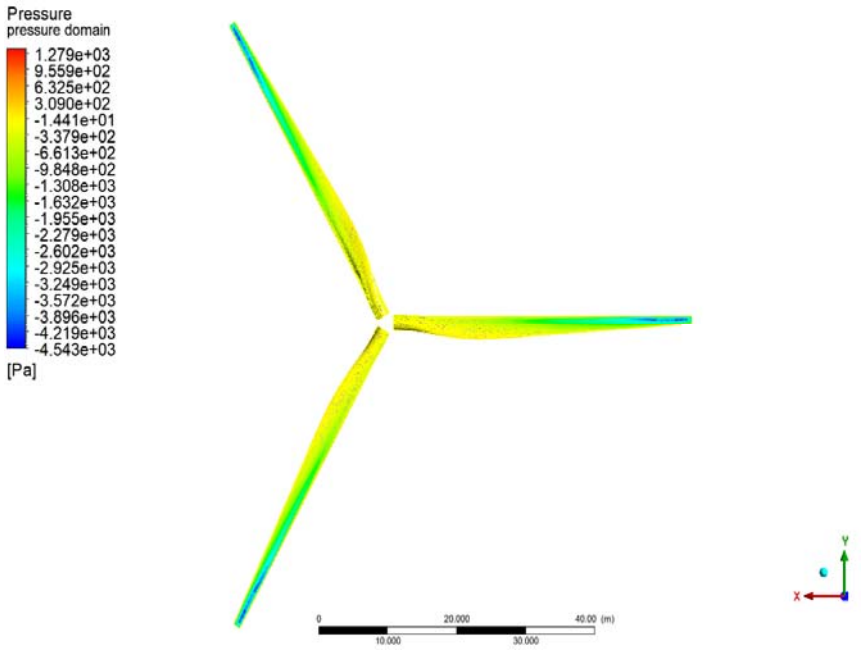

Figure 5.30: Pressure contour on the wind turbine blade back. It is shown in that the pressure is relatively higher in the front but lowers in the back.

It is shown in Figures 5.29 and 5.30 that the pressure contours are closely related to the wind conditions. Similar pressure bands have been observed in Case One and Two, therefore, it is not repeated here. A relatively high pressure, however, is noticed for Case three, which can be explained due to the larger wind speed.

Pressure contour for different cross sections

The pressure contours for different cross-sections are also investigated in this section. The pressure contour for the cross section near the root region (at x=-10m) is shown in the following Figure 5.31.

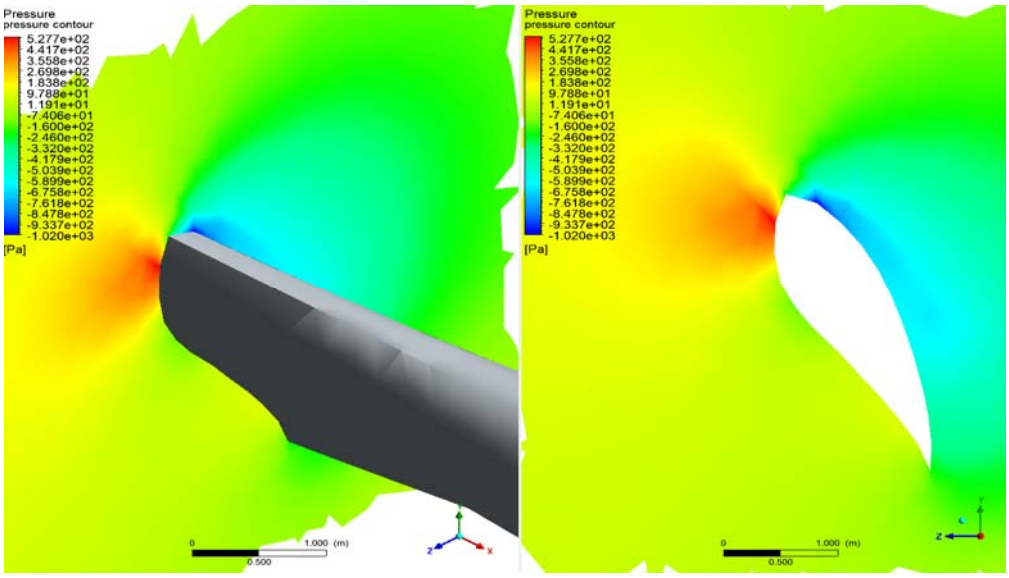

Figure 5.31: Pressure contour for the wind fluid near the root region. The left is a 3D sketch of the YZ plane and the pressure on the blade and the ambient fluid. The right subfigure shows a 2D pressure contour on the selected YZ plane (x=-10m). It is noted that the blade section has an S818 airfoil shape.

It is shown in Figure 5.31 that the pressure is higher at the leading edge compared with that in the trailing edge. This is the same as the observations in Case One and Two. Since the surface wind velocity increases, the relative velocity thus increases. Similarly, the pressure contour for the cross section near in the mid (at x=-35m) is shown in Figure 5.32. The pressure contour for the cross section near the tip (at x=-43m) is in Figure 5.33.

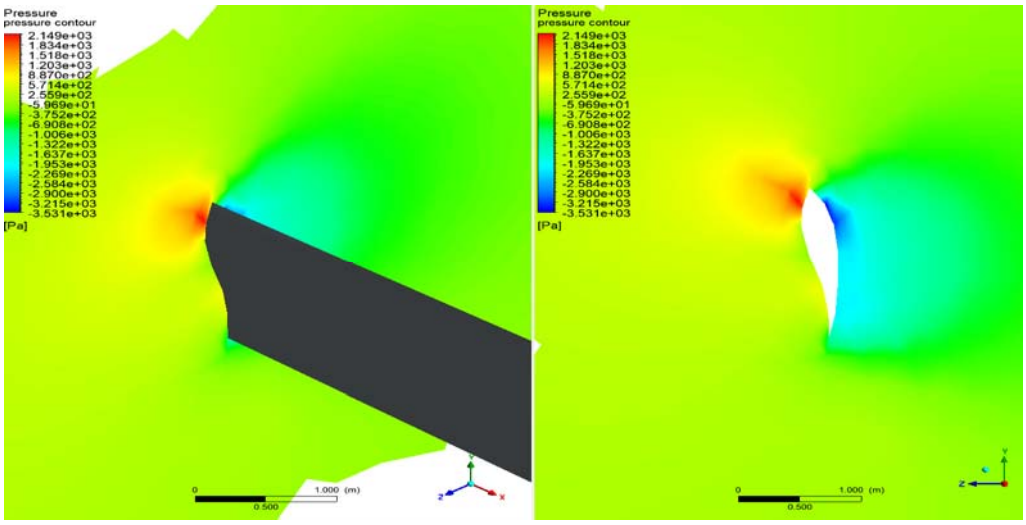

Figure 5.32: Pressure contour for the wind fluid near the mid region. The left is a 3D sketch of the YZ plane and the pressure on the blade and the ambient fluid. The right subfigure shows a 2D pressure contour on the selected YZ plane (x=-30m). It is noted that the blade section has an S825 airfoil shape.

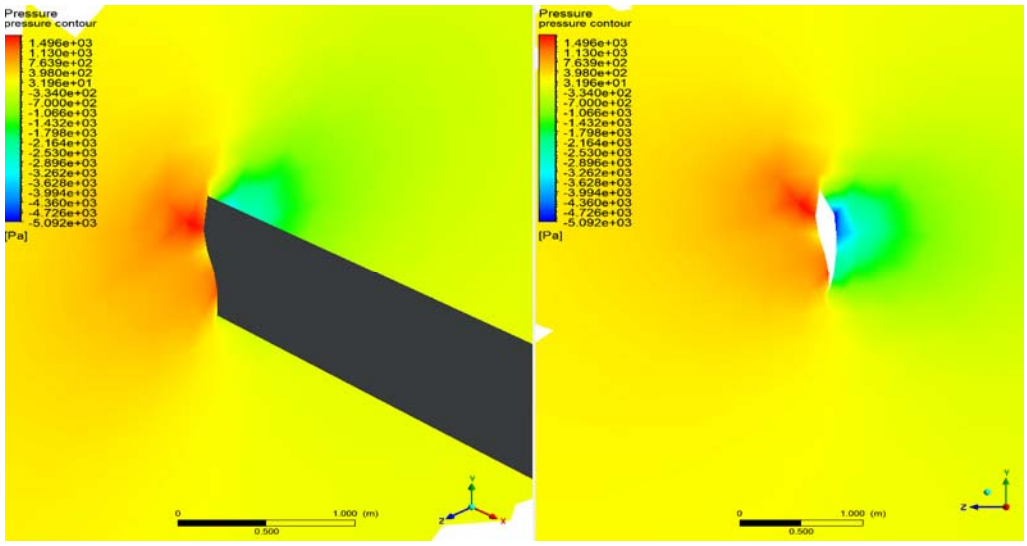

Figure 5.33: Pressure contour for the wind fluid near the tip region. The left is a 3D sketch of the YZ plane and the pressure on the blade and the ambient fluid. The right

subfigure shows a 2D pressure contour on the selected YZ plane (x=-43m). It is noted that the blade section has an S826 airfoil shape.

Figures 5.32 and 5.33 show that pressure in the mid-region of the blade is larger than that compared with the root region. The pressures are very high at both the leading edge and the trailing edge for the near-tip plane. The pressure contour can be explained by the fact that the line velocities are both very larger in the leading edge and the trailing edge. The integral pressure of Case Three is also the largest compared to Cases One and Two.

Velocity streamlines for different cross sections

The velocity streamlines for the three cross-sections are shown in the following three figures, including the fluid streamlines for the cross section near the root region (at x=-10m) is shown in Figure 5.34, the fluid streamlines for the cross section near in the mid (at x=-35m) in Figure 5.35 and the fluid streamlines for the cross section near the tip (at x=-43m) in Figure 5.36.

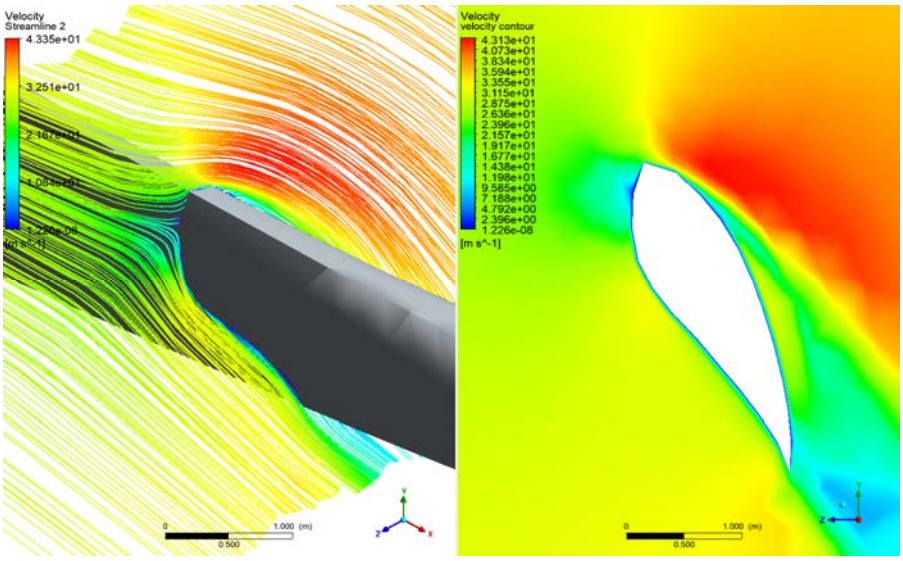

Figure 5.34: Fluid streamlines for the wind fluid near the root region. The left is a 3D sketch of the YZ plane and the fluid streamlines for ambient fluid around the blade. The right subfigure shows a 2D pressure contour on the selected YZ plane (x=-10m). It is noted that the blade section has an S818 airfoil shape.

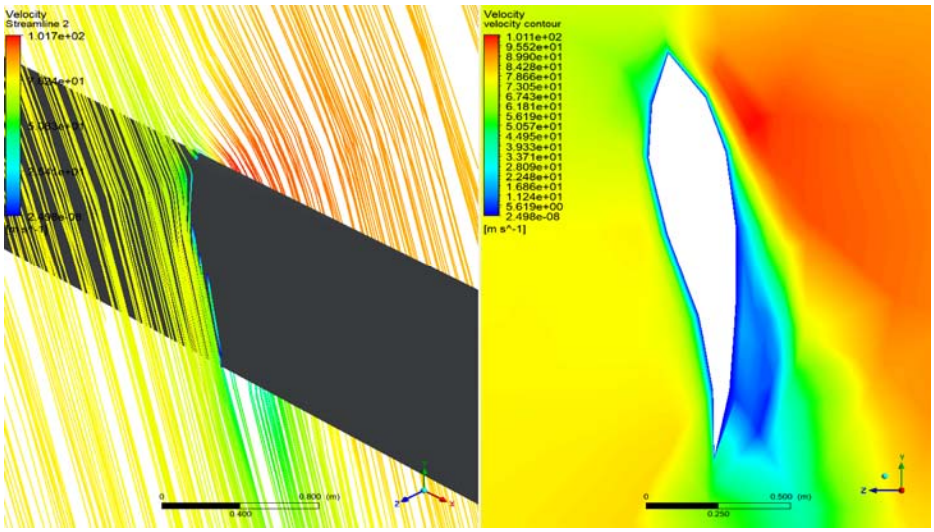

Figure 5.35: Fluid streamlines for the wind fluid near the mid blade region. The left is a 3D sketch of the YZ plane and the fluid streamlines for ambient fluid around the blade.

The right subfigure shows a 2D pressure contour on the selected YZ plane (x=-35m). It is noted that the blade section has an S825 airfoil shape.

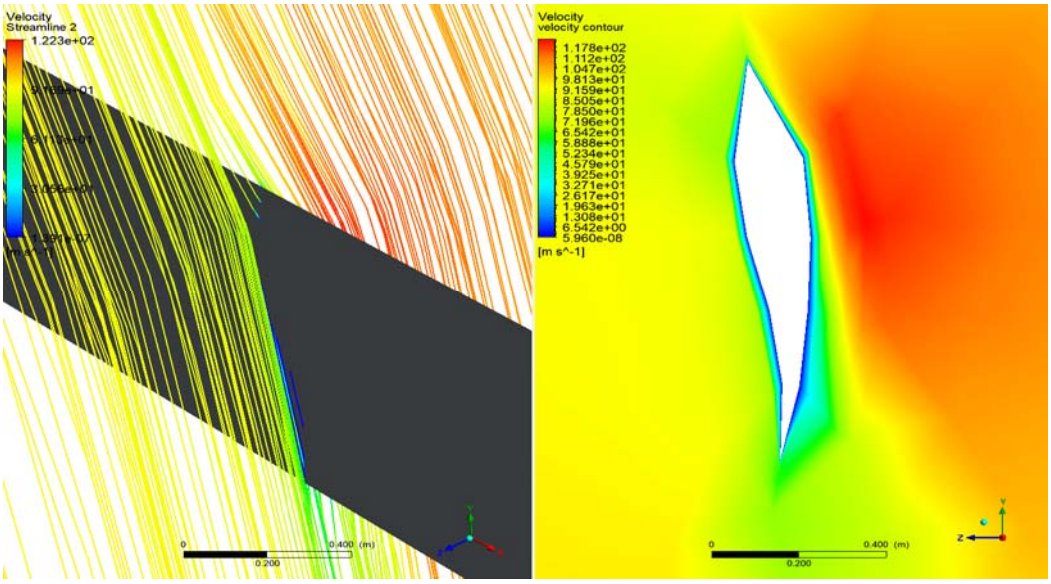

Figure 5.36: Fluid streamlines for the wind fluid near the root region. The left is a 3D sketch of the YZ plane and the fluid streamlines for ambient fluid around the blade. The right subfigure shows a 2D pressure contour on the selected YZ plane (x=-43m). It is noted that the blade section has an S826 airfoil shape.

Figures 5.34 to 5.36 show that the velocities are relatively larger in the leading edge region compared with that in the trailing edge. The velocity is highest in the tip region, among the root, mid and the tip regions. The velocity in Case Three compared with Case One and Two is also the largest, since Case Three has the largest surface wind velocity. For the pressure contours, it is also observed that the outer 2/3 of the blade has a relatively large pressure, while the pressure is smaller in the inner 1/3 region of the blade.

In this chapter, the aerodynamics of the wind turbine blade under three different inflow wind velocities are examined. It is shown higher inflow wind speed can realistically impact the turbine blade performance in terms of increasing pressure and larger velocities. It is observed in this section that the blade leading edge has a larger pressure compared with other regions of the blade. The velocity streamlines also show that the kinetic energy is large near the tip region, which explains why most of the wind energy is captured from the outer 1/3 of the blade.

CHAPTER 6

3D SIMULATIONS OF RAIN DROPLET PARTICLES

In this chapter, the discrete phase model (DPM) is used to simulate rain droplet particles. The rain droplets are assumed uniformly distributed over the entire domain with the same radius R. In this chapter, both the mean rain droplet radius and the median droplet radius are used for the simulations. Five different rain intensities are considered for the three different wind conditions. The three different wind cases considered in this work as discussed in Chapter 5 are featured by the inflow wind speed of $5ms^{-1}$,$12ms^{-1}$, and $22ms^{-1}$ respectively. For each inflow wind scenario, the five simulated rain intensities are: $20mmh^{-1}, 40mmh^{-1}, 60mmh^{-1}, 80mmh^{-1}$ and $100mmh^{-1}$.

A New Rain Droplet Model

In this section, a new rain droplet model is proposed to relate the rain intensity to rain droplet size. The model is based on the commonly accepted Marshall-Palmer rain droplet distribution function and an empirical rain intensity-droplet number relationship. The sketch of the computational domain is shown here again in Figure 6.1, which has been discussed in Chapter 4.

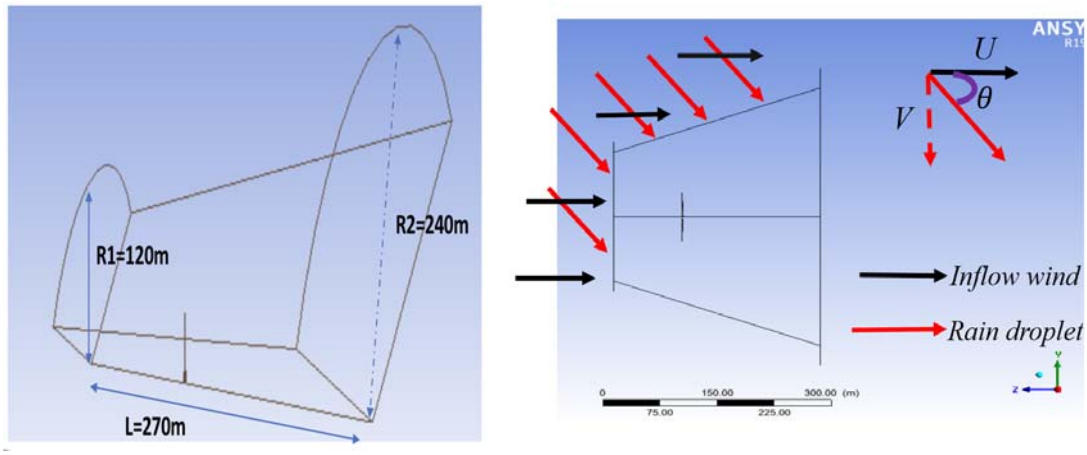

Figure 6.1: A sketch of the computational domain and the rainfall directions. The red and black arrows represent the inflow wind and particle respectively. The inflow wind velocity is U and the vertical component of the terminal velocity of a droplet is V.

By definition, the rain flux for a specific rain intensity RR can be calculated using the mass flux equation,

$$Fx_R = \rho_p S_t RR \tag{6.1}$$

where ρ_p as defined is particle density, S_t is the surface area, which is perpendicular to the rain fall. The surface area can be estimated using,

$$S_t = \pi(R_1^2 + R_2^2)cos\theta \tag{6.2}$$

where R_1 and R_2 are the radius of the left and right circular lateral surface of the computational domain as shown in Figure 6.1, θ is the angle between the inlet wind velocity U and the particle terminal velocity V. The angle θ can be calculated using the geometry relationship,

$$cos\theta = \frac{U}{\sqrt{U^2 + V^2}} \tag{6.3}$$

where U and V as defined are the free surface wind and the particle terminal velocity respectively. The particle terminal velocity can be determined using an empirical equation for a limited range of particle radii from [Stull, 2000],

$$\mathrm{V} = -\mathrm{c}\left[V_0 - \exp\left(\frac{R_0 - R}{R_1}\right)\right] \tag{6.4}$$

where the three parameters as mentioned are given as $V_0 = 12m/s$, $R_0 = 2.5mm$ and $R_1 = 1mm$. The parameter c is a density correction factor, which can be estimated using $\mathrm{c} = \sqrt{70/P}$, where P is the ambient pressure.

For the rain droplet characterized radius, the median value, $\mathrm{R_{50}}(= 0.5\mathrm{D_{50}})$ value is used to represent the particle size. The $\mathrm{R_{50}}$ value is a representative (median) value of the droplets. For example, the $\mathrm{R_{50}}$ value has been used in the sediment transport field to represent the size property of the sediments. The $\mathrm{R_{50}}$ value is computed using the formula [Yakubu et al., 2016] (recall Equation 2.4)

$$R_{50} = 1.635 - 0.816\exp(-0.04RR) \tag{6.5}$$

The distribution described by Equation 6.5 is shown in Figure 6.3. The result shows that the increase in rain intensity, $\mathrm{R_{50}}$ increases. This is not surprising, as intense rainfall can generate more large droplets, therefore, $\mathrm{R_{50}}$ value increases.

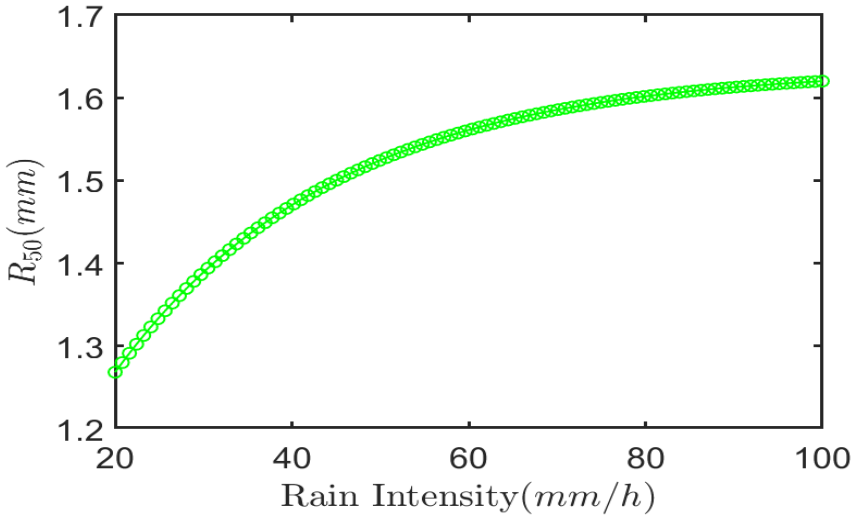

Figure 6.3: The median R_{50} values of the rain droplet particles for a given rain intensity.

The median rain droplet R_{50} value is discussed in the following paragraph.

In the following sections, the rain droplets are simulated using the DPM for different inflow wind and rain intensity conditions. The particles are assumed uniformly distributed in space and the R_{50} values are used as the specific rain droplet radius. The radius range is also decreased and set (R_{s50}) to about 15−20% of the R_{50} values to run an additional series of simulations. Thus for each of the wind speed simulations presented there is one set of results for the R_{s50} values and one set for the R_{50}values. Once the rainfall intensity is predetermined, Figure 6.3 is used to determine the characterized rain droplet radii, R_{50}. Then it is assumed that all the particles in the domain have the same characterized radius. The total number of the particles in the domain can be calculated using the total volume of the rain in the domain over the volume of each rain droplet according to R_{50} or R_{s50}values.

In the simulations, the rain droplets are introduced at the top of the domain along with the red arrows while the inflow velocity is horizontal along with the black arrows (shown in Figure 6.1). As the turbine blade rotates, the velocity streamlines are deflected (this will be discussed later) producing an angle of attack to the blade. The effect of the inflow wind is also to change the angle of the rain droplets. The objective of the simulations is to understand the efficiency of the blade surface in terms of how many of the incoming rain droplets strike the blade and how this impact efficiency changes with wind speed and rainfall intensity/droplet size. In the following sections, several different inflow wind velocities are used to observe the influence of the wind velocity on the rain droplet responses. Moreover, for each specific wind velocity, five different rain intensities will be used to see how many rain droplets can be trapped by the wall. If the rain intensity increases, that means the rain droplet sizes and the terminal velocity will also change. In sum, a total of 15 different rain scenarios are simulated. The results of each simulation run are shown in the following sections.

Case 1: When Inflow Wind Velocity Is $\mathbf{5ms^{-1}}$

For an inflow wind velocity of 5ms^{-1}, 5 different rain intensities are used as summarized in Table 6.1. Two different rain droplet radius, R_{50} and the R_{s50} based on the proposed rain texture model are used.

Particle trajectories

First, using the R_{50} value, some representative particle trajectories of the five different rain intensities are shown in the following figures. The particle trajectories when the rain intensity is set at 20 mmh^{-1} is shown in Figure 6.4, when the rain intensity is set at 40mmh^{-1} is shown in Figure 6.5, when the rain intensity is set at 60mm/h is shown in Figure 6.6, when the rain intensity is set at 80mmh^{-1} is shown in Figure 6.7 and when the rain intensity is set at 100mmh^{-1} is shown in Figure 6.8. The simulation conditions and results are all listed in the tables of each subsection.

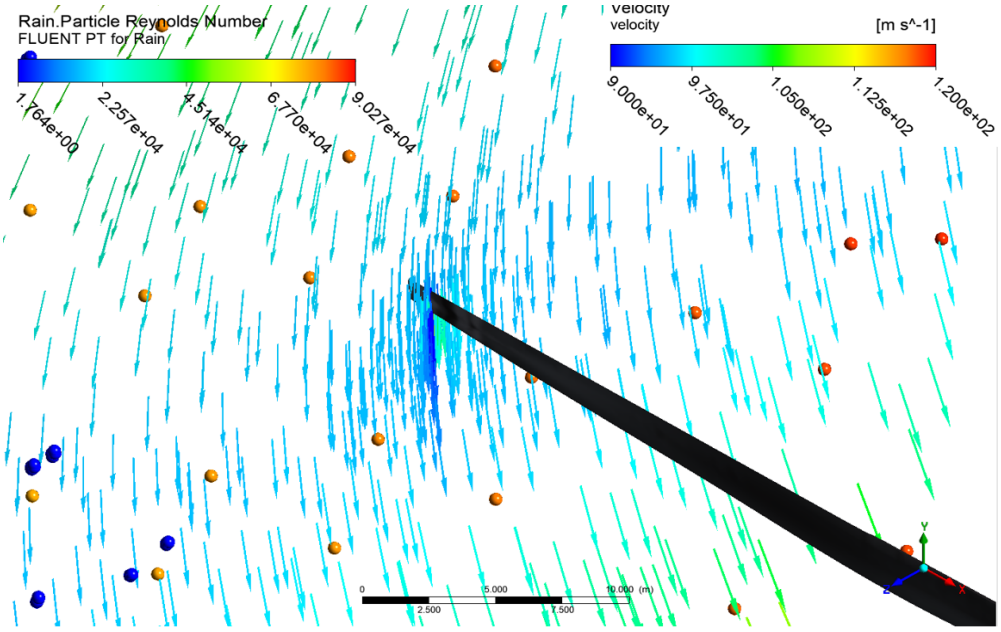

Figure 6.4: Particle trajectories of the rain droplets when the rainfall intensity is $20mmh^{-1}$.

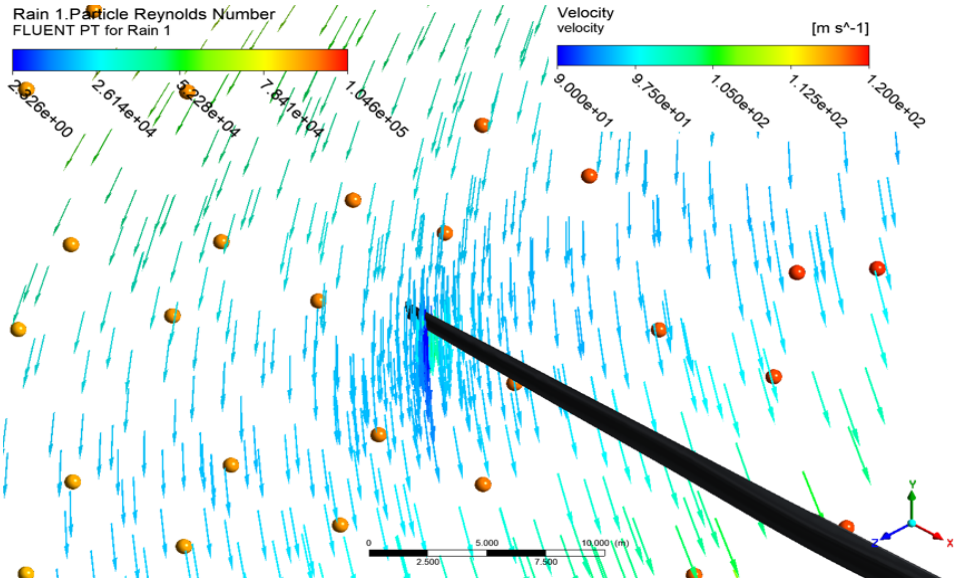

Figure 6.5: Particle trajectories of the rain droplets when the rainfall intensity is $40mmh^{-1}$.

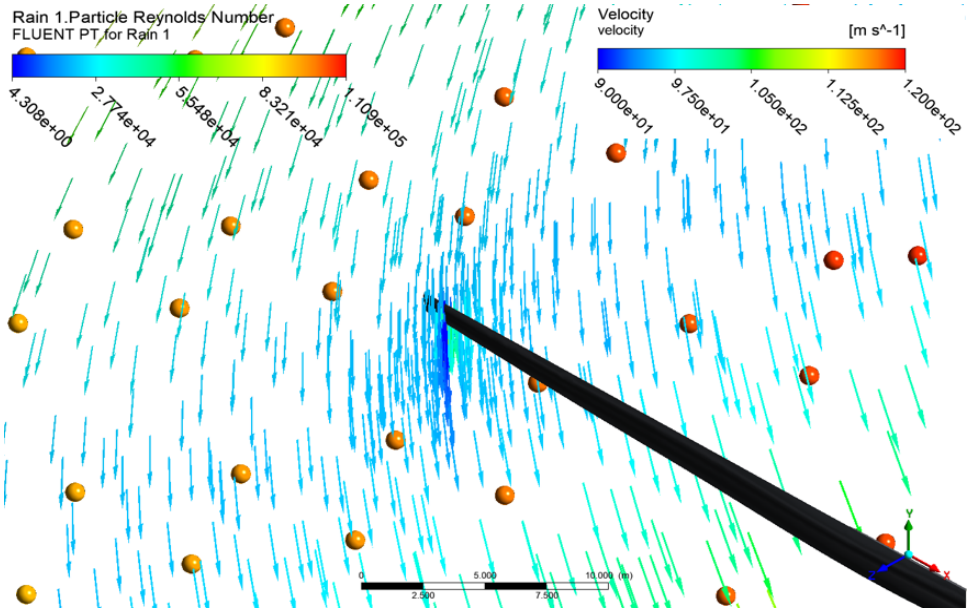

Figure 6.6: Particle trajectories of the rain droplets when the rainfall intensity is $60mmh^{-1}$.

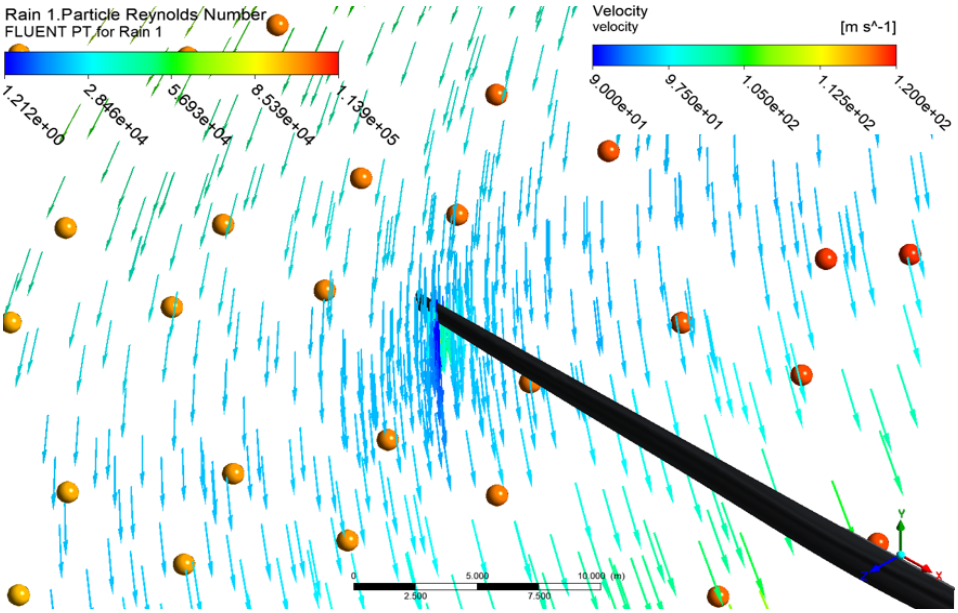

Figure 6.7: Particle trajectories of the rain droplets when the rainfall intensity is $80mmh^{-1}$.

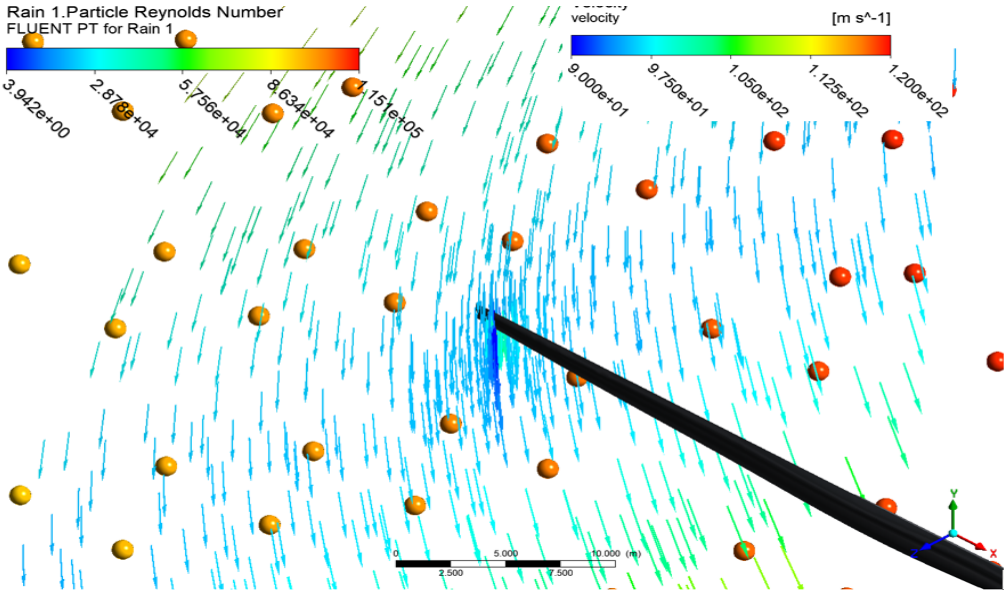

Figure 6.8: Particle trajectories of the rain droplets when the rainfall intensity is $100mmh^{-1}$.

It is observed from Figures 6.4 to 6.8 that the particle trajectories are closely related to the streamlines. Further away from the turbine blade, the trajectories of the particles are driven by the free stream wind and gravity due to mass. However, as the particles move closer towards the blades, the particles are strongly influenced by the turbine blade. Over the whole domain, it is observed that only a small portion of the particles is influenced by the blade.

Particle collections

As the rain intensity becomes larger, the particle sizes used in these simulations also increase. The number of particles that are trapped (collected) by the blade also increases. We assume this to mean that the particles impact the blade. We are using a small size range, however, once the particle size becomes larger than a critical size value, the percentage of particles that are trapped by the blade decreases. To make the result clear, the number of particles trapped collected are shown in Table 6.1 and 6.2. In Table 6.1, the R_{50} value is used, while in 6.2, the R_{s50} is used. In these tables, "Total" refers to the total number of particles in the domain, which is computed by dividing the total volume of rain over the volume of a single droplet featured by a specific radius. "Trapped" means the number of particles that are trapped/collected by the blade and "Ratio" is a ratio of Trapped to Total.

Table 6.1: Simulation conditions and result with R_{50} for the case when $U = 5ms^{-1}$

RR	***U***	***R_{50}***	***V***	***Cosθ***	***S_t***	***Fx_R***	***Total***	***Trapped***	***Ratio***

mm/h	*m/s*	*mm*	*m/s*	*-*	*m^2*	*kg/s*	*#/s*	*#/s*	*%*
20	5	1.27	8.57	0.50	113948.60	633.05	7.40E+07	4.55E+04	0.06%
40	5	1.47	9.20	0.48	108011.66	1200.13	9.01E+07	1.11E+05	0.12%
60	5	1.56	9.44	0.47	105849.62	1764.16	1.11E+08	1.36E+05	0.12%
80	5	1.60	9.54	0.46	104962.26	2332.49	1.36E+08	8.33E+04	0.06%
100	5	1.62	9.59	0.46	104579.18	2904.98	1.63E+08	1.00E+05	0.06%

Table 6.2: Simulation conditions and result with R_{s50} for the case when U $= 5ms^{-1}$

RR	*U*	*R_{s50}*	*V*	*Cosθ*	*S_t*	*Fx_R*	*Total*	*Trapped*	*Ratio*
mm/h	*m/s*	*mm*	*m/s*	*-*	*m^2*	*kg/s*	*#/s*	*#/s*	*%*
20	5	0.23	2.30	0.91	205446.37	1141.37	2.29E+10	1.41E+07	0.061%
40	5	0.23	2.33	0.91	204961.11	2277.35	4.39E+10	2.70E+07	0.061%
60	5	0.23	2.35	0.91	204763.56	3412.73	6.47E+10	3.97E+07	0.061%
80	5	0.23	2.37	0.90	204459.20	4543.54	8.39E+10	5.16E+07	0.061%
100	5	0.24	2.38	0.90	204306.82	5675.19	1.03E+11	6.36E+07	0.061%

Table 6.1 and Table 6.2 both show that with the increasing rain intensities, more particles are generated in the domain. Compared with all the particles in the domain, only a small portion (~0.1%) of the particles are trapped by the blade. No particles are reflected by the blade. Comparing Table 6.1 with Table 6.2 indicates that the number of particles trapped by the blade does not change much. This plausibly suggests that over the small range of particle radius used here, the particle radius is not the most dominating factors in governing the particle interaction with the blade. The rain intensity, however, is very important in blade-rain droplet interaction. If the rain intensity increases, more and more particles are trapped by the wall although the percentage of particles trapped does not change much. If the rainfall intensity becomes larger than a critical value, then the percentage of particles that can be trapped by the wall decreases, as shown in Table 6.1.

Case 2: When Inflow Wind Velocity Is $12ms^{-1}$

For the operational wind condition where the inflow wind velocity is $12ms^{-1}$, five different rain intensities are used and summarized in Tables 6.5 and 6.6. Two different rain droplet diameters based on the proposed rain droplet model are also used. First, using the R_{50} value, some representative particle trajectories of the five different rain intensities are shown in the following figures.

Particle trajectories

The particle trajectories when the rain intensity is set at $20mmh^{-1}$ is shown in Figure 6.9.

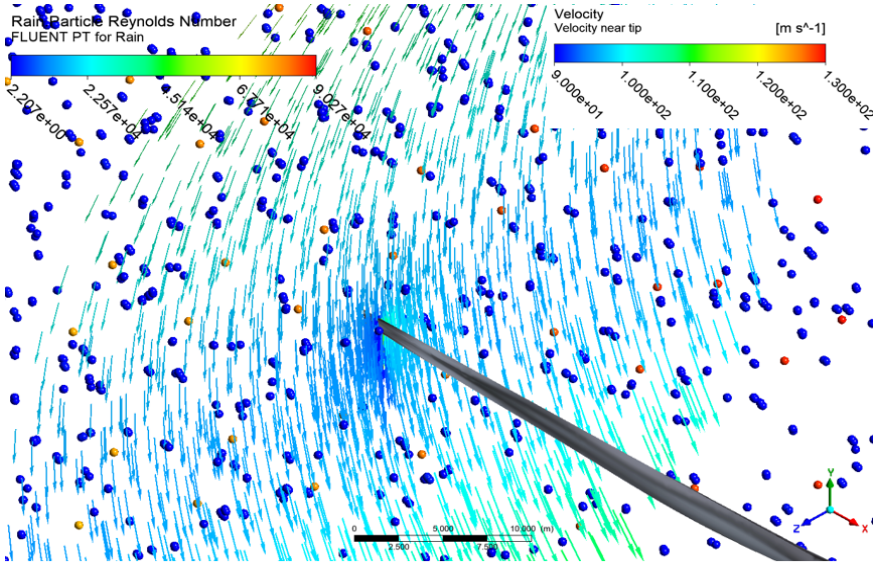

Figure 6.9: Particle trajectories of the rain droplets when the rainfall intensity is $20mmh^{-1}$.

The particle trajectories when the rain intensity is set at $40mmh^{-1}$ is shown in Figure 6.10.

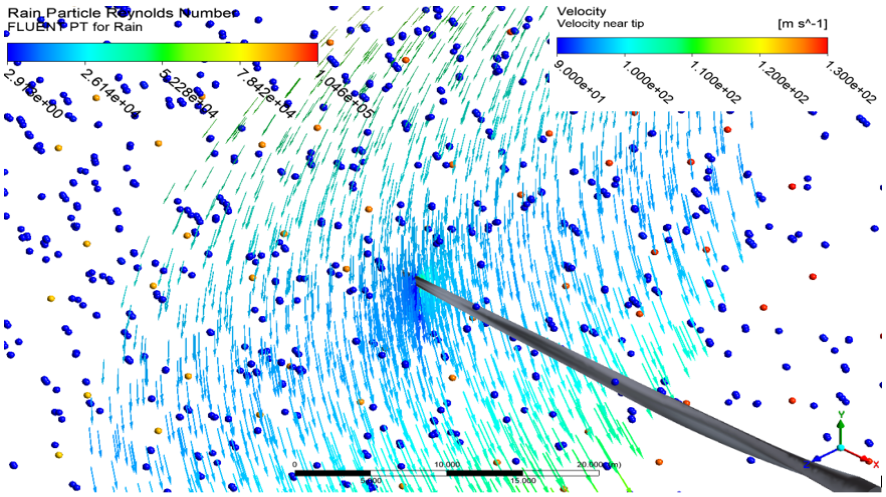

Figure 6.10: Particle trajectories of the rain droplets when the rainfall intensity is $40mmh^{-1}$.

The particle trajectories when the rain intensity is set at $60mmh^{-1}$ is shown in Figure 6.11.

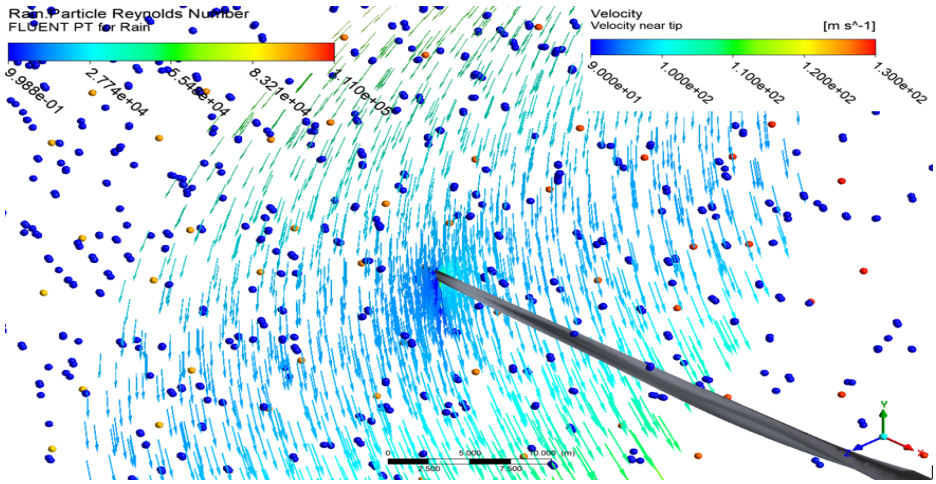

Figure 6.11: Particle trajectories of the rain droplets when the rainfall intensity is $60mmh^{-1}$.

The particle trajectories when the rain intensity is set at $80mmh^{-1}$ is shown in Figure 6.12.

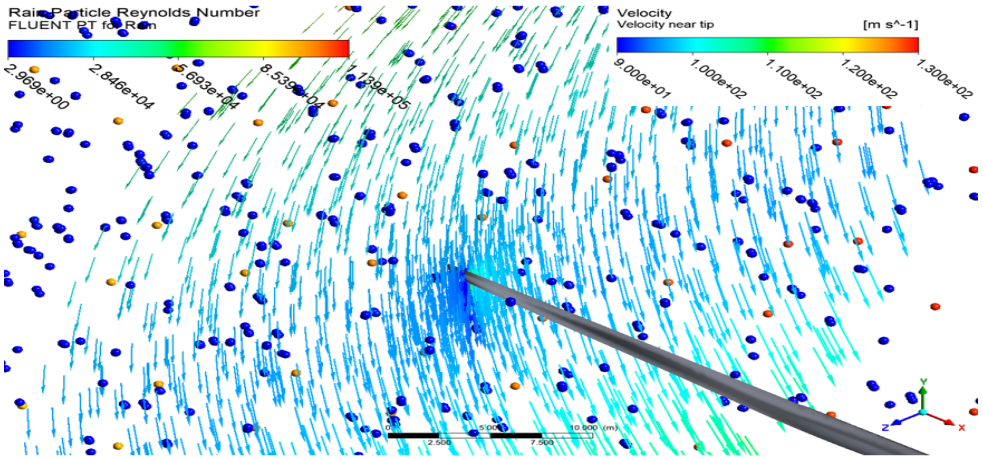

Figure 6.12: Particle trajectories of the rain droplets when the rainfall intensity is $80mmh^{-1}$.

The particle trajectories when the rain intensity is set at $100mmh^{-1}$ is shown in Figure 6.13.

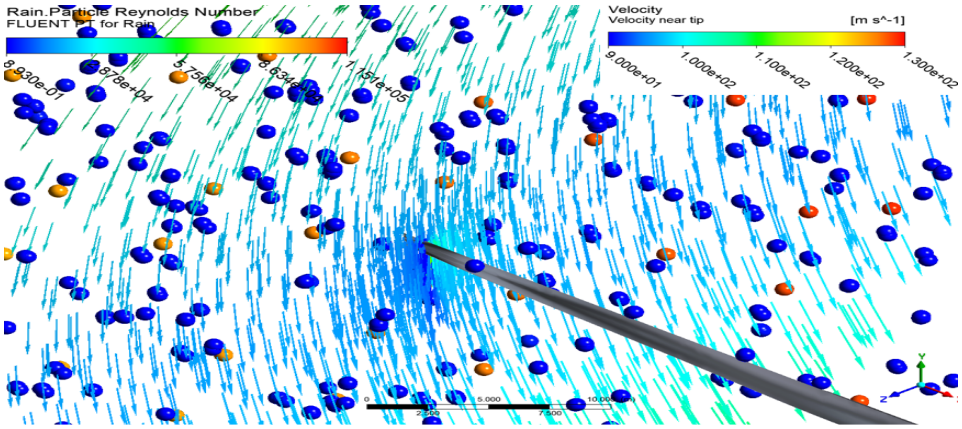

Figure 6.13: Particle trajectories of the rain droplets when the rainfall intensity is $100mmh^{-1}$.

It is observed from Figures 6.9 to 6.13 that the particle trajectories are closely related to the streamlines. Further away from the turbine blade, the particles are driven by the free stream wind and the gravity due to mass. However, as the particles are moving closer towards the blades, the particles are strongly influenced by the tip velocity which is generated due to the blade rotation. It is observed that only a small portion of the particles are influenced by the blade. This observation is similar to the results shown in Figures 6.4 to 6.8.

Particle collections

The number of particles in the whole domain and those trapped by the blade is shown in Table 6.3 and 6.4. In Table 6.3, the R_{50} value is used, while in Table 6.4, the R_{s50} value is used.

Table 6.3: Simulation conditions and result with R_{50} for the case when $U = 12ms^{-1}$

RR	***U***	***R_{50}***	***V***	***Cosθ***	***S_t***	***Fx_R***	***Total***	***Trapped***	***Ratio***
mm/h	***m/s***	***mm***	***m/s***	***-***	***m^2***	***kg/s***	***#/s***	***#/s***	***%***
20	12	1.27	8.57	0.81	184044.37	1022.47	1.20E+08	7.35E+04	0.06%
40	12	1.47	9.20	0.79	179510.08	1994.56	1.50E+08	2.76E+05	0.18%
60	12	1.56	9.44	0.79	177759.82	2962.66	1.86E+08	2.29E+05	0.12%
80	12	1.60	9.54	0.78	177025.48	3933.90	2.29E+08	2.81E+05	0.12%
100	12	1.62	9.59	0.78	176705.53	4908.49	2.76E+08	3.39E+05	0.12%

Table 6.4: Simulation conditions and result with R_{s50} for the case when U $= 12ms^{-1}$

RR	***U***	$\boldsymbol{R_{s50}}$	***V***	***Cosθ***	$\boldsymbol{S_t}$	$\boldsymbol{Fx_R}$	***Total***	***Trapped***	***Ratio***
mm/h	***m/s***	***mm***	***m/s***	***-***	$\boldsymbol{m^2}$	***kg/s***	***#/s***	***#/s***	***%***
20	12	0.228	2.30	0.98	222140.17	1234.11	2.48E+10	4.57E+06	0.018%
40	12	0.231	2.33	0.98	222033.37	2467.04	4.75E+10	2.51E+07	0.053%
60	12	0.233	2.35	0.98	221989.72	3699.83	7.01E+10	4.05E+07	0.058%
80	12	0.235	2.37	0.98	221922.27	4931.61	9.11E+10	5.49E+07	0.060%
100	12	0.236	2.38	0.98	221888.41	6163.57	1.12E+11	6.91E+07	0.061%

Table 6.3 and Table 6.4 both show that with the increasing rain intensities, more particles are generated in the domain. Compared with all the particles in the domain, only a small portion of the particles are trapped by the blade. No particles are reflected by the blade, which may indicate that most of the rain droplets are able to maintain their own trajectories. This observation is similar to the case when $U = 5ms^{-1}$.

Comparing Tables 6.3 and 6.4 with Table 6.1 and 6.2 indicates that the number of particles trapped by the blade does vary. In Table 6.3 when the wind velocity increases, the number of particles trapped by blade also increases. However, when the particle radius becomes larger than $1.56mm$, the number of particles trapped by the blade does not change. This may plausibly suggest that a critical value of particle size under current wind condition has been achieved. In Table 6.4, the particle sizes are smaller than those in Table 6.3, the percentage of particles trapped by the blade increases slightly if the particle radius increases.

Case 3: When Inflow Wind Velocity Is $22ms^{-1}$

For the surface wind velocity of $22ms^{-1}$ when the turbine will still be operating at its rated capacity, five different rain intensities are used are also summaries in Tables 6.5 and 6.6. Two different rain droplet diameters based on the proposed rain texture model are used.

Particle trajectories

First, using the R_{50} value, some representative particle trajectories of the five different rain intensities are shown in the following figures.

The particle trajectories when the rain intensity is set at $20\text{m}mh^{-1}$ is shown in Figure 6.14.

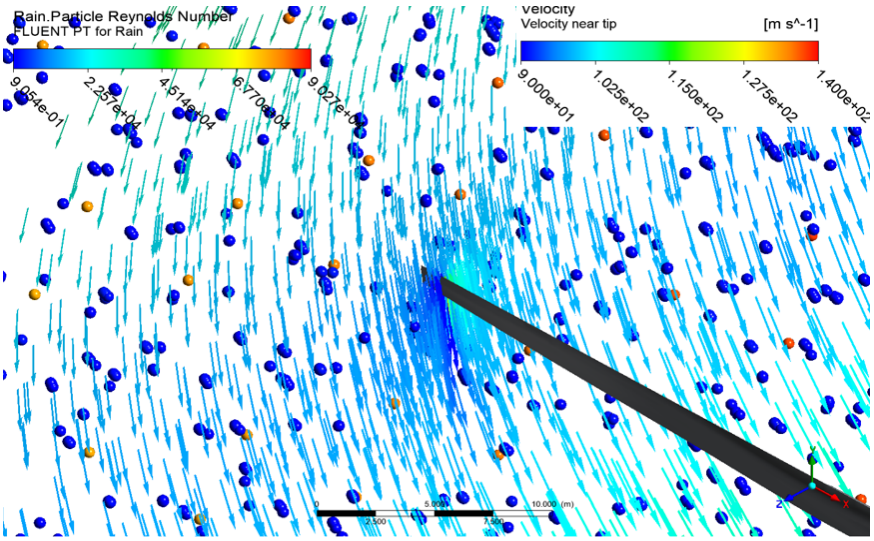

Figure 6.14: Particle trajectories of the rain droplets when the rainfall intensity is $20mmh^{-1}$.

The particle trajectories when the rain intensity is set at $40mmh^{-1}$ is shown in Figure 6.15.

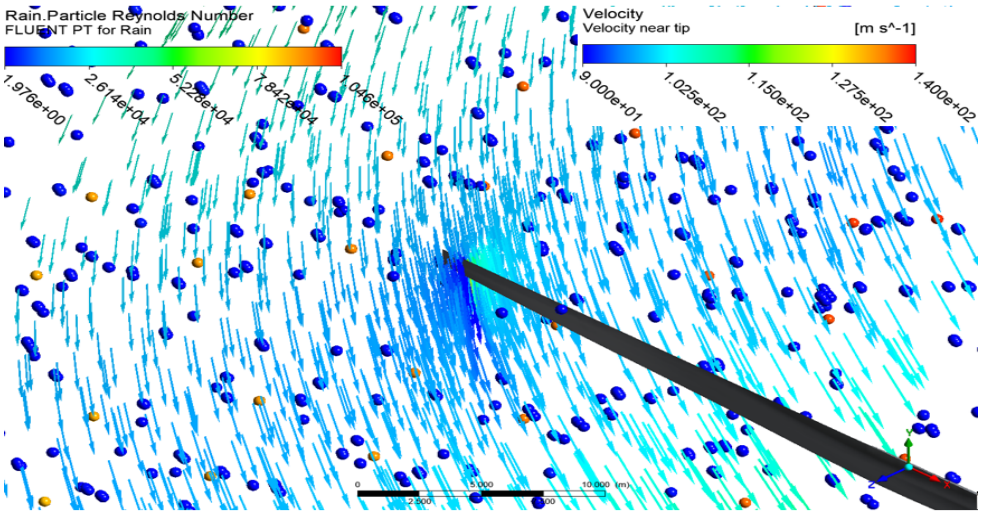

Figure 6.15: Particle trajectories of the rain droplets when the rainfall intensity is $40mmh^{-1}$.

The particle trajectories when the rain intensity is set at $60mmh^{-1}$is shown in Figure 6.16.

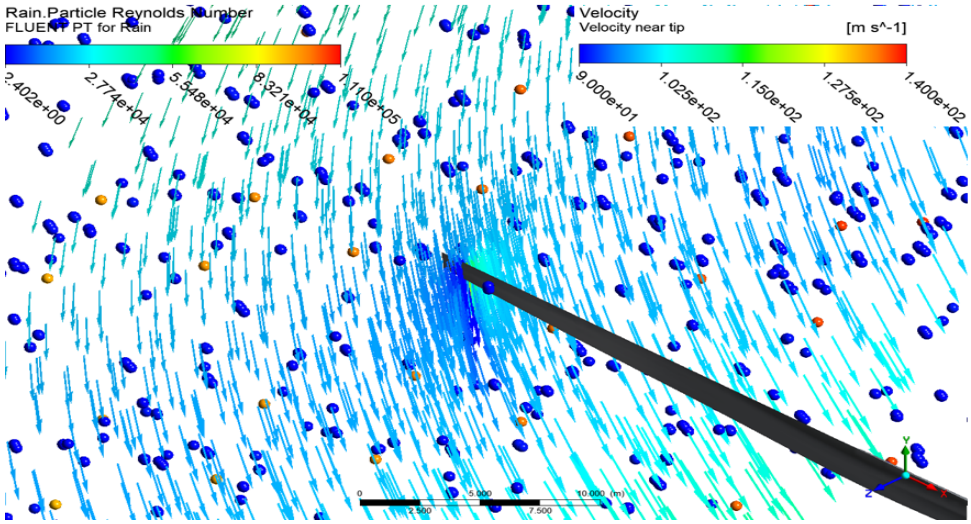

Figure 6.16: Particle trajectories of the rain droplets when the rainfall intensity is $60mmh^{-1}$.

The particle trajectories when the rain intensity is set at $80mmh^{-1}$ is shown in Figure 6.17.

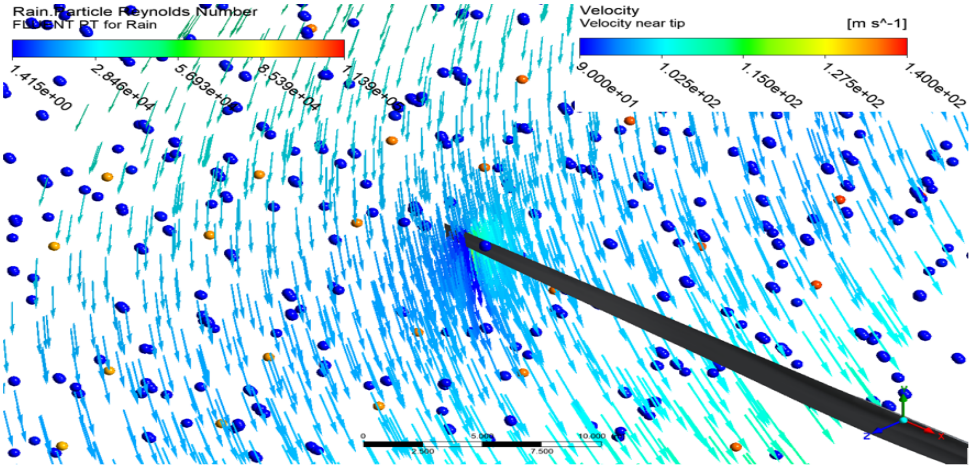

Figure 6.17: Particle trajectories of the rain droplets when the rainfall intensity is $80mmh^{-1}$.

The particle trajectories when the rain intensity is set at $100mmh^{-1}$ is shown in Figure 6.18.

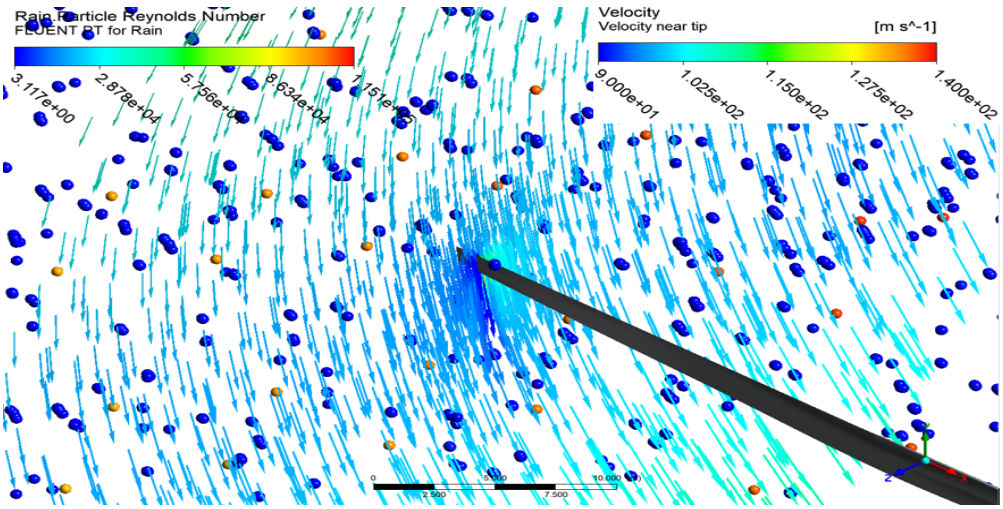

Figure 6.18: Particle trajectories of the rain droplets when the rainfall intensity is 100m/h

It is observed from Figures 6.14 to 6.18 that the particle trajectories are closely related to the streamlines. Further away from the turbine blade, the particles are driven by the free stream wind and the gravity due to mass. However, as the particles are moving closer towards the blades, the particles are strongly influenced by the tip velocity which is generated due to the blade rotation. It is observed that only a small portion of the particles are influenced by the blade. This observation is similar to the results shown in Figures 6.4 to 6.13.

Particle collections

The number of particles in the whole domain and those trapped are shown in Table 6.5 and 6.6. In Table 6.5, the R_{50} value is used, while in Table 6.6, the mean R_{s50} value is used.

Table 6.5: Simulation conditions and result with R_{50} for the case when $U = 22ms^{-1}$

RR	***U***	***R_{50}***	***V***	***Cosθ***	***S_t***	***Fx_R***	***Total***	***Trapped***	***Ratio***
mm/h	***m/s***	***mm***	***m/s***	***-***	***m^2***	***kg/s***	***#/s***	***#/s***	***%***
20	22	1.27	8.57	0.93	210755.13	1170.86	1.37E+08	1.68E+05	0.12%
40	22	1.47	9.20	0.92	208682.91	2318.70	1.74E+08	2.14E+05	0.12%
60	22	1.56	9.44	0.92	207857.59	3464.29	2.17E+08	2.67E+05	0.12%
80	22	1.60	9.54	0.92	207507.00	4611.27	2.68E+08	1.65E+05	0.06%
100	22	1.62	9.59	0.92	207353.43	5759.82	3.23E+08	1.99E+05	0.06%

Table 6.6: Simulation conditions and result with R_{s50} for the case when U $= 22ms^{-1}$

RR	***U***	$\boldsymbol{R_{s50}}$	***V***	***Cosθ***	$\boldsymbol{S_t}$	$\boldsymbol{Fx_R}$	***Total***	***Trapped***	***Ratio***
mm/h	***m/s***	***mm***	***m/s***	***-***	$\boldsymbol{m^2}$	***kg/s***	***#/s***	***#/s***	***%***
20	22	0.228	2.303	0.995	224965.242	1249.807	2.51E+10	0.00E+00	0.00%
40	22	0.231	2.334	0.994	224932.223	2499.247	4.82E+10	5.33E+06	0.01%
60	22	0.233	2.347	0.994	224918.718	3748.645	7.10E+10	1.57E+07	0.02%
80	22	0.235	2.366	0.994	224897.839	4997.730	9.23E+10	4.20E+07	0.05%
100	22	0.236	2.376	0.994	224887.353	6246.871	1.14E+11	6.72E+07	0.06%

Table 6.5 and Table 6.6 both show that with the increasing rain intensities, more particles are generated in the domain. Compared with all the particles in the domain, only a small portion (~0.1%) of the particles are trapped by the blade. No particles are reflected by the blade, which may indicate that most of the rain droplets are able to maintain their own trajectories. If the rain intensity increases, more and more particles are trapped by the wall. If the rainfall intensity becomes larger than a critical value, then the number of particles that can be trapped by the wall decreases.

Compared with Tables 6.1-6.6, it is clear that the number of particles which are trapped by the blade increases, when the rain intensity increases. This is especially clear when the small radius range is used. In addition, it may also suggest that the number of particles collected by the blade is strongly related to the wind velocity.

Rain Droplet Collection Rate near Blade

In this section, the number of particles which are collected by the blade is discussed locally in the vicinity of the blade. The blade is considered as a wall, where the wind flow is obstructed by it. For the blade wall, the no-slip boundary condition is applied in the rotational coordinate system. To help understand the mechanism of how the wind flow can influence the particle transport processes, the turbulent boundary layer in introduced here. As shown in Figure 6.20, the boundary layer thickness of turbulent flow over an airfoil is given as δ.

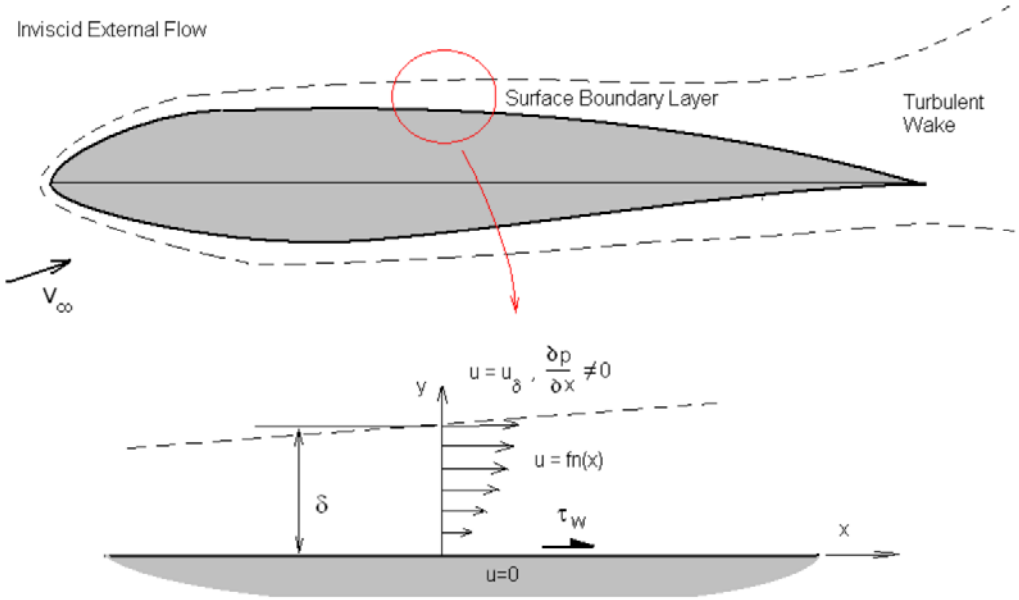

Figure 6.19: Boundary layer thickness of turbulent flow over a flat plane[4]. The definition of all the parameters can be found from the webpage herein. Since they are not the focus of the present work, it is hence not repeated here.

[4] The figure is reproduced from webpage: http://www.aerodynamics4students.com

It is shown in Figure 6.19 that within the turbulence boundary layer in the vicinity of the blade, the fluid characteristics are mainly determined by the near-wall (viscous layer) flow [Hansen, 2015]. Therefore, it is assumed that the region where the transport properties are determined by the turbine blade wall is the region covered by the turbulent boundary layer here. Although this assumption is not perfect, many studies [Brendel and Mueller, 1988; Kerho and Bragg, 1997; Samson and Sarkar, 2016; Moreau et al., 2016] adopt it and show the suitability of it compared with the experimental data. The turbulent boundary layer thickness can be approximated as,

$$\delta = 0.37\mathrm{x}/Re_x^{1/5} \tag{6.6}$$

where

$$Re_x = \rho U x/\mu \tag{6.7}$$

where is the x is the distance downstream from where the boundary layer starts (shown in Figure 6.12), ρ and μ as defined are the air density and dynamic viscosity respectively.

Figure 6.19 implies the boundary viscous layer may contribute to the mechanisms that the high-speed particles are trapped by the wall. For simplification, it is assumed that the entire surface of the blade leading edge surface is able to capture particles. The surface area of the leading edge can be obtained from the geometry shown in Figure 6.20.

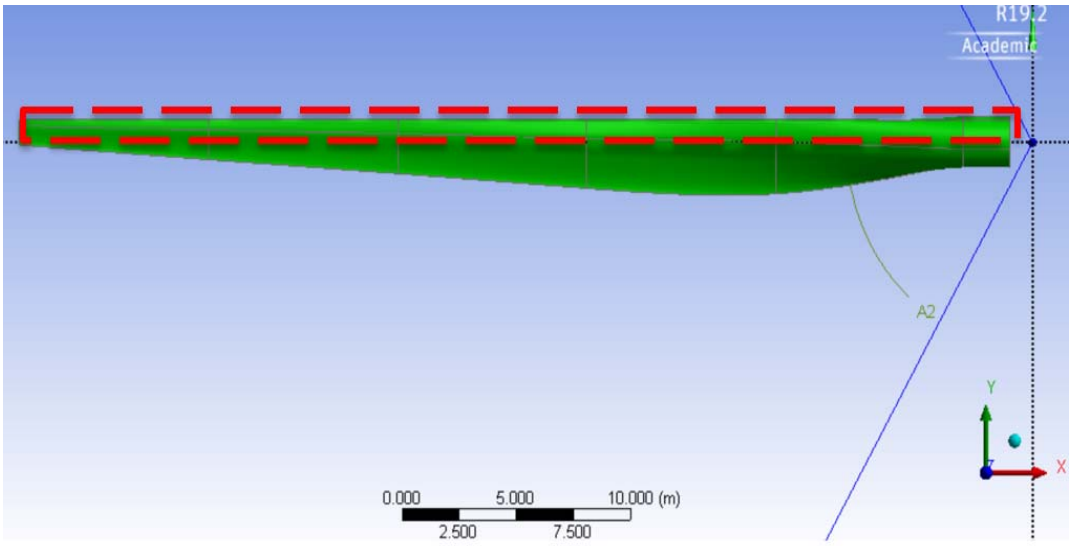

Figure 6.20: Surface area of the blade leading edge. The leading edge of the blade is shown in the red dashed rectangular, which is about 20% of the entire blade.

For a single blade, the area of the leading edge can be computed directly from the geometric configurations. For the modeled blade in this work, the surface areas of the leading edge (S_{bl}) and the entire blade (S_{be}) are given as $68.53m^2$ and $213.23m^2$.

As shown in the Tables 6.1-6.6, the trapping efficiency tends to increase as particle size increase but this does not hold uniformly. It is also highest in the 12 ms^{-1} cases when the blade aerodynamics should be working most efficiently. The trapping efficiency is a maximum of 0.18% for the 12 ms^{-1} cases with a moderate rainfall rate of 40 mm/hr and a radius of 1.47 mm. It is unclear why this should be the case and why there are relatively fewer impacts with the presence of more rain droplets in the domain. The complex interaction of the blade aerodynamics with the particle size and rainfall rate needs further investigation.

Tentatively, a plausibly simple explanation is put here. In the absence of any rotation, we could reasonably expect the leading edge to trap the same number of particles as any other part of the domain and it would, therefore, the maximal number of the particles that can be trapped is given as,

$$N_{sm} = \frac{3S_{bl}cos\theta}{4\pi R^3} \times \frac{\mathrm{RR}}{1000} \times \frac{1}{3600} \tag{6.8}$$

For comparison, the simulated results are the maximal stationary results are shown in Table 6.7.

Table 6.7: The comparisons between different results. The comparison is made between the maximal number of rain droplets that can be trapped by the blade for one cycle when the blade is not rotating and the actual number of particles that are captured by the blade from simulations.

U	RR	$N_{sm}(R_{50})$	$N_s(R_{50})$	$Ratio$	$N_{sm}(\boldsymbol{R_{s50}})$	$N_s(\boldsymbol{R_{s50}})$	$Ratio$
m/s	*mm/h*	*#/s*	*#/s*	*-*	*#/s*	*#/s*	*-*
5	20	2.24E+04	4.55E+04	2.03	5.82E+06	1.41E+07	2.03
	40	2.73E+04	1.11E+05	4.06	1.11E+07	2.70E+07	2.03
	60	3.35E+04	1.36E+05	4.06	1.64E+07	3.97E+07	2.03
	80	4.11E+04	8.33E+04	2.03	2.13E+07	5.16E+07	2.03
	100	4.94E+04	1.00E+05	2.03	2.63E+07	6.36E+07	2.03
12	20	3.62E+04	7.35E+04	2.03	6.11E+06	4.57E+06	0.61
	40	4.54E+04	2.76E+05	6.09	1.17E+07	2.51E+07	1.74
	60	5.63E+04	2.29E+05	4.06	1.73E+07	4.05E+07	1.91
	80	6.92E+04	2.81E+05	4.06	2.24E+07	5.49E+07	1.99
	100	8.35E+04	3.39E+05	4.06	2.77E+07	6.91E+07	2.03
22	20	4.15E+04	1.68E+05	4.06	6.12E+06	0.00E+00	0.00
	40	5.28E+04	2.14E+05	4.06	1.17E+07	5.33E+06	0.37
	60	6.59E+04	2.67E+05	4.06	1.73E+07	1.57E+07	0.73
	80	8.12E+04	1.65E+05	2.03	2.25E+07	4.20E+07	1.50

	100	9.80E+04	1.99E+05	2.03	2.78E+07	6.72E+07	1.95

The comparison between the maximal number of rain droplets that can be trapped by the blade when the blade is not rotating and the actual number of particles that are captured by the blade from simulations is shown in Table 6.7. It is noted that $N_{sm}(R_{50})$ refers to the maximal number of the droplets that can be trapped in one cycle according to Equation 6.10 when the blade is not rotating and the R_{50} value is used for the particle terminal velocity calculation. Similarly, $N_{sm}(R_{s50})$ refers to the maximal number of the droplets that can be trapped according to Equation 6.10 when the blade is not rotating and the R_{s50} value is used for the particle terminal velocity calculation. Moreover, $N_s(R_{50})$ and $N_s(R_{s50})$ refer to the simulated results based on Tables 6.1 to 6.6 when the blade finishes one cycle of rotation. The "ratio" is a simple math ratio using the simulated values divided by the computed maximal stationary values.

It is shown in Table 6.7 that, when the blade is rotating, about 2~4 times of the rain droplet particles will be trapped by the wall when the median value is used for the rain droplet radius calculation. This implies that the rotation of the blade is more efficient at capturing particles than a flat surface. However, when we use the small-ranged radius, the magnitude of the particles that are trapped over the stationary cases falls in the range between 0.2-2.1. This may plausibly indicate the particle size is very important in influencing how many particles can be trapped to the blade. Also, it is clear from Table 6.7 that for the same wind velocity when the rain intensity increases,

relatively more particles are trapped by the wall compared with the stationary conditions. Moreover, comparing the cases when the rain intensity is the same, when the inflow wind velocity increases, the number of particles that are trapped to the blade relative to the maximal stationary cases decreases. This may be explained since the radius of the particles is small, if the inflow wind velocity is large enough, most of the particles will be influenced by the flow around the blade. The turbulent advection thus dominates the transport processes, aiding the particles to move with the streamlines.

CHAPTER 7

CONCLUSION AND FUTURE WORK

Conclusions

Blade leading edge erosion is a serious issue in wind turbine operation, which influences turbine performance and energy capture. However, little is understood of the mechanisms how the hydrometers, especially the rain droplet influences the erosion process on the leading edge. Since precipitation cannot be avoided where the turbine blades are installed, and precipitation varies extensively by amount and type, it is therefore of great scientific and practical merit to investigate how the rain droplet influences the blade leading edge erosion. It is necessary to understand quantitatively how these rain droplets contribute to the erosion process, which may finally destroy the blade if it is exposed to the natural forces without further protection. Since the physical experiments can be hard to conduct given that the large size of the blade and huge simulation domain, this thesis offers some numerical experimental results. It is hoped that the models and simulation framework built in this thesis can be heuristic in guiding future numerical simulations and laboratory experiments. The work conducted here serves as the first step towards some fundamental understandings of the blade leading edge erosion due to the rain droplets in the atmosphere.

In summary, this work achieved a goal of building a set of numerical frameworks to quantify the roles of the rain characteristics on the blade leading edge erosion. The specific conclusion is listed below.

First, a 3D wind turbine aero dynamical numerical simulation system has been built. The simulation is based on ANSYS Fluent. The geometries used in this work are based on three different airfoil shapes in different locations, so that the lift forces generated on the blade are consistent with the blade rotating direction. The wind turbine numerically simulated comprises three blades, which are identical to each other. Therefore, only 1/3 of the entire wind turbine domain is needed for conducting the numerical simulations. The numerical simulation system can be modified with different blade shape, blade length and other configurations, inlet wind velocity, and fluid temperature and density. Therefore, this system is flexible and can be used to simulate different meteorological scenarios. Moreover, a discrete phase model (DPM) for particle simulations is combined with the current wind simulation model to analyze the influence of the particles on the blade leading edge erosion. The particle tracking model allows the inlet conditions to be modified so that this system can be used to simulate more complex scenarios. The particles are currently assumed to be uniformly distributed by size and in the domain but could be modified with different user-defined functions to investigate different particle distributions.

In addition, the influence of free wind velocity on the aerodynamics of the turbine blade has been investigated. Using the numerical simulation system, three

different wind velocities are simulated and their influence on the blade performance is investigated. It is shown that the wind velocity can significantly influence the pressure field of the blade domain. When the free wind velocity increases, the corresponding pressure on the blade surface also increases, thus generating more kinetic energy. It is observed that the pressure is relatively large near the blade leading edge compared with the blade surface.

Finally, the influence of rain droplets on the turbine blade has been investigated. In this work, a DPM model is embedded in the aerodynamical simulations to analyze the effects of particle size, rain intensity on the blade performance. It is shown here that the rain droplet size is closely related to the rainfall intensity. Larger rainfall intensity means larger mean and median particle sizes. When the rain intensity increases, the number of smaller particles in a cubic meter of air also increases. Using the DPM for particle tracking, it shows that only a very small portion (about ~0.1%) of the particles inside the turbine domain will be trapped by the blade, however, no particles are observed to be reflected by the blade (i.e. bounce off the blade surface). With the median droplet size and different intensities, the comparisons show that the percentage of particles trapped by the blade increases when the rain intensity increases for the highest wind speed case. Although the rain intensity varies from $20mmh^{-1}$ to $100mmh^{-1}$, the corresponding particle sizes used does not change very much in this work. Therefore, the conclusion may be confined to this range. The trapping efficiency is a maximum of 0.18% for the 12 ms^{-1} case with a moderate rainfall rate of 40 mm/hr and a radius of

1.47 mm. This compares with the maximum possible rate of 0.2% from pure geometric consideration as the ratio of the blade leading edge area to the total domain size.

Future Work

This works acts as a necessary first step towards the formidable challenge of understanding the intricate connection between hydrometeors, blade aerodynamics, and blade leading edge erosion, therefore it is by no means conclusive. Many future endeavors are still needed to examine the processes involved. Therefore, some possible future works are discussed here.

First, a better rain texture model is required. The rain droplet is currently considered uniformly distributed in the simulation domain, which is not realistic. Therefore, a more observation-verified model is needed to consider some practical scenarios. The rain droplets currently are considered as spheres with the same radius. However, in natural rainfall, the rain droplets are of different sizes, hence, a better droplet function is also needed. Moreover, the rain droplets are assumed as solids in current work, which cannot change their forms or break into smaller droplets. Future work can make some improvements on this. Here we considered only rain, whereas other precipitation types particularly hail, may also be important.

Furthermore, some simplified 2D investigations may be heuristic. Since the current investigation is conducted in the 3D domain, which requires larger

computational resources, it is hence practical to conduct some simplified 2D simulations. The 2D simulations can provide a direct observation of the particle trajectories in a 2D plane and contribute to the theoretical modeling. The 2D simulations can also be used to calibrate the 3D simulations, which offers a possibility to verify the 3D results when no experimental data is available due to its current limitations.

Finally, the three wind conditions and the five rain intensity conditions may be enough for us to derive critical values in terms of wind speed and particle size. Similarly, rain intensity varies from $20mmh^{-1}$ to $100mmh^{-1}$ here, which may not be representative enough for all the rain scenarios across all wind farms. The range of particle sizes in this work is not very large, which indicates some future work can be extended to a wide particle range. In addition, the particles are assumed uniformly distributed in size and in the domain, which is not consistent with reality. Further work is required to introduce the Marshall-Palmer distribution in the simulations. In sum, more simulations with high resolution of boundary conditions are preferable. The simulations can be used to derive and verify theoretical models which will also be needed in the future to assess the potential for leading edge erosion at particular wind farm sites.

REFERENCES

1. ANSYS [15.6] User's Guide. https://www.ansys.com/en-in/
2. ANSYS [15.6] Theory Guide. https://www.ansys.com/en-in/
3. Amirzadeh, B., Louhghalam, A., Raessi, M., & Tootkaboni, M. (2017). A computational framework for the analysis of rain-induced erosion in wind turbine blades, part II: Drop impact-induced stresses and blade coating fatigue life. Journal of Wind Engineering and Industrial Aerodynamics. https://doi.org/10.1016/j.jweia.2016.12.007
4. Almohammadi, K. M., Ingham, D. B., Ma, L., & Pourkashanian, M. (2015). Modeling dynamic stall of a straight blade vertical axis wind turbine. Journal of Fluids and Structures. https://doi.org/10.1016/j.jfluidstructs.2015.06.003
5. Bako, A. N., Darboux, F., James, F., & Lucas, C. (2019). Rainfall erosivity in interrill areas: insights about the choice of an erosive factor. *CATENA*.
6. Barthelmie, R.J., Hansen, K.S. and Pryor, S.C. 2013: Meteorological controls on wind turbine wakes, Institute Electrical and Electronics Engineers, 101(4), 1010-1019.
7. Best, A. C. (1950). The size distribution of raindrops. Quarterly Journal of the Royal Meteorological Society. https://doi.org/10.1002/qj.49707632704
8. Bewley, G. P., Saw, E. W., & Bodenschatz, E. (2013). Observation of the sling effect. *New Journal of Physics*, *15*(8), 083051.
9. Bewley, G. P., Sreenivasan, K. R., & Lathrop, D. P. (2008). Particles for tracing turbulent liquid helium. *Experiments in Fluids*, *44*(6), 887-896.

10. Brendel, M., & Mueller, T. J. (1988). Boundary-layer measurements on an airfoil at low Reynolds numbers. *Journal of aircraft*, *25*(7), 612-617.
11. Cai, M., Abbasi, E., & Arastoopour, H. (2013). Analysis of the performance of a wind-turbine airfoil under heavy-rain conditions using a multiphase computational fluid dynamics approach. Industrial and Engineering Chemistry Research. https://doi.org/10.1021/ie300877t
12. Cao, H., "Aerodynamics Analysis of Small Horizontal Axis Wind Turbine Blades by Using 2D and 3D CFD Modelling. (2011)" MSc thesis: School of Computing, Engineering and Physical Sciences at the University of Central Lancashire, Preston, England
13. Casari, N., Pinelli, M., Suman, A., di Mare, L., & Montomoli, F. (2018). EBFOG: Deposition, Erosion, and Detachment on High-Pressure Turbine Vanes. *Journal of Turbomachinery*, *140*(6), 061001.
14. Dalili, N., Edrisy, A., & Carriveau, R. (2009). A review of surface engineering issues critical to wind turbine performance. Renewable and Sustainable Energy Reviews. https://doi.org/10.1016/j.rser.2007.11.009
15. Duque, E., Burkland, M., Johnson, W., (2003). Navier-stokes and comprehensive analysis performance predictions of the NREL phase VI experiment. J. Sol. Energ. Eng. 125(4), 43–61.
16. Ehrmann, R.S., et al., Realistic Leading-Edge Roughness Effects on Airfoil Performance, in 31st AIAA Applied Aerodynamics Conference. 2013, American Institute of Aeronautics and Astronautics.

17. Ehrmann, R.S. and E.B. White, *Influence of 2D Steps and Distributed Roughness on Transition on a NACA 63(3)-418*, in *32nd ASME Wind Energy Symposium*. 2014, American Institute of Aeronautics and Astronautics.
18. Ehrmann, R.S., et al., *Effect of Surface Roughness on Wind Turbine Performance*. 2017, Sandia National Laboratories: Albuquerque, NM. p. 114. SAND2017-10669.
19. European Wind Energy Association. (2011). Pure power-wind energy targets for 2020 and 2030. Ewea.
20. EWEA. (2011). Europe's Premier Wind Energy Even, MARCH, 2011, The European Wind Energy Council
21. Fuglsang P, Bak C. Development of the Risø wind turbine airfoils. Wind Energy: An International Journal for Progress and Applications in Wind Power Conversion Technology. 2004 Apr;7(2):145-62.
22. Fu, X., Li, H.-N., Yang, Y., (2015). Calculation of rain load based on single raindrop impinging experiment and applications. J. Wind Eng. Ind. Aerodyn. 147, 85–94.
23. Giguère P, Selig MS. Aerodynamic effects of leading-edge tape on aerofoils at low Reynolds numbers. Wind Energy: An International Journal for Progress and Applications in Wind Power Conversion Technology. 1999 Jul;2(3):125-36.
24. Goch, G., Knapp, W., & Härtig, F. (2012). Precision engineering for wind energy systems. CIRP annals, 61(2), 611-634.

25. Goward, G. W. "Protective coatings–purpose, role, and design." Materials Science and Technology 2.3 (1986): 194-200.
26. Gunn, R., & Kinzer, G. D. (2002). The terminal velocity of fall for water droplets in stagnant air. Journal of Meteorology. https://doi.org/10.1175/1520-0469(1949)006<0243:ttvoff>2.0.co;2
27. GWEC. (2019). Global Wind Energy Wind Report, April, 2019, Global Wind Energy Council
28. Hansen, M. O. (2015). *Aerodynamics of wind turbines*. Routledge.
29. Holton, J. R. (1973). An introduction to dynamic meteorology. American Journal of Physics, 41(5), 752-754.
30. Jasinski W, Noe S, Selig M, Bragg M, Jasinski W, Noe S, Selig M, Bragg M. Wind turbine performance under icing conditions. In35th Aerospace Sciences Meeting and Exhibit 1997 (p. 977).
31. Karmouch, R., & Ross, G. G. (2010). Superhydrophobic wind turbine blade surfaces obtained by a simple deposition of silica nanoparticles embedded in epoxy. Applied Surface Science. https://doi.org/10.1016/j.apsusc.2010.07.041
32. Keegan, M. H., Nash, D. H., & Stack, M. M. (2013a). Modelling Rain Drop Impact of Offshore Wind Turbine Blades. https://doi.org/10.1115/gt2012-69175
33. Keegan, M. H., Nash, D. H., & Stack, M. M. (2013). Numerical modelling of hailstone impact on the leading edge of a wind turbine blade. In EWEA Annual Wind Energy Event. https://doi.org/10.1007/978-88-470-0842-7

34. Keegan, M. H., Nash, D. H., & Stack, M. M. (2013b). On erosion issues associated with the leading edge of wind turbine blades. Journal of Physics D: Applied Physics. https://doi.org/10.1088/0022-3727/46/38/383001
35. Keegan, Mark. (2014). Wind Turbine Blade Leading Edge Erosion: A investigation of rain droplet and hailstone impact induced damage mechanisms. PhD Thesis, University of Strathclyde, Glasgow, Scotland
36. Kerho, M. F., & Bragg, M. B. (1997). Airfoil boundary-layer development and transition with large leading-edge roughness. *AIAA journal*, *35*(1), 75-84.
37. Khalfallah, M. G., & Koliub, A. M. (2007). Effect of dust on the performance of wind turbines. Desalination, 209(1-3), 209-220.
38. Langtry, R., Gola, J., & Menter, F. (2006, January). Predicting 2D airfoil and 3D wind turbine rotor performance using a transition model for general CFD codes. In *44th AIAA aerospace sciences meeting and exhibit* (p. 395).
39. Li, D., Zhao, Z., Li, Y., Wang, Q., Li, R., & Li, Y. (2018). Effects of the particle Stokes number on wind turbine airfoil erosion. *Applied Mathematics and Mechanics*, *39*(5), 639-652.
40. Li, Y., Paik, K.J., Xing, T., Carrica, P.M., (2012). Dynamic overset CFD simulations of wind turbine aerodynamics. Renew. Energy 37 (1), 285–298.
41. Mahadi Lawan Yakubu, Zulkifli Yusop. (2017a) Adaptability of rainfall simulators as a research tool on urban sealed surfaces – a review. Hydrological Sciences Journal 62:6, pages 996-1012.
42. Mahadi Lawan Yakubu, Zulkifli Yusop. (2017b) The influence of rain intensity on raindrop diameter and the kinetics of tropical rainfall: case study

of Skudai, Malaysia. Hydrological Sciences Journal. https://doi.org/10.1080/02626667.2014.934251

43. Manwell, J. F., McGowan, J. G., & Rogers, A. L. (2010). Wind energy explained: theory, design and application. John Wiley & Sons.
44. Marshall, J. S., & Palmer, W. M. K. (2002). THE DISTRIBUTION OF RAINDROPS WITH SIZE. Journal of Meteorology. https://doi.org/10.1175/1520-0469(1948)005<0165:tdorws>2.0.co;2
45. Matteoni, G., & Georgakis, C. T. (2012). Effects of bridge cable surface roughness and cross-sectional distortion on aerodynamic force coefficients. Journal of Wind Engineering and Industrial Aerodynamics. https://doi.org/10.1016/j.jweia.2012.02.029
46. Matteoni, G., & Georgakis, C. T. (2015). Effects of surface roughness and cross-sectional distortion on the wind-induced response of bridge cables in dry conditions. Journal of Wind Engineering and Industrial Aerodynamics. https://doi.org/10.1016/j.jweia.2014.11.003
47. Mezhericher, M., Brosh, T., & Levy, A. (2011). Modeling of particle pneumatic conveying using DEM and DPM methods. Particulate Science and Technology, 29(2), 197-208.
48. Montero-Martínez, G., Kostinski, A. B., Shaw, R. A., & García-García, F. (2009). Do all raindrops fall at terminal speed? Geophysical Research Letters. https://doi.org/10.1029/2008GL037111
49. Morata, F., & Sandoval, I. S. (Eds.). (2012). European energy policy: An environmental approach. Edward Elgar Publishing.

50. Moreau, D. J., Doolan, C. J., Alexander, W. N., Meyers, T. W., & Devenport, W. J. (2016). An Experimental Investigation of Wall-Mounted Finite Airfoil Turbulent Boundary Layer Noise. In *Fluid-Structure-Sound Interactions and Control* (pp. 45-49). Springer, Berlin, Heidelberg.
51. Pryor, S. C., & Barthelmie, R. J. (2010). Climate change impacts on wind energy: A review. *Renewable and sustainable energy reviews*, *14*(1), 430-437.
52. Pryor, S. C., Spaulding, A. M., & Barthelmie, R. J. (2010). New particle formation in the Midwestern USA: Event characteristics, meteorological context and vertical profiles. *Atmospheric Environment*, *44*(35), 4413-4425.
53. Rumsey, M.A. *Leading-Edge Erosion Measurements* in *Blade Reliability Collaborative Meeting 2013*. 2013. Albuquerque, NM.
54. Safaei, M. R., Mahian, O., Garoosi, F., Hooman, K., Karimipour, A., Kazi, S. N., & Gharehkhani, S. (2014). Investigation of micro-and nanosized particle erosion in a 90 pipe bend using a two-phase discrete phase model. *The scientific world journal*, *2014*.
55. Samson, A., & Sarkar, S. (2016). Effects of free-stream turbulence on transition of a separated boundary layer over the leading-edge of a constant thickness airfoil. *Journal of Fluids Engineering*, *138*(2), 021202.
56. Sareen, A., Sapre, C. A., & Selig, M. S. (2014). Effects of leading edge erosion on wind turbine blade performance. Wind Energy. https://doi.org/10.1002/we.1649

57. Saw, E. W., Bewley, G. P., Bodenschatz, E., Sankar Ray, S., & Bec, J. (2014). Extreme fluctuations of the relative velocities between droplets in turbulent airflow. *Physics of Fluids*, *26*(11), 111702.

58. Sayer, F., Bürkner, F., Buchholz, B., Strobel, M., Van Wingerde, A. M., Busmann, H. G., & Seifert, H. (2013). Influence of a wind turbine service life on the mechanical properties of the material and the blade. Wind Energy. https://doi.org/10.1002/we.53

59. Schuerich, F., & Brown, R. E. (2012). Effect of Dynamic Stall on the Aerodynamics of Vertical-Axis Wind Turbines. AIAA Journal. https://doi.org/10.2514/1.j051060

60. Sezeruzol, N., Long, L., (2006). 3-D time-accurate CFD simulations of wind turbine rotor flow fields. Parallel Comput. Fluid Dyn. 394, 457–464.

61. Shu, L., Li, H., Hu, Q., Jiang, X., Qiu, G., He, G., & Liu, Y. (2018). 3D numerical simulation of aerodynamic performance of iced contaminated wind turbine rotors. *Cold Regions Science and Technology*, *148*, 50-62.

62. Slot, H. M., Gelinck, E. R. M., Rentrop, C., & Van Der Heide, E. (2015). Leading edge erosion of coated wind turbine blades: Review of coating life models. Renewable Energy, 80, 837-848.

63. Simcafe, 2019: https://confluence.cornell.edu/display/SIMULATION

64. Somers, D. M. (2004). S814 and S815 Airfoils: October 1991--July 1992 (No. NREL/SR-500-36292). National Renewable Energy Lab., Golden, CO (US).

65. Sørensen, N.N., Michelsen, J.A., Schreck, S., (2013). Navier-stokes predictions of the NREL phase VI rotor in the NASA Ames 80 ft×120 ft wind tunnel. Wind Energ. 5 (2–3), 151–169.
66. Stull, Roland. Meteorology for scientists and engineers. Brooks/Cole, 2000.
67. Stinebring, D. R., Holl, J. W., & Arndt, R. E. (1980). Two aspects of cavitation damage in the incubation zone: scaling by energy considerations and leading edge damage. Journal of Fluids Engineering, 102(4), 481-485.
68. Torres, D. S., Porrà, J. M., and Creutin, J.-D. (1994). A general formulation for raindrop size distribution. Journal of Applied Meteorology, 33(12):1494–1502
69. Uematsu, Y., & Yamada, M. (1995). Effects of aspect ratio and surface roughness on the time-averaged aerodynamic forces on cantilevered circular cylinders at high Reynolds numbers. Journal of Wind Engineering and Industrial Aerodynamics. https://doi.org/10.1016/0167-6105(94)00049-J
70. Van Rooij RP, Timmer WA. Roughness sensitivity considerations for thick rotor blade airfoils. InASME 2003 Wind Energy Symposium 2003 Jan 1 (pp. 22-31). American Society of Mechanical Engineers.
71. Varikoden, H., Samah, A. A., & Babu, C. A. (2010). Spatial and temporal characteristics of rain intensity in the peninsular Malaysia using TRMM rain rate. *Journal of hydrology*, *387*(3-4), 312-319.
72. Wagner, H. J. (2013). Introduction to wind energy systems. In EPJ Web of Conferences (Vol. 54, p. 01011). EDP Sciences.
73. Wilcox, B. and E. White, *Computational analysis of insect impingement patterns on wind turbine blades.* Wind Energy, 2016. **19**(3): p. 483-495.

74. WISER. (2016). 2016 Wind Energy Technologies Market Reports, Office of Energy Efficiency & Renewable Energy, http:/www.osti.gov/scitech

75. Wu, Z., Lv, B., & Cao, Y. (2019). Improved Taylor analogy breakup and Clark models for droplet deformation prediction. Proceedings of the Institution of Mechanical Engineers, Part G: Journal of Aerospace Engineering. https://doi.org/10.1177/0954410017736545

76. Yakubu, M. L., Yusop, Z., & Fulazzaky, M. A. (2016). The influence of rain intensity on raindrop diameter and the kinetics of tropical rainfall: case study of Skudai, Malaysia. Hydrological Sciences Journal. https://doi.org/10.1080/02626667.2014.934251